

School of Mathematical Sciences  
Centre in Statistical Science and Industrial Mathematics  
Queensland University of Technology

# **Numerical Modelling of Industrial Microwave Heating**

VIKTOR VEGH

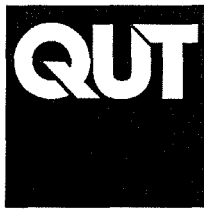
A thesis submitted for the degree of Doctor of Philosophy in the Faculty of  
Science, Queensland University of Technology according to QUT requirements  
for presenting theses by published and submitted manuscripts.

2003

Principal Supervisor: Dr. Ian W. Turner

Associate Supervisor: Dr. Huawei (Bob) Zhao

Associate Supervisor: Dr. Troy Farrell



QUEENSLAND UNIVERSITY OF TECHNOLOGY

DOCTOR OF PHILOSOPHY THESIS EXAMINATION

CANDIDATE NAME: *Viktor Vegh*

CENTRE: *Statistical Science and Industrial Mathematics*

PRINCIPAL SUPERVISOR: *Dr Ian Turner*

ASSOCIATE SUPERVISOR(S): *Dr Troy Farrell  
Dr Huawei Zhao*

THESIS TITLE: *Numerical Modelling of Industrial Microwave Heating*

*Under the requirements of PhD regulation 16.8, the above candidate presented a Final Seminar that was open to the public. A Faculty Panel of three academics attended and reported on the readiness of the thesis for external examination. The members of the panel recommended that the thesis be forwarded to the appointed Committee for examination.*

Name: DR. IAN W. TURNER  
*Panel Chairperson (Principal Supervisor)*

Name: DR. TROY W. FARRELL  
*Panel Member*

Name: DR. HUAWEI ZHAO  
*Panel Member*

Name: .....  
*Panel Member*

*Under the requirements of PhD regulations, Section 16, it is hereby certified that the thesis of the above-named candidate has been examined. I recommend on behalf of the Examination Committee that the thesis be accepted in fulfilment of the conditions for the award of the degree of Doctor of Philosophy.*

Name: A N PETTITT Signature: Date: 2/5/03  
*Chair of Examiners (Head of School or nominee) (Examination Committee)*

*To Joanne*



# Abstract

The numerical modelling of electromagnetic waves has been the focus of many research areas in the past. Some specific applications of electromagnetic wave scattering are in the fields of Microwave Heating and Radar Communication Systems. The equations that govern the fundamental behaviour of electromagnetic wave propagation in waveguides and cavities are the Maxwell's equations. In the literature, a number of methods have been employed to solve these equations. Of these methods, the classical Finite-Difference Time-Domain scheme, which uses a staggered time and space discretisation, is the most well known and widely used. However, it is complicated to implement this method on an irregular computational domain using an unstructured mesh.

In this work, a coupled method is introduced for the solution of Maxwell's equations. It is proposed that the free-space component of the solution is computed in the time domain, whilst the load is resolved using the frequency dependent electric field Helmholtz equation. This methodology results in a time-frequency domain hybrid scheme. For the Helmholtz equation, boundary conditions are generated from the time dependent free-space solutions. The boundary information is mapped into the frequency domain using the Discrete Fourier Transform. The solution for the electric field components is obtained by solving a sparse-complex system of linear equations. The hybrid method has been tested for both waveguide and cavity configurations. Numerical tests performed on waveguides and cavities for inhomogeneous lossy materials highlight the accuracy and computational efficiency of the newly proposed hybrid computational electromagnetic strategy.

*Keywords:* *Finite-Difference Time-Domain, Maxwell's Equation, Frequency Domain, Helmholtz Equation, Discrete Fourier Transform, Hybrid Method*



# List of Publications & Manuscripts

Liu, B., Marchant, T.R., Turner, I.W., **Vegh, V.** A Comparison of Three-dimensional Semi-analytical and Numerical Techniques for the Microwave Heating of a Lossy Material in a Waveguide, 3rd World Congress on Microwave and Radio Frequency Applications, September 2002.

**Vegh, V.**, Turner, I.W. Comparison of Time-Domain Numerical Solvers for the Propagation of a Gaussian Pulse Inside a Rectangular Waveguide, Australian & New Zealand Industrial and Applied Mathematics Journal - Electronic Supplement, **44**, 2002–3.

**Vegh, V.**, Turner, I.W., Zhao, H. Comparison of Time-Domain Solvers for the Solution of Maxwell's Equations, submitted in the International Journal of Applied Mathematical Modelling, 2001 submitted for publication.

**Vegh, V.**, Turner, I.W. A Hybrid Approach for Resolving the Microwave Heating inside Lossy Media, Advances in Microwave and Radio Frequency Processing, Ampere 8, Germany, 2002.

**Vegh, V.**, Turner, I.W. A Hybrid Technique for Computing the Power Distribution Generated in a Lossy Medium During Microwave Heating, submitted for publication in International Journal of Computational and Applied Mathematics, 2003.



# Contents

<b>Abstract</b>	iii
<b>List of Publications &amp; Manuscripts</b>	v
<b>List of Figures</b>	xii
<b>List of Tables</b>	xiii
<b>Statement of Original Authorship</b>	xv
<b>Acknowledgments</b>	xvii
<b>1 Introduction and Literature Review</b>	1
1.1 Introduction . . . . .	2
1.1.1 Aims of the Research Work . . . . .	6
1.1.2 The Microwave Heating Process . . . . .	7
1.1.3 The Microwave Heating Apparatus . . . . .	8
1.1.4 Classification of Waveguide and Cavity . . . . .	9
1.1.5 Calibration of the Applicator . . . . .	15
1.1.6 Material Properties . . . . .	15
1.1.7 Computing the Dissipated Heat . . . . .	16
1.1.8 Thermal Runaway . . . . .	17
1.1.9 Generalisations in the Numerical Methods . . . . .	18
1.2 Existing Numerical Models in Microwave Heating . . . . .	19

1.2.1	Form of the Governing Equations . . . . .	21
1.2.2	Spatial Discretisation Strategies . . . . .	23
1.2.3	Resolution of the Time Derivative . . . . .	35
1.2.4	Corrections, Smoothing and Special Boundary Conditions	39
1.3	The Hybrid Model . . . . .	41
1.3.1	Exterior Problem . . . . .	42
1.3.2	Boundary Problem . . . . .	43
1.3.3	Interior Problem . . . . .	44
1.4	Outline of Thesis . . . . .	45
1.4.1	Chapter 2 . . . . .	45
1.4.2	Chapter 3 . . . . .	46
1.4.3	Chapter 4 . . . . .	47
1.4.4	Chapter 5 . . . . .	48
1.4.5	Chapter 6 . . . . .	49
1.4.6	Chapter 7 . . . . .	50
	Bibliography . . . . .	51
<b>2</b>	<b>Microwave Heating of a Lossy Material in a Three-dimensional Waveguide</b>	<b>59</b>
2.1	Introduction . . . . .	62
2.2	Governing equations . . . . .	65
2.2.1	The frequency domain . . . . .	67
2.3	The numerical schemes . . . . .	69
2.3.1	The Frequency Domain Solution Method . . . . .	69
2.3.2	The Time Domain Solution Method . . . . .	70
2.4	Results and comparisons . . . . .	72
2.5	Conclusions . . . . .	75
	Bibliography . . . . .	77

<b>3 Propagation of a Gaussian Pulse</b>	<b>79</b>
3.1 Introduction . . . . .	81
3.2 Cell-Centred Finite-Volume Time-Domain Methods . . . . .	84
3.3 Boundary Conditions . . . . .	89
3.4 Results . . . . .	92
3.5 Conclusion . . . . .	96
Bibliography . . . . .	99
<b>4 Time-Domain Solvers for the Solution of Maxwell's Equations</b>	<b>101</b>
4.1 Introduction . . . . .	103
4.2 Mathematical Formulations . . . . .	108
4.3 Implementation of Boundary Conditions . . . . .	115
4.4 Results and Discussion . . . . .	124
4.5 Conclusion . . . . .	140
Bibliography . . . . .	143
<b>5 The Hybrid Method in a Single-Mode Waveguide</b>	<b>147</b>
5.1 Introduction . . . . .	149
5.2 Numerical Solution of the Maxwell's Equations - Exterior Problem	151
5.3 Numerical Solution of the Helmholtz Equation - Interior Problem	153
5.4 Summary of the Hybrid Method . . . . .	154
5.5 Results . . . . .	155
5.6 Conclusions . . . . .	157
Bibliography . . . . .	159
<b>6 The Hybrid Method in a Multi-Mode Apparatus</b>	<b>161</b>
6.1 Introduction . . . . .	163
6.2 Outline of the Hybrid Method . . . . .	167
6.2.1 Exterior Problem - Maxwell's Equations . . . . .	169
6.2.2 Interior Problem - Helmholtz Equation . . . . .	171

6.3	Boundary Conditions . . . . .	176
6.4	Results . . . . .	179
6.4.1	Case Study 1 - Fully Loaded Waveguide . . . . .	181
6.4.2	Case Study 2 - Semi Loaded Waveguide . . . . .	185
6.4.3	Case Study 3 - Mashed Potato . . . . .	188
6.4.4	Case Study 4 - Layers of Pastry . . . . .	192
6.5	Conclusions . . . . .	194
	Bibliography . . . . .	197
<b>7</b>	<b>General Discussion</b>	<b>201</b>
7.1	Conclusions and Remarks . . . . .	201
7.2	Recommendations for Future Work . . . . .	205

# List of Figures

1.1	The conventional microwave oven . . . . .	9
1.2	An industrial microwave heating apparatus . . . . .	10
1.3	Waveguides . . . . .	11
1.4	Rectangular waveguide dimensions . . . . .	12
1.5	Dimensions of a cavity . . . . .	13
1.6	Spatial discretisation . . . . .	26
1.7	Time discretisation . . . . .	36
1.8	The Hybrid method . . . . .	43
2.1	Time-domain algorithm flowchart . . . . .	72
2.2	Steady-state power versus temperature curve . . . . .	74
3.1	A Yee cell . . . . .	82
3.2	A cell within the computational domain . . . . .	85
3.3	Incident and absorbing boundary conditions . . . . .	90
3.4	A selection of numerical simulations of a Gaussian pulse . . . . .	94
3.5	RK4 simulation of Gaussian pulse inside a waveguide . . . . .	95
4.1	A 3D cell inside the computational domain . . . . .	112
4.2	Perfectly conducting wall boundary conditions . . . . .	115
4.3	Incident and absorbing boundary condition treatment . . . . .	117
4.4	Input plane boundary condition implementation . . . . .	122
4.5	Free-space and material boundary condition treatment . . . . .	123

4.6	Various simulations of an empty waveguide . . . . .	129
4.7	RK3 and RK4 simulations of an empty waveguide . . . . .	130
4.8	Various simulations of a loaded waveguide with $\varepsilon_r = 1 - 0.2j$ . . .	132
4.9	RK4 simulations of a loaded waveguide with $\varepsilon_r = 1 - 0.2j$ . . .	134
4.10	Various simulations of a loaded waveguide with $\varepsilon_r = 2 - 0.5j$ . . .	135
4.11	RK4 simulations of a loaded waveguide with $\varepsilon_r = 2 - 0.5j$ . . .	136
4.12	The waveguide set up for the multi-mode study . . . . .	137
4.13	Normalised 2D contour plots of various simulations . . . . .	139
5.1	The Hybrid method with material properties $\varepsilon_r = 2 - 0.5j$ . . . .	157
5.2	The Hybrid method with material properties $\varepsilon_r = 3 - j$ . . . .	158
6.1	Schematic of a loaded waveguide . . . . .	168
6.2	The interior problem . . . . .	170
6.3	Finite-volume representation of a cell face . . . . .	172
6.4	Case study 1 - loaded waveguide with coarse mesh . . . . .	181
6.5	Case study 1 - loaded waveguide with fine mesh . . . . .	182
6.6	Case study 1 - contour plots of FD-TD versus Hybrid method . .	183
6.7	Case study 1 - line plots of FD-TD versus Hybrid method . .	183
6.8	Case study 2 - loaded waveguide with coarse mesh . . . . .	185
6.9	Case study 2 - loaded waveguide with fine mesh . . . . .	186
6.10	Case study 2 - contour plots of FD-TD versus Hybrid method . .	187
6.11	Case study 2 - line plots of FD-TD versus Hybrid method . .	188
6.12	The outline of the cavity problem. . . . .	189
6.13	Case study 3 - mashed potato . . . . .	190
6.14	Case study 4 - pastry block . . . . .	193

# List of Tables

1.1	Nomenclature for Chapter 1 . . . . .	2
1.2	Maxwell's equations . . . . .	22
1.3	Time harmonic electromagnetic equations . . . . .	23
2.1	Nomenclature for Chapter 2 . . . . .	61
3.1	Nomenclature for Chapter 3 . . . . .	80
4.1	Nomenclature for Chapter 4 . . . . .	102
4.2	Numerical scheme definitions . . . . .	126
4.3	Amplitude and phase errors of different numerical schemes . . . . .	128
5.1	Nomenclature for Chapter 5 . . . . .	148
6.1	Nomenclature for Chapter 6 . . . . .	162



## **Statement of Original Authorship**

The work contained in this thesis has not been previously submitted for a degree or diploma at any other higher education institution. To the best of my knowledge and belief, the thesis contains no material previously published or written by any other person except where due reference is made.

Signed: \_\_\_\_\_

Date: 13/5/03



# Acknowledgments

**Ian W. Turner.** I would like to thank Ian for his endless support through the duration of my thesis. For the three and a half years he was there for me, helped and guided the work. Without him this work could never have been completed. I look forward to working with him for many years to come. I believe that Ian has a lot to give to the computational modelling community. Thank you Ian, you are a great friend.

**Huawei (Bob) Zhao.** I clearly remember the times when we went fishing on weekends and talked about time-marching schemes for resolving the time-dependent electromagnetic fields. Bob's work with the FD-TD method helped me understand the constraints of numerical methods for the Maxwell's equations. Without his input into some of the papers, this thesis would not have been the same standard. Bob, I greatly appreciate the time and effort that you have put aside for me.

**Troy Farrell.** I would like to thank Troy for putting time aside for me when I needed it most. He has been very helpful and I look forward to working with him in the future. Thank you Troy.

**Timothy R. Marchant.** Thermal runaway in industrial microwave processes is a phenomenon that is observed frequently in ceramics. Tim contributed to this thesis by helping me understand better ways of modelling industrial applications that can have thermal runaway in the heating process. I find Tim to be very knowledgeable and it has been a pleasure working with him. Many thanks Tim.

**Bin Liu.** Many late nights and endless weekends were spent by Bin and myself comparing different types of semi-analytical and numerical algorithms. At times it seemed like the solution was not near, but Bin and I stuck through it. Thank you Bin for being patient, after all in the end we did it.

**Joseph A. Young.** Over the years and throughout the duration of my thesis work I attended numerous conferences and gave a number presentations to different groups of people. Joe helped me with some of the visualisations, which were great. Thank you Joe for those late nights when you stayed up to help me get the 3D volume visualisations of the waveguide working.

**Queensland University of Technology.** I would like to thank the university for the opportunity to complete my PhD and to have the financial support of a QUT scholarship.



# **Chapter 1**

## **Introduction and Literature Review**

NOMENCLATURE	
<b>A</b>	Coefficient matrix
<b>b</b>	Right hand vector
<b>B</b>	Magnetic flux density ( $T$ )
<b>D</b>	Diagonal matrix
<b>H</b>	Magnetic field intensity ( $A/m$ )
<b>M<sub>l</sub></b>	Left preconditioning matrix
<b>n</b>	Unit outward normal to face $f$
$a_g$	Broad dimension of waveguide ( $m$ )
$b_g$	Narrow dimension of waveguide( $m$ )
$c_c$	Height of cavity ( $m$ )
$f$	A face of a Cartesian cell
$f_g$	Cutoff frequency of waveguide ( $Hz$ )
$j$	Complex unity
$m$	Modes in the $x$ -coordinate direction
$n$	Modes in the $y$ -coordinate direction
$p$	Modes in the $z$ -coordinate direction
$s$	Surface area ( $m^2$ )
$V$	Voltage ( $V$ )
$\delta_x$	Cell dimension in the $x$ direction
$\delta_z$	Cell dimension in the $z$ direction
$\delta_t$	Time step of numerical scheme ( $s$ )
$\epsilon$	Permittivity ( $F/m$ )
$\epsilon'$	Relative dielectric constant
$\lambda$	Unbounded wavelength ( $m$ )
$\lambda_g$	Cutoff wavelength of waveguide ( $m$ )
$\mu$	Permeability ( $H/m$ )
$\sigma$	Electric conductivity ( $\Omega^{-1}/m$ )
$\hat{\mathbf{A}}$	Augmented matrix
$\hat{\mathbf{b}}$	Augmented right hand vector
<b>D</b>	Electric flux density ( $V/m$ )
<b>E</b>	Electric field intensity( $V$ )
<b>J</b>	Electric current density ( $A/m^2$ )
<b>M<sub>r</sub></b>	Right preconditioning matrix
$a_c$	Broad dimension of cavity ( $m$ )
$b_c$	Narrow dimension of cavity ( $m$ )
$c$	Wave speed ( $m/s$ )
$c_g$	Length of waveguide ( $m$ )
$f$	Frequency ( $Hz$ )
$i$	Current ( $A$ )
$k_2$	Condition number
$n$	Matrix dimension
$n$	The $n^{th}$ time level
$q$	Charge ( $C$ )
$v$	Volume ( $m^3$ )
$\beta_0$	Phase factor of free-space
$\delta_y$	Cell dimension in the $y$ direction
$\delta_s$	Surface area of face $f$ ( $m^2$ )
$\delta_v$	Volume of the cell ( $m^3$ )
$\epsilon_r$	Relative permittivity
$\epsilon''$	Relative loss factor
$\lambda_c$	Cutoff wavelength in cavity ( $m$ )
$\lambda_w$	Wavelength in waveguide ( $m$ )
$\omega$	Angular frequency ( $2\pi f$ ) ( $rad/s$ )

Table 1.1: List of symbols used in Chapter 1.

## 1.1 Introduction

Computational Electromagnetics (CEM) is an important research field that spans the disciplines of Engineering, Science and Environmental Studies. The impact of CEM is clearly evident in the literature, where it has been employed in the study of many key industrial problems, including microwave heating and drying processes, and also sterilisation. The first evidence of CEM appeared in the

1940s where it was used to investigate satellite communication systems [1]. Later the numerical techniques developed for high frequency free-space propagation of electromagnetic waves in satellite communications were adapted to other fields, including industrial microwave heating.

During the growth period of CEM, a number of different numerical techniques have been developed to resolve the governing electromagnetic equations, which in the time-domain are referred to as Maxwell's equations. The biggest achievement was the development of the Finite-Difference Time-Domain (FD-TD) method by Yee in the middle of the 1960s [2]. In fact, to this day, many researchers use the FD-TD method as a benchmark algorithm to compare any newly developed electromagnetic numerical modelling techniques.

In the last twenty years, the FD-TD method has been widely analysed and implemented, applied to many different problems and used to study the interaction of electromagnetic fields with a variety of media. The current state-of-the-art FD-TD solution strategy has evolved during this period from a simple two-dimensional computational model to a very powerful three-dimensional simulation tool for investigating electromagnetic field phenomena in many complex industrial microwave and radio-frequency cavity designs. During the last three decades, the following important milestones in industrial microwave heating and CEM should be noted:

- *Bosisio and Nachman, 1975*: Introduced a simplistic approach for determining the electric field distribution inside a microwave applicator [3].
- *Mur, 1981*: Developed a new approach to absorb fields for the finite-difference approximation of the time-domain electromagnetic field equations [4].

- *Metaxas and Meredith, 1983*: Published a book dedicated to the field of industrial microwave heating [1].
- *De Pourceq and Eng, 1985*: Three-dimensional power-density calculations were performed using finite-difference approximations [5].
- *Madsen and Ziolkowski, 1988*: Investigated irregular non-orthogonal grids for the solution of the time-domain Maxwell's equations [6].
- *Shankar and Mohammadian, 1990*: Applied techniques from computational fluid dynamics in computational electromagnetics to resolve the time-domain electromagnetic equations in a new form [7].
- *Jia and Jolly, 1992*: Introduced a three-dimensional finite-element method for the simulation of microwave field and power distributions [8].
- *Berenger, 1993*: A new absorbing boundary concept was derived that is called the Perfectly Matched Layer (PML) for the finite-difference time-domain discretisation of Maxwell's equations [9, 10].
- *Fu and Metaxas, 1994*: Power density calculations were performed in a multi-mode cavity using full three-dimensional electromagnetic simulations [11].
- *Dibben, 1995*: Finite element methods were investigated and experimental modelling of microwave applicators was conducted [12].
- *Zhao, 1997*: A comprehensive study of heating of lossy dielectric materials inside arbitrary shaped cavities using various time-domain numerical strategies to resolve the electromagnetic equations was performed [13].
- *Reader and Chow Ting Chan, 1998*: Experimental and numerical field studies in loaded multimode and single mode cavities was thoroughly investigated [14].

- *Ditkowski, 2001*: Staircasing problems at boundaries have been investigated and eliminated, and a special free-space and material interface condition for the propagation of electromagnetic waves was introduced [15].
- *Xie, 2002*: An explicit fourth-order finite-difference time-domain numerical solver for the Maxwell's equations was proposed [16].

Although existing CEM models can be used to investigate a variety of important industrial problems in microwave heating and drying, substantial computational overheads are associated with these schemes to obtain suitable results to allow for strategic decision making. For example, in the optimisation of a combined microwave and convective drying process, the drying engineer would need knowledge of the moisture, thermal and internal pressure fields together with the power distribution in the load. This complex coupled system would require numerous simulations to be performed before the optimal design is reached. Therefore, the computation time for the simulations is crucial, hence requiring that the underlying CEM algorithm needs to be as efficient as possible. Current CEM trends indicate that the prediction of the power distribution for an irregularly shaped load placed within a small-scale industrial microwave cavity can take from hours to days to obtain a single estimate of the electromagnetic field evolution. This bottleneck provides the motivation of this thesis for deriving a new and innovative strategy for determining the power distribution in the load, which then can be coupled with either the heat equation or the more complicated heat and mass transfer models.

In the past, researchers have investigated two different approaches to resolving the electromagnetic phenomena within a microwave heating process. Firstly, time-domain methods have been investigated, where the numerical solution strategy uses a time-marching algorithm to predict the nature of the electric and magnetic fields at the next time step. Secondly, time-harmonic or frequency-domain

implicit solvers have been applied to microwave heating problems. The latter techniques predict the electric and magnetic fields at a particular frequency. Generally, a number of solutions to the problem are obtained at frequencies within the vicinity of the dominant frequency. Time-domain and frequency-domain equations and solvers are discussed further in §1.2.1.

This thesis makes its contribution to both of the areas of industrial microwave heating and CEM. An innovative numerical strategy for analysing microwave heating problems, which combines the power of a time-domain solver with an efficient frequency-domain solver, can be used to predict the power distribution generated in a lossy medium during microwave heating. This *hybrid* approach resolves the power distribution more efficiently than existing methods and maintains the accuracy of the solution. This efficient computational tool can be used by engineers to investigate, design and analyse new and exciting cavity structures that seek to optimise the power delivered to the material.

### 1.1.1 Aims of the Research Work

The work in this thesis is specifically focused towards the study of the microwave heating process. Primarily, the aim of the work is to identify a new and innovative methodology for resolving the governing electromagnetic equations. The main objectives of the thesis are to:

- (a) *Develop efficient and accurate computational algorithms for simulating industrial microwave heating processes.*
- (b) *Investigate and provide further insight into the physical phenomenon of thermal runaway and the way in which electromagnetic waves interact with dielectric materials in waveguide and cavity structures.*
- (c) *Calibrate the computational model for industrial use by applying it to specific*

*case studies in dielectric heating using high frequency microwave energy.*

### **1.1.2 The Microwave Heating Process**

Microwaves have been used in industry since the early 1940s [17, 18], and today the benefits of this technological advance have been widely adopted to the heating of food and the drying of building materials like wood and bricks. Microwave energy has also been used in the treatment of waste, both chemical and domestic, and in sterilisation, for example tree roots.

In the modern family home the domestic microwave oven is as important as the television set that provides hours of entertainment. As a consequence, research in the field of microwave heating, and in particular the search for the optimal microwave design that delivers heating uniformly in the load is invaluable [19]. The millions of microwave ovens in use today for both industrial and domestic purposes are based on the same fundamental concept and design. Therefore, the study of industrial microwave heating can be adapted easily to more conventional microwave ovens found in many household kitchens.

There are many benefits to using microwave energy as a source for heating [1]. One of the key benefits is the speed of processing compared to conventional systems, which arises due to the volumetric delivery of energy associated with the microwave processing phenomenon. Other benefits include rapid heating, efficient use of energy, high end product quality and usually a clean and compact heating environment.

Conventional heating methods rely on the delivery of energy through the conduction of heat from the surface of the product. Depending on material properties, this conductive heating process may take a long time and may not produce

an acceptable final product quality. Because microwave technology delivers the bulk of the energy in a highly concentrated and very rapid manner to the product, the case-hardening of products that are heated and dried by classical convective methods often can be eliminated. This advantage is a major attraction for the industrial microwave heating process.

### **1.1.3 The Microwave Heating Apparatus**

The basic conceptual idea behind a domestic microwave heating process is illustrated in Figure 1.1. Industrial processes are based around the same principal as illustrated in Figure 1.2, whereby the electromagnetic energy is delivered using a waveguide. In the figures, the load or product is located at the bottom of the cavity, which is referred to as the applicator when the waveguide is included. The dimension of the applicator is calculated so that certain electromagnetic fields are generated within the cavity when the product is not present. These fields are delivered via a waveguide. Waveguides are usually attached to a power source, and in this form, the energy delivery device is referred to as a magnetron. The magnetron has certain specifications and dimensions that in these cases (see Figures 1.1 and 1.2) delivers the electromagnetic energy through a rectangular cross section.

The magnetron has a nominal output power, which is transferred into the cavity via the waveguide in the form of electromagnetic waves. This input power is usually excited over the cross-section of the waveguide, and hence, measured in  $W/m^2$ . The absorbed power is then computed according to the governing equations in  $W/m^3$  within the load, which is dependent on the dielectric properties of the material (see §1.1.6 for discussion on dielectric properties). Generally, all computations are done with an initial unity wave amplitude and the absorbed energy distribution in the product determined. More often than not in modern

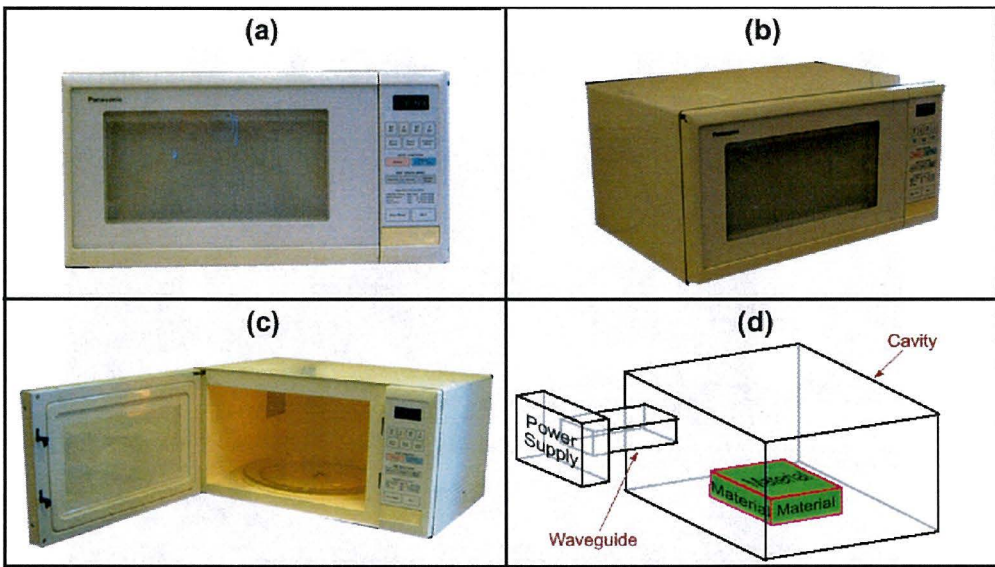


Figure 1.1: The conventional microwave oven. The different components of the microwave heating system are exhibited; (a) front view, (b) perspective view, (c) open cavity and (d) main components.

calculations, the absorbed power inside the load is determined directly without the use and implementation of an energy balance equation. In this case, the electric and magnetic field amplitudes are calculated using the average input power of the waveguide, whilst in the case of unity input field amplitude, an energy balance for the system is calculated from which the absorbed power is computed. In this thesis, the relationship between the average input power and the incident field amplitude is used in the numerical electromagnetic field simulations.

#### 1.1.4 Classification of Waveguide and Cavity

In many industrial applications, a  $TE_{mn}$  waveguide is used to deliver the energy to the material. In Figure 1.3 a selection of waveguides is exhibited. The Transverse Electric (TE) fields travel through the waveguide into the applicator. Transverse Magnetic (TM) waveguides are also used for industrial applications. The numerical implementation of the TM field components is similar to the TE

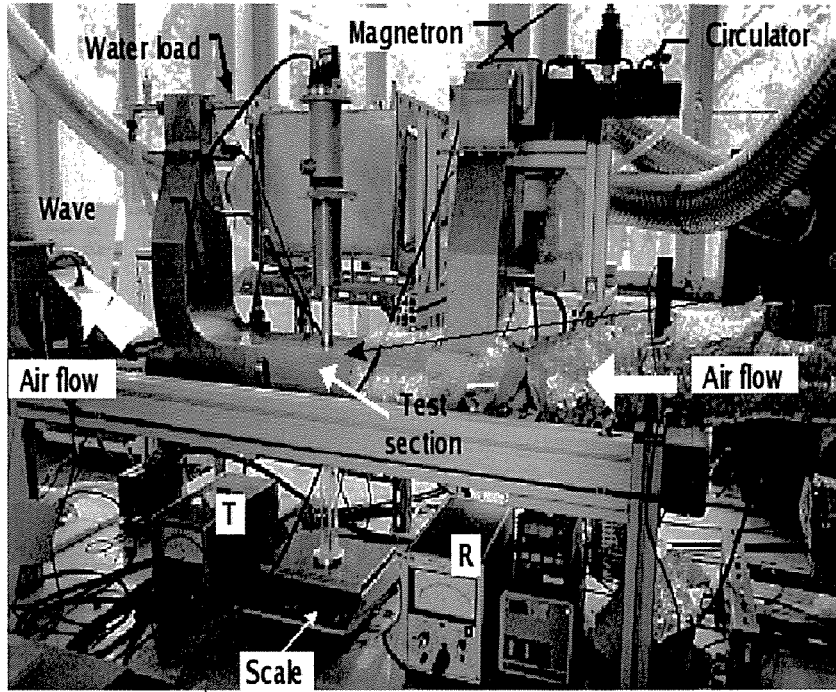


Figure 1.2: An industrial microwave heating apparatus, where the different components of the microwave heating system are exhibited. Picture adapted from [20].

case, the differences arise due to the cross-sectional dimension of the waveguide and the form of the particular components of the incident fields [17].

The  $m$  and  $n$  subscripts ( $TE_{mn}$ ) refer to the modes that are generated inside the waveguide, where the modes are determined by the cross-sectional dimensions of the waveguide. The  $m$  subscript refers to the broad side of the waveguide and the  $n$  subscript refers to the narrow side of the waveguide (see Figure 1.4). For example, if the broad side of a rectangular waveguide has dimension  $a_g$  and the narrow side has dimension  $b_g$ , then the cutoff wavelength ( $\lambda_g$ ) of the guide is determined by the following expression [17]:

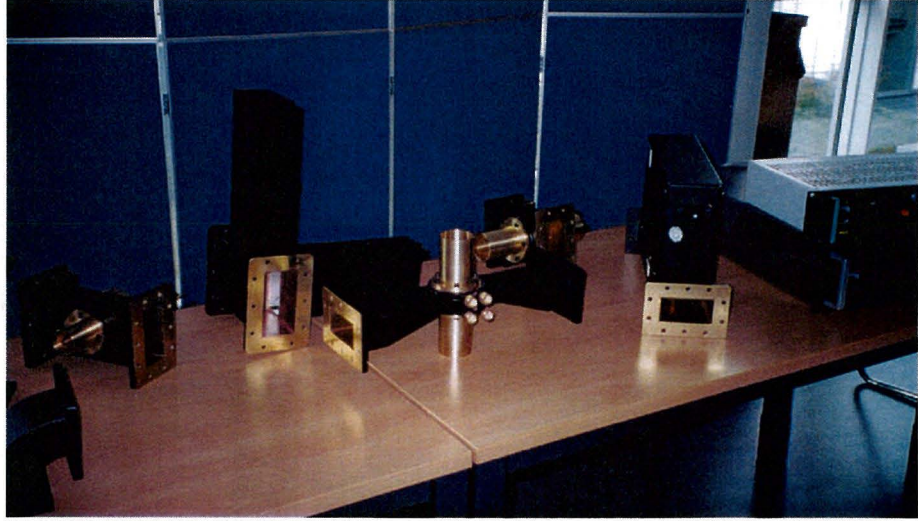


Figure 1.3: A selection of waveguides used in industrial microwave heating.

$$\lambda_g = \frac{2}{\sqrt{\left(\frac{m}{2a_g}\right)^2 + \left(\frac{n}{2b_g}\right)^2}}. \quad (1.1)$$

The  $TE_{10}$  incident mode gives that there is one mode in the  $x$ -coordinate direction (*i.e.* the broad dimension) and the fields are uniform in the  $y$ -coordinate direction (*i.e.* the narrow dimension). For example, in the case of a  $TE_{10}$  WR340 standard rectangular waveguide, the cross-sectional dimensions are given as  $a_g = 0.086\text{ m}$  and  $b_g = 0.043\text{ m}$ . For this setup the cutoff wavelength (1.1) is calculated as:

$$\lambda_g = \frac{2}{\sqrt{\left(\frac{1}{2 \times 0.086}\right)^2 + \left(\frac{0}{2 \times 0.043}\right)^2}} = 0.344\text{ m}. \quad (1.2)$$

From equation (1.1) the cutoff frequency ( $f_g$ ) of the waveguide can be determined according to the relationship [17]:

$$\lambda_g = \frac{c}{f_g}, \quad (1.3)$$

where,  $c = 3 \times 10^8\text{ m/s}$  is the wave speed inside the waveguide. Hence, the

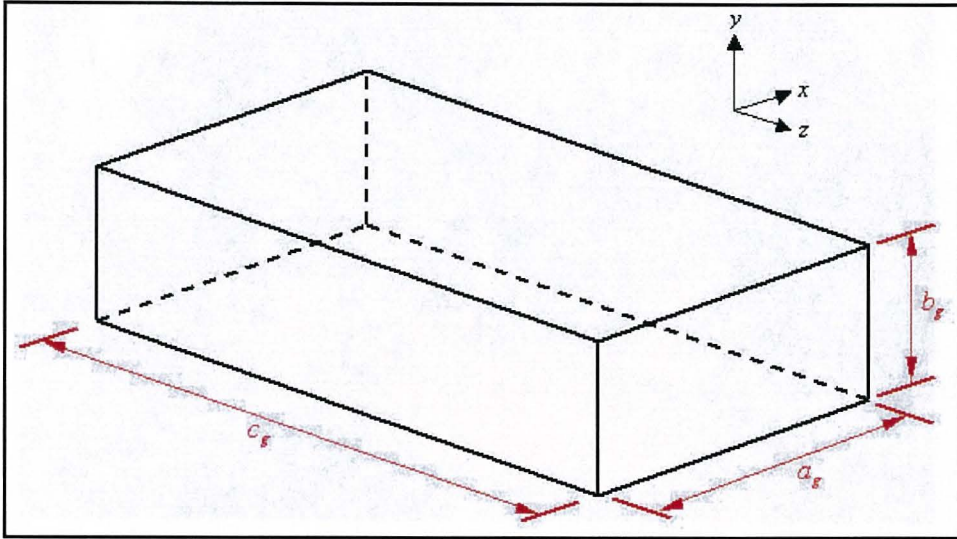


Figure 1.4: A rectangular waveguide with broad dimension  $a_g$ , narrow dimension  $b_g$  and longitudinal dimension  $c_g$ .

cutoff frequency for the  $TE_{10}$  WR340 waveguide is:

$$f_g = \frac{3 \times 10^8}{0.344} \simeq 0.8721 \text{ GHz}. \quad (1.4)$$

Equation (1.4) implies that electromagnetic waves inside the  $TE_{10}$  WR340 waveguide will only propagate for frequencies above  $f_g$ , and for this case, the cutoff frequency is given in (1.4). At frequencies lower than cutoff, the electromagnetic waves are attenuated and the modes inside the waveguide are not propagated. Therefore, it is reasonable and acceptable to excite the waveguide at  $f = 2.45 \text{ GHz}$ , as the modes at this frequency will propagate. To estimate the longitudinal dimension of a waveguide for a certain mode structure the unbounded wavelength ( $\lambda$ ) at this frequency is calculated as:

$$\lambda = \frac{c}{f} = \frac{3 \times 10^8}{2.45 \times 10^9} = 0.122449 \text{ m}. \quad (1.5)$$

Given  $\lambda_g$  from (1.2) and  $\lambda$  from (1.5), the wavelength inside the waveguide,  $\lambda_w$ , is obtained according to the following equation [17]:

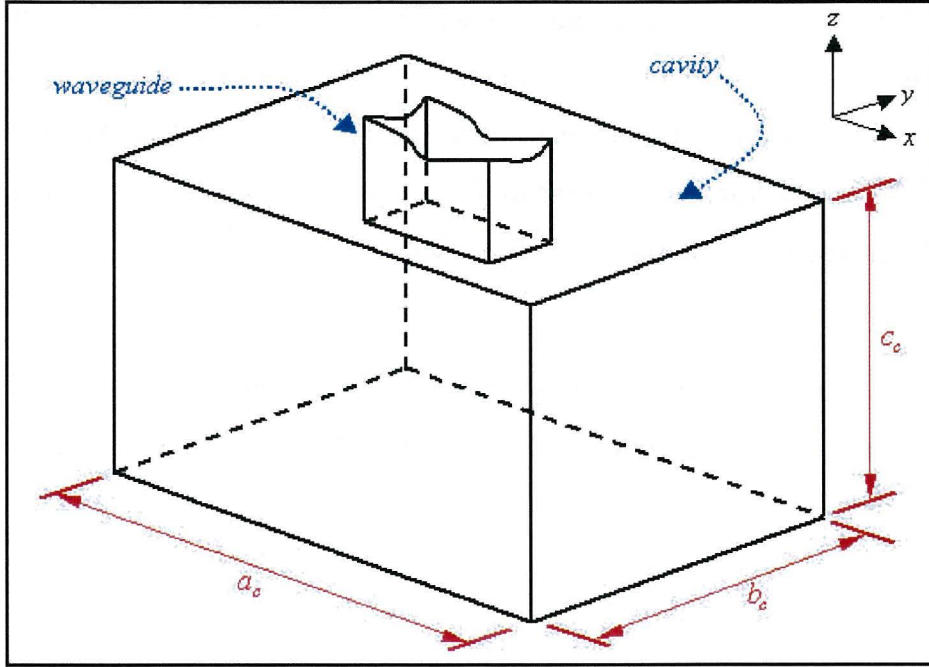


Figure 1.5: A cavity with dimensions  $a_c \times b_c \times c_c$ .

$$\lambda_w = \frac{\lambda}{\sqrt{1 - \left(\frac{\lambda}{\lambda_g}\right)^2}} = \frac{0.122449}{\sqrt{1 - \left(\frac{0.122449}{0.344}\right)^2}} = 0.1310312 \text{ m.} \quad (1.6)$$

In a waveguide, the electromagnetic fields will propagate in the longitudinal dimension, or the  $z$ -coordinate direction. In the most general case, a waveguide may be represented as  $TE_{105}$ , where 5 is the number of modes observed in the  $z$ -coordinate direction. A  $TE_{105}$  WR340 waveguide would have dimensions  $a_g = 0.086 \text{ m}$ ,  $b_g = 0.043 \text{ m}$  and  $c_g = 5 \times \lambda_w = 0.655156 \text{ m}$ , where  $c_g$  is the longitudinal dimension (see Figure 1.4). Since all modes have the same electromagnetic field nature, a  $TE_{101}$  and a  $TE_{105}$  waveguide will introduce the same fields into a cavity, provided that there are no losses through the walls of the waveguide. Due to this observation, future reference to waveguides will be in the form of  $TE_{mn}$ .

Once the waves propagating inside the waveguide have reached the cavity (see

Figure 1.5), new coupled fields and modes are formed inside the applicator and these are uniformly distributed within the empty space. These new modes that are formed according to the dimensions of the cavity are used to classify the nature of the empty applicator either as  $TE_{mnp}$  or  $TM_{mnp}$ , where  $p$  is the number of modes in the longitudinal (or  $z$ ) dimension.

The cavity problem can be considered as an over sized waveguide, and therefore the classification of the cutoff wavelength of the cavity is an extension of (1.1), namely:

$$\lambda_c = \frac{2}{\sqrt{\left(\frac{m}{2a_c}\right)^2 + \left(\frac{n}{2b_c}\right)^2 + \left(\frac{p}{2c_c}\right)^2}}, \quad (1.7)$$

where,  $a_c$ ,  $b_c$  and  $c_c$  are the  $x$ -coordinate,  $y$ -coordinate and  $z$ -coordinate dimensions of the cavity, respectively. An illustration of the cavity dimension is given in Figure 1.5. Similarly to (1.3), the resonant frequency ( $f_c$ ) of the cavity can be determined.

Numerical modelling can help predict the nature of the modes inside a cavity for a particular waveguide-cavity configuration. With the aid of numerical experimentation, the resonant frequency of the cavity can be calculated according to (1.7). Otherwise, given a certain resonant frequency, the dimension of the cavity can be determined for some desired empty cavity electromagnetic mode structure. Ideally, a numerical model that can predict the full electromagnetic fields of the microwave heating apparatus, including the load, should be used in the classification of the cavity.

### **1.1.5 Calibration of the Applicator**

Initially, the applicator is calibrated without any product or load present. Although it is easy to compute the fields that will be present inside an empty applicator, it is not so easy to determine the fields that will be present once a load or product is introduced into that cavity [1].

Numerical techniques have been widely used to compute the electric and magnetic field components inside applicators in the past [3,5,6,8,11-14,19,21-23,31-37,43]. When a product is introduced into the applicator, the nature of the electric and magnetic fields are changed, and new modes are formed. These new modes directly determine how that product will absorb energy (see §1.1.6 for a discussion on material absorptivity). Classical solution methods are very accurate for predicting the power distribution in loads with uniform dielectric properties without temperature dependence and regular product dimensions. However, the classical methods for determining the power distribution inside the load are very sensitive to changes in dielectric material properties and grid discretisations. To cater for these sensitivities, large computing resources are utilised that allow for smaller time stepping in the numerical solver, and a higher spatial resolution of the unknowns. Nevertheless, as more sophisticated numerical schemes are developed and the performance of hardware resources increase, numerical techniques provide an attractive way of predicting the electromagnetic wave evolution inside a loaded cavity.

### **1.1.6 Material Properties**

In electromagnetic computations, when there is a load present inside the microwave heating apparatus, it is essential that the properties of the material are carefully considered. To simulate electromagnetic field behaviour for microwave heating processes, only the permeability ( $\mu$ ) and the relative permittivity ( $\epsilon_r$ ) of

free-space and the dielectric material are used in the computations. Mostly, materials that are heated using microwave technology are dielectrics, which means that the permeability of the material is that of free-space (*i.e.*  $\mu = \mu_0$ ).

Although it is possible to heat materials using microwave technology that have permeabilities that are different to free space, in this thesis only materials that have constant free-space permeability and relative permittivity given as  $\epsilon_r = \epsilon' - \epsilon''j$  are considered. The relative dielectric constant ( $\epsilon'$ ) determines how the electromagnetic waves will interact, and as a result, reflect and refract at the material and free-space interface. The relative loss factor ( $\epsilon''$ ) is a measure of the ability of the material to absorb electromagnetic energy. The higher this constant, the larger the amount of energy being absorbed.

In this work, materials that have constant relative permittivity are investigated in detail. Materials that have temperature dependent permittivities are investigated also, and in this instance the permittivity is given as a function of temperature ( $T$ ) and written as  $\epsilon_r(T) = \epsilon' - \epsilon''(T)j$ . In the case of temperature dependent permittivity, only the dielectric loss factor is dependent on temperature, which means that as the temperature of the material changes, its ability to absorb energy also changes. For most materials, as the temperature inside the material increases, the relative loss factor also increases. Rapid changes in the permittivity can result in rapid changes in the heating of the material, which can be at times unpredictable and is commonly referred to as thermal runaway. Thermal runaway is discussed in detail in §1.1.8.

### 1.1.7 Computing the Dissipated Heat

The computation of the dissipated heat in the load within the cavity is determined by computing the forced heat equation [1, 5, 11, 14, 21, 23, 24]. A number

of assumptions can be made to model the dissipation of heat throughout the load. These assumptions may include Dirichlet, Neumann or Robin boundary conditions for the treatment of the extremities of the load.

The heat equation has been widely studied and has been exhaustively solved in many different applications on both regular and irregular grids or meshes [1, 21, 23]. Irrespective of the assumptions made to the forced heat equation, the challenge still remains with the computation of the dissipated power due to electromagnetic energy within the load (briefly mentioned in §1.1.3). Due to the nature of Maxwell's equations [2] and the corresponding discretisations of the electric and magnetic fields for numerical stability (see §1.2 for a detailed outline), the power inside the load is difficult to compute.

The dissipated power distribution inside the load is obtained directly from the electric field components and the relative loss factor of that load (see §1.1.6 for discussion on dielectric properties). In the case when the relative loss factor is temperature dependent, a feedback process for the solution of the dissipated heat inside the load is required. This feedback process generally involves a number of different solutions to both the electromagnetic fields and the dissipated heat inside the load before convergence is attained within the heating system. Chapter 2 exhibits this feedback process in detail for temperature dependent materials. For most cases studied in thesis, the material properties are not modelled using temperature dependency, and hence, the power distribution is obtained without the implementation of a feedback process.

### 1.1.8 Thermal Runaway

Thermal runaway is mostly observed with materials that have temperature dependent dielectric properties, and these properties increase dramatically with

increasing temperature [25-27]. Thermal runaway is frequently observed in the processing of metals and ceramics, and a glowing or sparking effect is usually associated with it. This happens when a large change in the dielectric property arises during microwave heating, and a coupling effect takes place between the electromagnetic energy and the material, which causes the rapid dissipation of heat (called arcing). Identifying and understanding thermal runaway from a mathematical and physical perspective is therefore an relevant research topic that has also been investigated to some extent in this thesis.

The phenomenon of thermal runaway is analogous to the combustion of an exothermic chemical reactant [27]. The rate at which a chemical reaction proceeds tends to increase with temperature, as a result, if the reaction is exothermic then the heat generated will result in positive feedback that can cause an explosion. The rate at which microwave radiation is absorbed by a material is also temperature-dependent. As a consequence, thermal runaway in this context is the result of an analogous feedback process.

### 1.1.9 Generalisations in the Numerical Methods

In most industrial applications the cavity design in which the heating takes place varies enormously. The assumption on the waveguides is that the walls are perfect conductors, which is to say that there are no losses through the walls of the guide. This is the same for the cavity walls. Although it is possible to model a system that has lossy applicator walls [19], in this study only perfectly conducting walls are studied and implemented. In the case where there may be losses across a conducting surface, an impedance or resistive condition can be adapted to cater for these losses. The reader is referred to [19] for the implementation of this type of applicator boundary condition.

Provided that the electromagnetic waves can be numerically simulated to some degree of accuracy, there still exist other, more complicated issues related to the material. Due to the temperature-dependent material properties, the governing equations are nonlinearly coupled and cannot be solved analytically. The existing models require some innovative computational re-engineering to enable their numerical overheads to be reduced substantially.

## 1.2 Existing Numerical Models in Microwave Heating

The scope of the modelling work conducted in this research work is threefold:

- (a) *An investigation of the use of cell-centred time-domain finite-volume (ccFV-TD) solvers for simulating electromagnetic field behaviour during microwave heating processes.*
- (b) *The analysis of the solution of the frequency dependent Helmholtz equation for predicting the power distribution inside the load.*
- (c) *Calculation of material interface information using the Discrete Fourier Transform (DFT) for the solution of Helmholtz equation.*

The time-domain and frequency-domain solution strategies are interlinked via the boundary information at the free-space and load interfaces. The time-domain solution generates boundary conditions at the material interface, so that the frequency-domain equations can be resolved for the domain of the load alone. Parts (a), (b) and (c) together comprise a new scheme called the Hybrid method, which is outlined in more detail in §1.3 and further in subsequent chapters. Before the hybrid method can be thoroughly investigated, an appreciation and understanding of current, state-of-the-art methods has to be developed.

For domestic and industrial microwave heating applications, the time-averaged electric and magnetic fields have to be computed inside the load. In the case of time-domain solution strategies, the power distribution is directly obtained from the time-averaged electric field. These time-averaged fields are generally computed after a certain number of periods has been realised inside the apparatus.

The computation of the time-averaged electromagnetic fields usually occurs when the system has converged to a desired level of accuracy. The convergence rate is usually monitored on a wave period basis, and the difference observed between periods is calculated to determine the error in the power distribution. Once the fields have reached a standing wave form, the time-averaged fields are computed over a number of periods (*i.e.* one or two electromagnetic wave periods). In this case, an explicit time-marching algorithm is utilised to obtain the power distribution from the time-dependent governing Maxwell's equations [5,12,13,21,31-35]. On the other hand, when obtaining the power distribution from time-harmonic or frequency-dependent equations, the system is usually cast into a system of linear equations. These equations are frequently solved implicitly using some iterative numerical linear algebra solution strategy [19]. From the electric field components obtained in this fashion, the power distribution is calculated in a straightforward and direct manner.

In this work, numerous cell-centred time-domain schemes are presented and assessed in terms of computational speed, phase and amplitude error, in order to identify the most accurate and efficient method that can be used to obtain the time-averaged electric field distribution inside the load in waveguides and cavities. The time-averaged fields are computed for various case studies and are compared to the results obtained using the classical Finite-Difference Time-Domain (FD-TD) [2] solution and to analytic solutions where possible.

The review that follows consists of four subsections, which together provide an outline of recent advances in CEM that can be applied to the microwave heating problem. Typically, discretisation of the electromagnetic equations introduce dispersion, phase and attenuation errors [39-42], which are discussed in detail. The first subsection establishes the governing equations, followed by a succinct outline of the most popular spatial discretisation methods. The spatial discretisation topic is supported by the resolution of the time derivative in the third subsection. The last subsection identifies different approaches for smoothing or correcting the noise apparent in time-marching numerical schemes that do not resolve the unknowns in a state-of-the-art manner, as in the FD-TD methodology [2].

### 1.2.1 Form of the Governing Equations

Over the years, a number of computational models and algorithms have been investigated, developed and enhanced for the solution of Maxwell's equations for a variety of important applications in Science and Engineering [1,25-27,36,43]. Most commonly, researchers implement solution methodologies that simulate instantaneous electromagnetic fields, which are used to obtain the steady-state electromagnetic wave phenomena inside a microwave heating apparatus. This is achieved by time-marching the electric and magnetic field unknowns over the domain of the problem. The time-harmonic or frequency-domain strategies have also been implemented, however, due to their excessive hardware and computational limitations, these methods have not been widely adapted to industrial applications [19]. In the frequency-domain the system is solved using a linear systems solver, where the number of unknowns can be of the order of millions [19].

In their most general form, the time dependent Maxwell's equations are rep-

resented in Table 1.2. For the harmonic representation, Table 1.3 illustrates the phasor form of Maxwell's equation [17, 18].

Law	Integral Form	Differential Form
Ampere	$\oint \mathbf{H} \cdot d\mathbf{l} = \int_s (\mathbf{J} + \frac{\partial \mathbf{D}}{\partial t}) \cdot d\mathbf{s} = i$	$\nabla \times \mathbf{H} = \mathbf{J} + \frac{\partial \mathbf{D}}{\partial t}$
Faraday	$\oint \mathbf{E} \cdot d\mathbf{l} = - \int_s \frac{\partial \mathbf{B}}{\partial t} \cdot d\mathbf{s} = v$	$\nabla \times \mathbf{E} = - \frac{\partial \mathbf{B}}{\partial t}$
Gauss for Electric Fields	$\oint \mathbf{D} \cdot d\mathbf{s} = \int_v \rho dv = q$	$\nabla \cdot \mathbf{D} = \rho$
Gauss for Magnetic Fields	$\oint \mathbf{B} \cdot d\mathbf{s} = 0$	$\nabla \cdot \mathbf{B} = 0$

Table 1.2: Time-domain representation of the governing equations.

In Tables 1.2 and 1.3 the constitutive relations are given as:

$$\mathbf{D} = \epsilon \mathbf{E}, \quad \mathbf{B} = \mu \mathbf{H}, \quad \mathbf{J} = \sigma \mathbf{E}. \quad (1.8)$$

Industrial microwave heating applications are current free, implying that  $\rho = 0$ . For this reason, the equations in Tables 1.2 and 1.3 that are related to the divergence of both  $\mathbf{D}$  and  $\mathbf{B}$  are set to zero.

In high frequency microwave applications, often the frequency-domain equations are rewritten in a form that satisfies the divergence condition. By taking the curl of both the Ampere and Faraday laws in Table 1.3, and eliminating either  $\mathbf{E}$  or  $\mathbf{H}$ , the following two equations are obtained for the electric and magnetic fields using the appropriate vector identities:

$$\nabla^2 \mathbf{E} + k^2 \mathbf{E} = 0, \quad (1.9)$$

$$\nabla^2 \mathbf{H} + k^2 \mathbf{H} = 0, \quad (1.10)$$

where, the wave number is given by

$$k^2 = \omega^2 \mu \epsilon - j \omega \mu \sigma.$$

Law	Integral Form	Differential Form
Ampere	$\oint \mathbf{H} \cdot d\mathbf{l} = (\sigma + j\omega\epsilon) \int_s \mathbf{E} \cdot ds$	$\nabla \times \mathbf{H} = (\sigma + j\omega\epsilon) \mathbf{E}$
Faraday	$\oint \mathbf{E} \cdot d\mathbf{l} = -j\omega\mu \int_s \mathbf{H} \cdot ds$	$\nabla \times \mathbf{E} = -j\omega\mu \mathbf{H}$
Gauss for Electric Fields	$\oint \mathbf{D} \cdot ds = \int_v \rho dv$	$\nabla \cdot \mathbf{D} = \rho$
Gauss for Magnetic Fields	$\oint \mathbf{B} \cdot ds = 0$	$\nabla \cdot \mathbf{B} = 0$

Table 1.3: Frequency-domain representation of the governing equations.

Equations (1.9) and (1.10) are the Helmholtz equations for the electric and magnetic fields [17, 18], respectively. Researchers in the past [8, 14, 19, 36, 37] have solved only (1.9) for the electric field inside the microwave heating apparatus, since the electric field has been decoupled from the magnetic field and the power is obtained directly from the electric field alone.

It should be noted that if (1.9) is solved everywhere in the domain, including the waveguide, cavity and material, then the resultant system of linear equations is ill-conditioned and requires the implementation of sophisticated numerical linear equations solvers to obtain the approximate electric field solution at a particular frequency [19]. Adaptive iterative techniques that use left and right preconditioning have to be utilised to obtain the electric field solutions inside the material. Although, it is possible to condition (via left and right preconditioning) the system matrix that performs well numerically, a small change in the layout of the problem can cause the system to break down numerically [38].

### 1.2.2 Spatial Discretisation Strategies

As with many numerical solution strategies for any type of governing equations, domain discretisation is adopted to resolve the unknowns at different spatial locations [24, 29, 30, 39, 44, 45, 47]. Knowledge of discretisation errors is essential before breaking the problem into smaller cells that are computationally stable.

Any type of discretisation will introduce errors into the problem, and therefore, the ability to properly manage these errors is a prerequisite to solving any application. In the numerical solution strategy discussed in this section, spatial discretisation can introduce either dissipation or dispersion errors into the numerical scheme [39].

The way in which the governing equations of Tables 1.2 and 1.3 in §1.2.1 are represented determines the spatial discretisation that can be utilised to accommodate the numerical solution strategy. Specifically, if the differential form of the governing Maxwell's equations of Table 1.2 are discretised, then a system of equations is obtained, for which the partial differential operator in space has to be approximated for some spatial location. Consequently, the accuracy of the underlying scheme is a function of the type and order of the spatial discretisation.

### Point Discretisation

Most frequently, Taylor series approximations are used to discretise the partial spatial derivatives to achieve some level of accuracy and a number of papers have been published in this area [5,28,31-35]. As an example, by taking the  $x$ -component of the Ampere law for the differential form in Table 1.2, the following partial differential equation is obtained according to the constitutive relations of (1.8):

$$\mu \frac{\partial H_x}{\partial t} = \frac{\partial E_z}{\partial y} - \frac{\partial E_y}{\partial z}. \quad (1.11)$$

Equation (1.11) relates the change in magnetic field in time to the change in electric field in space on an  $x$ ,  $y$  and  $z$ -coordinate system. As (1.11) gives a continuous representation of the behaviour of the  $x$ -component of the magnetic field ( $H_x$ ), spatial discretisation in the form of Taylor approximations is used to resolve the spatial derivatives in the  $y$  and  $z$ -coordinate dimensions in (1.11). A

first order approximation for  $\frac{\partial E_z}{\partial y}$  and  $\frac{\partial E_y}{\partial z}$  in (1.11) is given as:

$$\frac{\partial E_z}{\partial y} \simeq \frac{E_{z(i,j+1,k)} - E_{z(i,j,k)}}{\delta_y} = \frac{E_{z(i,j,k)} - E_{z(i,j-1,k)}}{\delta_y}, \quad (1.12)$$

$$\frac{\partial E_y}{\partial z} \simeq \frac{E_{y(i,j,k+1)} - E_{y(i,j,k)}}{\delta_z} = \frac{E_{y(i,j,k)} - E_{y(i,j,k-1)}}{\delta_z}. \quad (1.13)$$

Generally, equations (1.12) and (1.13) are not used in the numerical modelling of electromagnetic waves, as the first order schemes have large wave dissipation errors associated with them. More frequently, a second order spatial approximation is implemented for  $\frac{\partial E_z}{\partial y}$  and  $\frac{\partial E_y}{\partial z}$  in (1.11) and expressed as:

$$\frac{\partial E_z}{\partial y} \simeq \frac{E_{z(i,j+1,k)} - E_{z(i,j-1,k)}}{2\delta_y}, \quad (1.14)$$

$$\frac{\partial E_y}{\partial z} \simeq \frac{E_{y(i,j,k+1)} - E_{y(i,j,k-1)}}{2\delta_z}. \quad (1.15)$$

Substituting equations (1.14) and (1.15) into (1.11) resolves the partial space operators onto the discrete domain to obtain a differential equation in time:

$$\mu \frac{\partial H_x}{\partial t} = \left( \frac{E_{z(i,j+1,k)} - E_{z(i,j-1,k)}}{2\delta_y} \right) - \left( \frac{E_{y(i,j,k+1)} - E_{y(i,j,k-1)}}{2\delta_z} \right). \quad (1.16)$$

In terms of the discretisation strategy used in (1.16), the cells are regular and are located according to standard  $(i, j, k)$  referencing, as shown for  $E_y$  in Figure 1.6. It is assumed in this case that the unknowns  $E_y$  and  $E_z$  in (1.16) are located at the centres of these finite Cartesian cells. Therefore, a partial derivative in a certain Cartesian direction in space can be approximated by two adjacent cell unknowns in that direction, while fixing all other components. A stability analysis on (1.16) can be performed to show that this type of spatial discretisation can introduce errors into the numerical scheme [39]. In the case of Yee's method [2], the electric field spatial locations are offset by half a cell, implying that rather than locating the electric field components on cell centres, the components have been relocated to cell edges. As a consequence, the spatial partial derivatives of

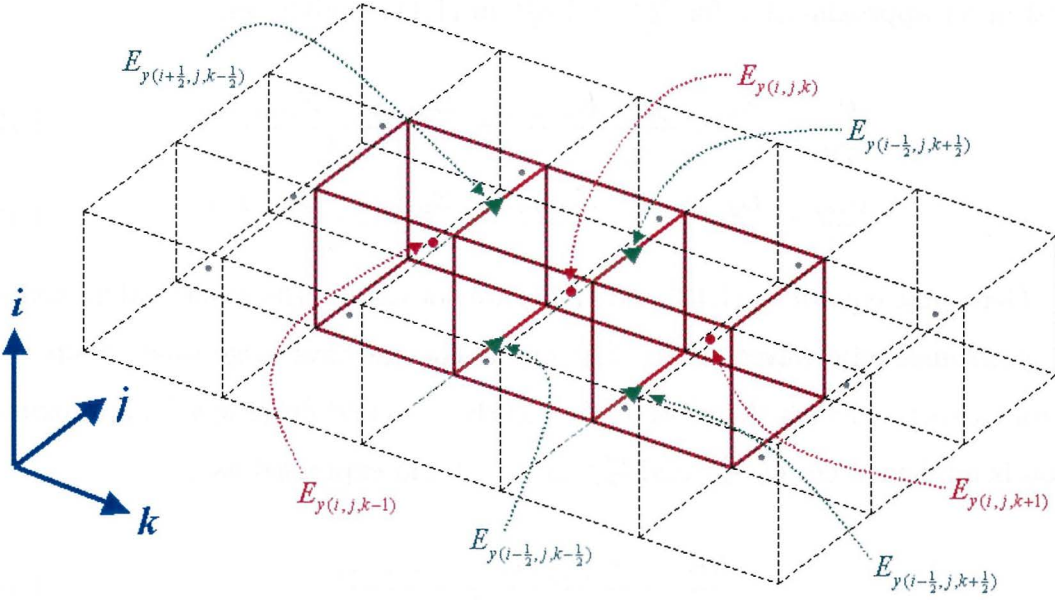


Figure 1.6: A layer of the Cartesian discretisation of the unknown  $E_y$  for an  $(i, j, k)$  stencil.

(1.11) have to be approximated at the edges of each Cartesian cell. Equations (1.14) and (1.15) for a regular cell are reformulated and represented on a cell edge as follows:

$$\frac{\partial E_z}{\partial y} \simeq \frac{E_{z(i+\frac{1}{2}, j+\frac{1}{2}, k)} - E_{z(i+\frac{1}{2}, j-\frac{1}{2}, k)}}{\delta_y}, \quad (1.17)$$

$$\frac{\partial E_y}{\partial z} \simeq \frac{E_{y(i+\frac{1}{2}, j, k+\frac{1}{2})} - E_{y(i+\frac{1}{2}, j, k-\frac{1}{2})}}{\delta_z}. \quad (1.18)$$

Equation (1.11) is rewritten in the following form when (1.17) and (1.18) are used in the substitutions:

$$\mu \frac{\partial H_x}{\partial t} = \left( \frac{E_{z(i+\frac{1}{2}, j+\frac{1}{2}, k)} - E_{z(i+\frac{1}{2}, j-\frac{1}{2}, k)}}{\delta_y} \right) - \left( \frac{E_{y(i+\frac{1}{2}, j, k+\frac{1}{2})} - E_{y(i+\frac{1}{2}, j, k-\frac{1}{2})}}{\delta_z} \right). \quad (1.19)$$

In (1.19) the derivative term in time ( $\frac{\partial H_x}{\partial t}$ ) has not been resolved at any particular spatial location. The location where this derivative is approximated is

also very important, and this will be discussed in §1.2.3.

To this point, the spatial change in the electric field has been considered. Similarly, the magnetic fields can be approximated from Faraday's differential form (see Table 1.2). In a similar manner outlined for  $\frac{\partial H_x}{\partial t}$ , all of the spatial components of the electric and magnetic fields in terms can be discretised. When the magnetic field components are resolved in space, they are stored on cell face centres, as the staggering between the electric and magnetic field components also reduces error in the numerical scheme. It can be shown from error analysis of the staggered schemes that some of the error terms are removed when the unknowns have been staggered in both space and time [13]. Once this is achieved, the time derivatives are resolved to some degree of accuracy, which is considered in §1.2.3.

### Finite-Volume Discretisation

In the spatial discretisations discussed throughout the previous sections the differential form of the Maxwell's equations have been resolved and approximated. A finite Cartesian cell within the domain has also been identified and referenced as  $(i, j, k)$ . This particular regular cell has certain dimensions and volume, given as  $\delta_x \times \delta_y \times \delta_z = \delta_v$ . By allowing the cell to have volume  $\delta_v$ , and only working with the  $x$ -component of the magnetic field as before, the differential form of Ampere's law in Table 1.2 is now integrated over the volume of the cell:

$$\iiint_v \mu \frac{\partial H_x}{\partial t} \delta v = - \iiint_v (\nabla \times \mathbf{E})_x \delta v. \quad (1.20)$$

In equation (1.20) the left hand side can be resolved easily over the volume, since the time derivative is independent of the volume. The  $\frac{\partial H_x}{\partial t}$  term is cell average for the  $(i, j, k)$  cell and written as:

$$\delta_v \mu \frac{\partial \bar{H}_x}{\partial t} = \mu \frac{\partial}{\partial t} \iiint_v H_x \partial v. \quad (1.21)$$

On the other hand, the right hand side of (1.20) is first rewritten according to Stokes' theorem [46] before the discretisation in space is applied:

$$\mu \delta_v \frac{\partial \bar{H}_x}{\partial t} = - \iint_s (\mathbf{n} \times \mathbf{E}_f)_x \partial s, \quad (1.22)$$

where,  $\mathbf{E}_f$  is the electric field on the surface of the cell. The surface integral in (1.22) is resolved over the cell, which gives on a well defined cell (*i.e.* a cell which has faces that are clearly identified) a sum over all faces ( $f$ ):

$$\mu \delta_v \frac{\partial \bar{H}_x}{\partial t} = - \sum_f (\mathbf{n} \times \mathbf{E}_f)_x \delta_f. \quad (1.23)$$

The mid-point integration rule was adopted for the integral approximation in (1.23). This scheme is known to be second order accurate when the value of the unknown  $(\mathbf{n} \times \mathbf{E}_f)_x$  is computed exactly. As a consequence of this limitation, an estimate of  $\mathbf{E}_f$  is sought on the cell face with high accuracy to enable the scheme to retain the second order spatial discretisation. Assuming that the normal ( $\mathbf{n}$ ) can be resolved into components as  $\mathbf{n} = (n_x, n_y, n_z)$ , equation (1.23) is simplified and expanded as:

$$\mu \delta_v \frac{\partial \bar{H}_x}{\partial t} = \sum_f (n_z E_y - n_y E_z)_f \delta_f. \quad (1.24)$$

On a Cartesian cell, (1.24) contributes only to faces that have  $y$  or  $z$ -coordinate normal components. By expanding about the faces of cell  $(i, j, k)$  and locating the unknowns on cell edges in the case of the electric field components, it can be shown that (1.24) reduces to (1.19). Given that the unknowns are located at the same spatial location in both instances, the two strategies yield the same outcome for a Cartesian mesh. It should be noted that the focus here is the development

of a numerical model that can be used on grids that are non-hexahedral, for example consisting of tetrahedra, and (1.23) is more suited to this type of mesh, as opposed to (1.11).

Equation (1.23) represents the  $x$ -component of the magnetic field in terms of the electric field for an unstructured cell. It is important to note that in the case of (1.23), all of the electric field components are required right on the cell faces. The location of the unknowns on the cell faces is very important, because on a particular cell face the different locations of an unknown can affect the size of the spatial discretisation errors significantly [46]. Similarly, when the discretisation of Faraday's law in Table 1.2 is performed, it can be seen that the magnetic fields are also required at the same facial locations of a given cell.

Since (1.23) is suitable for irregular grids, the positioning of the electric and magnetic field components has to be considered carefully. By locating the three electric field components and three magnetic field components on cell faces, thirty six components are required for a given Cartesian cell, and twenty four components are required for a tetrahedral cell, which has four triangular faces. Other cell structures can be utilised, but in any case, the smallest three-dimensional cell that can be formed is a tetrahedron. Although it is possible to use strategies that do not necessarily store all components of all fields within all cells, an approach that staggers the unknowns in space tends to use more computer memory than a cell-centred approach.

This thesis investigates methods that can store all of the components of the electric and magnetic field unknowns at the cell-centre. Using numerical least squares function reconstruction techniques, approximate facial values for (1.23) are generated from unknowns located at cell-centres adjacent to that face, and in the neighbourhood of that face. Various strategies are investigated to capture

the electromagnetic field behaviour inside the microwave applicator.

Considering industrial microwave heating problems that typically consist of millions of discrete cells, the discretisation can clearly impact the performance and computational execution time of the scheme employed. Therefore, cell-centred spatial locality is favourable on non-regular type grids for a number of reasons. Mainly, it is easier to manage cells that have unknowns at their centres, dual cells are created more easily (these are cells that are formed around existing cells to predict unknowns at different locations) and usually saves on the amount of storage. The drawbacks of cell-centred approaches are that since the unknowns are not staggered in space (*i.e.* the unknowns are not located at different spatial locations within a cell), greater discretisation errors are introduced, and it is harder to achieve stability in the numerical scheme.

For the reasons outlined in the previous paragraph and because the electric and magnetic fields are coupled (see Tables 1.2 and 1.3), researchers have investigated other approaches to resolve the power distribution inside a given load in a microwave heating apparatus. The Helmholtz equations (1.9) and (1.10) tend to have spatial stability due to the nature of the equations, and once the discrete point forms are established, the equations can be resolved using an implicit solution strategy. As the power dissipated inside the load is obtained from the electric field components directly, only (1.9) is solved. The  $x$ -component of the electric field in the frequency domain is given by the following partial differential equation:

$$\frac{\partial^2 E_x}{\partial x^2} + \frac{\partial^2 E_x}{\partial y^2} + \frac{\partial^2 E_x}{\partial z^2} + k^2 E_x = 0. \quad (1.25)$$

On a regular Cartesian grid, second order spatial discretisations of  $\frac{\partial^2 E_x}{\partial x^2}$ ,  $\frac{\partial^2 E_x}{\partial y^2}$  and  $\frac{\partial^2 E_x}{\partial z^2}$  according to the Taylor expansion are respectively given as:

$$\frac{\partial^2 E_x}{\partial x^2} \simeq \frac{E_{x(i+1,j,k)} - 2E_{x(i,j,k)} + E_{x(i-1,j,k)}}{\delta_x^2}, \quad (1.26)$$

$$\frac{\partial^2 E_x}{\partial y^2} \simeq \frac{E_{x(i,j+1,k)} - 2E_{x(i,j,k)} + E_{x(i,j-1,k)}}{\delta_y^2}, \quad (1.27)$$

$$\frac{\partial^2 E_x}{\partial z^2} \simeq \frac{E_{x(i,j,k+1)} - 2E_{x(i,j,k)} + E_{x(i,j,k-1)}}{\delta_z^2}. \quad (1.28)$$

Substituting (1.26-1.28) into (1.25) and collecting like terms, the discrete finite-difference analogue of (1.25) is obtained according to the finite difference stencil:

$$\begin{aligned} & \frac{1}{\delta_z^2} E_{x(i,j,k+1)} + \frac{1}{\delta_y^2} E_{x(i,j+1,k)} + \frac{1}{\delta_x^2} E_{x(i+1,j,k)} \\ & - 2 \left( \frac{1}{\delta_x^2} + \frac{1}{\delta_y^2} + \frac{1}{\delta_z^2} + \frac{k^2}{2} \right) E_{x(i,j,k)} \\ & + \frac{1}{\delta_x^2} E_{x(i-1,j,k)} + \frac{1}{\delta_y^2} E_{x(i,j-1,k)} + \frac{1}{\delta_z^2} E_{x(i,j,k-1)} = 0. \end{aligned} \quad (1.29)$$

When all cells in the computational domain are visited, (1.29) generates the matrix system  $\mathbf{Ax} = \mathbf{b}$ , where  $\mathbf{A}$  is the coefficient matrix,  $\mathbf{b}$  is the right hand vector that includes the boundary information and  $\mathbf{x}$  is the vector that represents the unknowns. In (1.29) the unknown is  $E_x$ , but can easily be adapted to  $E_y$  and  $E_z$ , provided that the boundary condition implementation does not significantly change the entries of  $\mathbf{A}$ . In the situation when the object is touching one or more of the faces of the cavity, then it is possible that the coefficient matrix will take a different form to cater for the existence of the different electric field components on the cavity walls.

## Solution of Linear Systems of Equations

For frequency-domain solution strategies, the discretisation of (1.9) yields a system of linear equations that has a  $k^2$  contribution to the diagonal terms of the coefficient matrix. The implementation of the boundary conditions can introduce

entries into the coefficient matrix that make it more difficult to treat numerically, and usually implicit partial pivoting is necessary. For these reasons, the system of linear equations can become ill-conditioned and the condition number of the matrix is a function of the way the boundary conditions were implemented and the magnitude of  $k^2$ .

In equation (1.29) when  $k^2 = 0$  then the solution to the system of equations becomes equivalent to the solution of the Laplace equation. The discretisation of the Laplace equation can be solved easily using direct methods like LU factorisation, shifted LU factorisation and with incomplete factorisation given some level of fill, where the solution is iteratively refined [48]. All of these methods will converge and provide very accurate solutions when there is no contribution on the diagonal from the  $k^2$  term.

If the effect of  $k^2$  is negligible compared to the other terms on the diagonal, then the solution is still obtained relatively easily and the direct methods will still perform well. For values of  $|k|^2 \ll \frac{1}{\delta_x^2} + \frac{1}{\delta_y^2} + \frac{1}{\delta_z^2}$  iterative methods can also be employed. Methods like Jacobi, Gauss-Seidel and Successive Over Relaxation (SOR) [48] will perform well in this range of  $|k|$ . Once the  $k^2$  term becomes large enough to significantly affect the eigenvalue spectrum of the coefficient matrix  $\mathbf{A}$ , and hence the condition number  $k_2(\mathbf{A})$ , then the solution to the problem is no longer straightforward and some scaling strategy must be employed. In microwave heating problems, because the frequency is in the *GHz* range and  $k$  is a function of frequency, there will always be considerable contribution from the  $k^2$  term in the Helmholtz equation (1.9). It should also be noted that  $k \in \mathbb{C}$ , which implies that  $\mathbf{A} \in \mathbb{C}^{n \times n}$ , where  $n$  is the dimension of the matrix. To obtain the approximate solution, complex arithmetic is used to resolve the system of linear equations.

The condition number of the coefficient matrix ( $\mathbf{A}$ ) is obtained from the following expression:

$$k_2(\mathbf{A}) = \|\mathbf{A}\|_2 \|\mathbf{A}^{-1}\|_2 = \frac{\sigma_{\max}}{\sigma_{\min}}, \quad \|\mathbf{A}\|_2 = \sqrt{\rho_\sigma(\mathbf{A}^H \mathbf{A})} = \sigma_{\max}, \quad (1.30)$$

where,  $\sigma_{\min}$  and  $\sigma_{\max}$  are the minimum and maximum singular values of  $\mathbf{A}^H \mathbf{A}$ , respectively. Generally, the coefficient matrix  $\mathbf{A}$  generated from (1.29) either has a very large or very small singular value, or both, implying that (1.30) tends to be such that  $k_2(\mathbf{A}) \gg 1$ . It is well known that for large condition numbers (*e.g.*  $k_2(\mathbf{A}) > 1000$ ) iterative processes like Jacobi, Gauss-Seidel and SOR will not converge to the solution.

Krylov subspace methods [38] usually perform well, and in most cases can obtain the solution to the Helmholtz equation accurately. Some of the Krylov subspace methods that have been used in the past to solve the Helmholtz equations are the Conjugate Gradient (CG), Bi-Conjugate Gradient (biCG), Minimum Residual (minRES), Quasi-Minimal Residual (QMR) and Generalised Minimum Residual (GMRES) methods [19]. Depending on whether the coefficient matrix ( $\mathbf{A}$ ) is symmetric or non-symmetric, at least one of these algorithms can be used with complex arithmetic.

All iterative methods perform better when the spectral radius of the coefficient matrix is narrow. Therefore, preconditioning on either the left or right should be used to reduce the condition number of the resultant coefficient matrix:

$$\mathbf{M}_l \mathbf{A} \mathbf{M}_r \mathbf{M}_r^{-1} \mathbf{x} = \mathbf{M}_l \mathbf{b}. \quad (1.31)$$

Equation (1.31) reduces to the original system of equations ( $\mathbf{A}\mathbf{x} = \mathbf{b}$ ) when the left preconditioner ( $\mathbf{M}_l$ ) and the right preconditioner ( $\mathbf{M}_r$ ) are set to the identity matrix ( $\mathbf{I}$ ) of the same dimension as  $\mathbf{A}$ . Otherwise, when both  $\mathbf{M}_l$  and

$\mathbf{M}_r$  are not set to the identity matrix, then the system is solved via the following two steps:

$$\mathbf{M}_l \mathbf{A} \mathbf{M}_r \mathbf{y} = \mathbf{M}_l \mathbf{b}, \quad (1.32)$$

$$\mathbf{x} = \mathbf{M}_r \mathbf{y}. \quad (1.33)$$

In (1.32),  $\mathbf{M}_l$  and  $\mathbf{M}_r$  are chosen such that  $k_2(\mathbf{M}_l \mathbf{A} \mathbf{M}_r) \ll k_2(\mathbf{A})$ . If this can be achieved, then the system of equations in (1.32) will converge to the solution much more rapidly than in the case where the coefficient matrix has not been preconditioned. Usually either left or right preconditioning is used, and not both, unless the system cannot be solved otherwise. The easiest way to precondition such a system is to use a diagonal left preconditioner as follows:

$$\mathbf{D}^{-1} \mathbf{A} \mathbf{x} = \mathbf{D}^{-1} \mathbf{b}. \quad (1.34)$$

Special care must be taken when the left preconditioner is used with numerical methods like GMRES, as this alters the right hand vector prior to the generation of the Krylov subspace, and as a consequence, the calculated residual through the iterations of the GMRES scheme is not representative of the true system residual. Therefore, right preconditioning is recommended where possible, but nevertheless (1.34) is cast into an augmented system, which has the same solution:

$$\hat{\mathbf{A}} \mathbf{x} = \hat{\mathbf{b}}, \quad (1.35)$$

where,

$$\hat{\mathbf{A}} = \mathbf{D}^{-1} \mathbf{A}, \quad \hat{\mathbf{b}} = \mathbf{D}^{-1} \mathbf{b}. \quad (1.36)$$

The solution to the linear system of equations can now be performed using the GMRES method [51] on the preconditioned system in (1.35). There is a tendency for this process to converge well, provided the condition number  $k_2(\hat{\mathbf{A}})$

is sufficiently small. Normally explicit preconditioning is not practiced, but rather the system is implicitly preconditioned as the basis vectors for the solution are generated, as in the preconditioned GMRES method [51]. This can save large amounts of computational time on matrices that have hundreds of thousands of entries, because instead of an initial matrix-matrix multiplication, only a finite number of matrix-vector multiplications are calculated. Also in this work it was found that by using the Incomplete Orthogonalisation Method (IOM) in GMRES [38], the solution to the problem was obtained much more rapidly. GMRES with IOM is referred to in the literature as Quasi-GMRES and is outlined in more detail in Chapter 6.

### 1.2.3 Resolution of the Time Derivative

In the previous section the spatial discretisation of the system was considered. To obtain a highly accurate numerical scheme to resolve the electromagnetic phenomena inside a microwave heating apparatus, high accuracy in both the spatial and time discretisations has to be accomplished [39]. A scheme that takes advantage of both the spatial discretisation of the domain and the time stepping of the numerical algorithm will achieve the best results for industrial microwave heating problems. By carefully selecting the time-marching and spatial discretisation strategies, error in the time-space discretisation can be significantly reduced.

When considering time discretisation of the governing electromagnetic Maxwell's equations (see Table 1.2), numerical discretisation errors can be introduced. These errors are usually related to the speed of the wave front and the phase of the electromagnetic waves. Unlike in radar communication systems, in microwave heating problems time averaged fields are computed to obtain the power distribution inside the load, and as a result the wave front speed error is usually of little concern. Although, the phase error can affect the final solution, it is easier

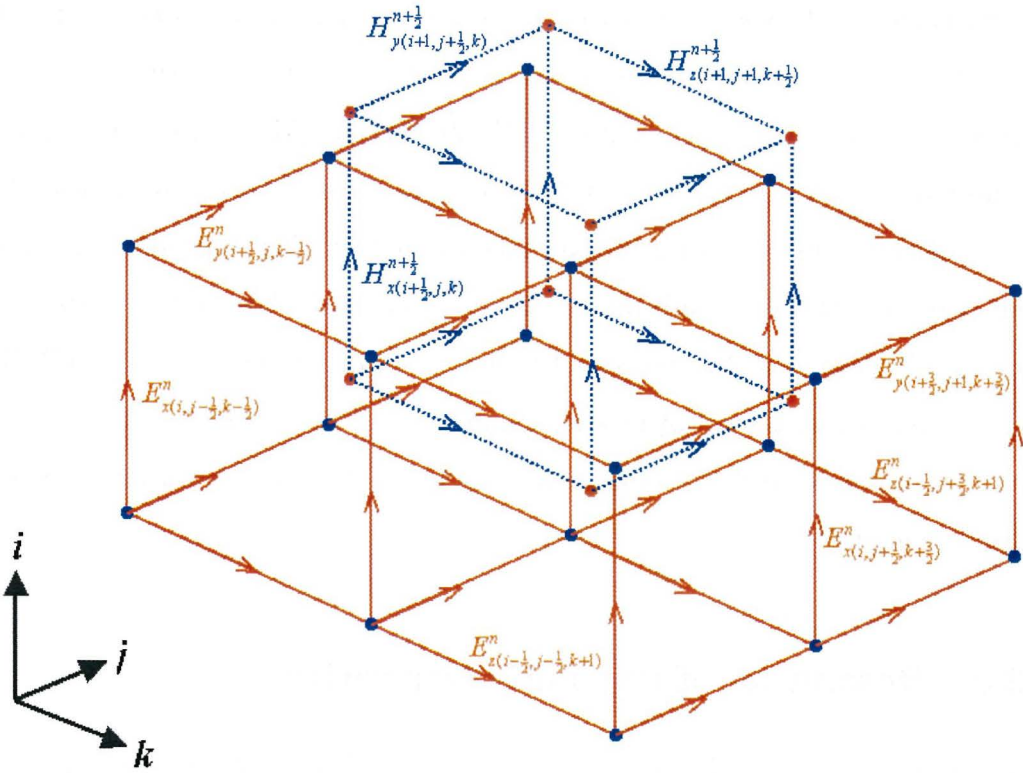


Figure 1.7: The locations of the different unknowns and their time levels. *Orange* corresponds to electric field locations and *blue* represents the magnetic field locations.

to manage the errors related to time discretisation than it is to control the errors related to the different spatial discretisations.

Firstly, assume that the discretisation technique for the spatial terms in the governing equations has been decided. For example, consider equation (1.19) where the electric fields have been discretised over a regular Cartesian cell. In this case the electric field components are located on different cell edges, as discussed in §1.2.2. Similarly to the spatial discretisation approximations for the partial differential operator, the space derivatives are approximated. Before the approximation for the time derivative is substituted into (1.19), the equation is

fixed at time level  $n$ :

$$\mu \frac{\partial H_x^n}{\partial t} = \left( \frac{E_{z(i+\frac{1}{2}, j+\frac{1}{2}, k)}^n - E_{z(i+\frac{1}{2}, j-\frac{1}{2}, k)}^n}{\delta_y} \right) - \left( \frac{E_{y(i+\frac{1}{2}, j, k+\frac{1}{2})}^n - E_{y(i+\frac{1}{2}, j, k-\frac{1}{2})}^n}{\delta_z} \right). \quad (1.37)$$

In (1.37) the  $\frac{\partial H_x^n}{\partial t}$  term has to be approximated. Using a similar strategy to (1.17) and (1.18), the second order Taylor series approximation is written as [31]:

$$\frac{\partial H_x^n}{\partial t} \simeq \frac{H_x^{n+\frac{1}{2}} - H_x^{n-\frac{1}{2}}}{\delta_t}. \quad (1.38)$$

Since for spatial stability purposes the magnetic field components are located on the cell face centres, equation (1.38) is rewritten for a Cartesian cell in the following point form:

$$\frac{\partial H_{x(i+\frac{1}{2}, j, k)}^n}{\partial t} \simeq \frac{H_{x(i+\frac{1}{2}, j, k)}^{n+\frac{1}{2}} - H_{x(i+\frac{1}{2}, j, k)}^{n-\frac{1}{2}}}{\delta_t}. \quad (1.39)$$

Substituting (1.39) into (1.37) and rearranging yields the Finite-Difference Time-Domain (FD-TD) method for the  $x$ -component of the magnetic field [2], namely:

$$H_{x(i+\frac{1}{2}, j, k)}^{n+\frac{1}{2}} = H_{x(i+\frac{1}{2}, j, k)}^{n-\frac{1}{2}} + \frac{\delta_t}{\mu \delta_y} \left( E_{z(i+\frac{1}{2}, j+\frac{1}{2}, k)}^n - E_{z(i+\frac{1}{2}, j-\frac{1}{2}, k)}^n \right) - \frac{\delta_t}{\mu \delta_z} \left( E_{y(i+\frac{1}{2}, j, k+\frac{1}{2})}^n - E_{y(i+\frac{1}{2}, j, k-\frac{1}{2})}^n \right). \quad (1.40)$$

Figure 1.7 is an illustration of the different spatial and time locations of the electric and magnetic field components for the FD-TD method implemented on a Cartesian mesh. In the figure, the orange line represents the line of action of the electric field components, while the dashed blue line is the line of action of the magnetic field components. It can be seen that the electric field components are lagging the magnetic field components by half a time step. The dashed line in Figure 1.7 represents a fictitious cell (*i.e.* a cell that has been artificially created

to cater for the time marching scheme), and the continuous line is a representation of the mesh used to discretise the problem domain.

The method used to resolve the partial time derivative in (1.37) is commonly referred to as the Leapfrog time marching algorithm, where one unknown (in this case the electric field) is displaced by half a time step from the other unknown (the magnetic field). In a similar manner, the other components in Ampere's and Faraday's differential forms in Table 1.2 can be obtained. This type of approach to resolve the Maxwell's equations is highly stable, and is very accurate on Cartesian grids [1].

Leapfrog time marching algorithms have been widely implemented in many computational modelling fields. The Leapfrog discretisation is unmatched by any other type of time marching strategy for the same computational cost and accuracy. Although, when considering cell-centred in space discretisations, where the derivatives in time have to be approximated, it may be necessary to employ higher order time marching algorithms. Runge-Kutta multi-step ordinary differential equations solvers have been previously implemented. In this thesis, the cell-centred time domain solvers (1.23) are analysed and discretised in time using Leapfrog and higher order Runge-Kutta methods [48, 49, 50].

Runge-Kutta (RK) methods can be used with both (1.19) and (1.24). Generally second order Runge-Kutta (RK2) methods are not implemented, because this technique very much resembles the Leapfrog time-discretisation strategy in terms of numerical error and performance. Typically, higher order RK methods often are implemented with these equations (usually third and fourth order, *i.e.* RK3 and RK4). In the third order case (RK3), the solution from  $H_x^n$  to  $H_x^{n+1}$  is obtained by substituting  $\frac{\partial H_x^n}{\partial t}$  into the RK3 scheme:

$$\begin{aligned}
H_x^{n+\frac{1}{3}} &= H_x^n + \frac{\delta_t}{3} \frac{\partial H_x^n}{\partial t}, \\
H_x^{n+\frac{2}{3}} &= H_x^n + \frac{2\delta_t}{3} \frac{\partial H_x^{n+\frac{1}{3}}}{\partial t}, \\
H_x^{n+1} &= H_x^n + \frac{\delta_t}{4} \left( 3 \frac{\partial H_x^{n+\frac{2}{3}}}{\partial t} + \frac{\partial H_x^n}{\partial t} \right). \tag{1.41}
\end{aligned}$$

A 4<sup>th</sup> order Runge-Kutta (RK4) method can be implemented also, and is formulated below:

$$\begin{aligned}
\hat{H}_x^{n+\frac{1}{2}} &= H_x^n + \frac{\delta_t}{2} \frac{\partial H_x^n}{\partial t}, \\
\tilde{H}_x^{n+\frac{1}{2}} &= H_x^n + \frac{\delta_t}{2} \frac{\partial \hat{H}_x^{n+\frac{1}{2}}}{\partial t}, \\
\bar{H}_x^{n+1} &= H_x^n + \delta_t \frac{\partial \tilde{H}_x^{n+\frac{1}{2}}}{\partial t}, \\
H_x^{n+1} &= H_x^n + \frac{\delta_t}{6} \left( \frac{\partial H_x^n}{\partial t} + 2 \frac{\partial \hat{H}_x^{n+\frac{1}{2}}}{\partial t} + 2 \frac{\partial \tilde{H}_x^{n+\frac{1}{2}}}{\partial t} + \frac{\partial \bar{H}_x^{n+1}}{\partial t} \right). \tag{1.42}
\end{aligned}$$

When (1.24) is implemented with the higher order RK methods, as in (1.41) and (1.42), the resulting numerical algorithm is formulated for an unstructured problem domain. This type of approach is more flexible for problems that have certain restrictions on the discretisation of the domain, because they do not have to be implemented on Cartesian meshes.

#### 1.2.4 Corrections, Smoothing and Special Boundary Conditions

In the last fifteen years, techniques from Computational Fluid Dynamics (CFD) have been adapted in Computational Electromagnetics (CEM) [7, 39, 52] with reasonable success. In this thesis, the uses of Intensity Vector Splitting (IVS) [39] and Riemann Solvers (RS) [7] are analysed when used with cell-centred spatial

discretisation methods, and mathematical formulations for these also are provided. The CFD type methods are known to dampen the electric and magnetic field components, which gives the solution to the industrial microwave problem an overall smooth appearance. The oscillatory behaviour evident in some discretisation strategies is removed by the introduction of another term into the cell face approximations. The IVS and RS techniques when used to help approximate cell face unknowns for cell-centred schemes tend to also remove instability in the discretisations.

In CEM simulations, the methods implemented from CFD that use the characteristic theory to split an electromagnetic wave into + and – states are dissipative by nature. Munz et al [31] discuss a finite-volume solver for the Maxwell's equations in curvilinear non-orthogonal coordinates without the use of dimensional splitting. The local wave propagation between adjacent grid cells is determined by the solution of Riemann problems. A thorough analysis of the characteristic methods used to determine the required solution is given in [7, 39, 52] and the reader is referred to [39] for more detailed explanation.

The characteristic theory [39] requires the flux to be split into + and – states at a cell interface (*i.e.* the cell face), then a number of different numerical approximations are applied to determine the required states. In this work, the schemes that are used to approximate the states are presented in a way that can easily be generalised to a completely unstructured mesh framework. However, in an attempt to gauge the accuracy and efficiency of the schemes investigated, it was decided to restrict the study here only to a structured mesh domain based on a Cartesian grid, since the FD-TD method [2] performs accurately on such grids and can be used for good comparisons.

Note that when these CFD type schemes are used to dampen any oscillatory

behaviour due to spatial discretisation errors caused by the cell-centred strategy, it becomes necessary to employ higher order time integration techniques to resolve the differential system in time [39]. In later chapters,  $3^{rd}$  and  $4^{th}$  order Runge-Kutta (RK3, RK4) [48, 49] methods are implemented on the cell-centred approaches to analyse their performance. However, the schemes that do not contain the damping term are discretised in time using second order Leapfrog time marching schemes that are staggered and unstaggered in time. Also, the schemes that utilise RK3 and RK4 time integrations with damping are implemented without the inclusion of the damping term, so that the effect of the term from the CFD methodology can be analysed for CEM applications.

The implementation of the electromagnetic boundary conditions have been improved over the years to better the performance of the Maxwell's equations numerical solvers on regular grids. Typically, perfectly conducting wall, incident field, material interface and absorbing layer conditions have been investigated in the past [4,9,10,53-57]. Most of these conditions have been widely used when simulating microwave heating problems, although not all of them can be migrated in a straightforward manner to an unstructured spatial methodology. In this work, an existing Perfectly Matched Layer (PML) [53] is adapted to unstructured cells, and implemented with a number of different cell-centred schemes outlined in this work. Corrections for material interface boundary conditions are investigated also [40-42], and general forms for these are provided along with the perfectly conducting wall and incident field components.

### 1.3 The Hybrid Model

The FD-TD method when applied to computing the power distribution in a lossy dielectric load can be a computationally intensive (in terms of CPU time and memory) solution scheme. Small scale industrial applications can take many

hours to obtain a numerical solution to the problem using the FD-TD method, while large scale industrial applications may take more than a week to compute on high performance computers. This research work aims to establish a scheme that can predict the heating distribution inside a lossy medium, both accurately and efficiently.

To achieve this goal, a new hybrid approach is developed, whereby the problem of determining the electromagnetic fields evolving within a waveguide and the lossy medium is decoupled into an exterior problem for computing the fields in the waveguide and the cavity, including a coarse representation of the medium, and an interior problem for a detailed resolution of the lossy medium. The exterior and interior problems are linked together at the dielectric interface so that they are coupled, and the Discrete Fourier Transform (DFT) algorithm is used to transform the time dependent electric fields to the required frequency dependent boundary conditions for the interior problem (see Figure 1.8). This newly proposed scheme is demonstrated on structured grids, so that the accuracy of the developed method can be compared to the exact solution and the FD-TD scheme.

### 1.3.1 Exterior Problem

The exterior problem requires the solution to Maxwell's equations for the electromagnetic field components inside the waveguide and cavity, as illustrated in Figure 1.8. It is well-known that time-domain solvers work very efficiently in free-space electromagnetic computations, and for this reason, the exterior problem is resolved using a time-marching algorithm. In §1.2.1 a brief outline of time discretisation strategies is provided. Furthermore, in Chapter 4 a number of different cell-centred time-marching algorithms are introduced and analysed for the solution of the exterior problem. These cell-centred schemes are all for-

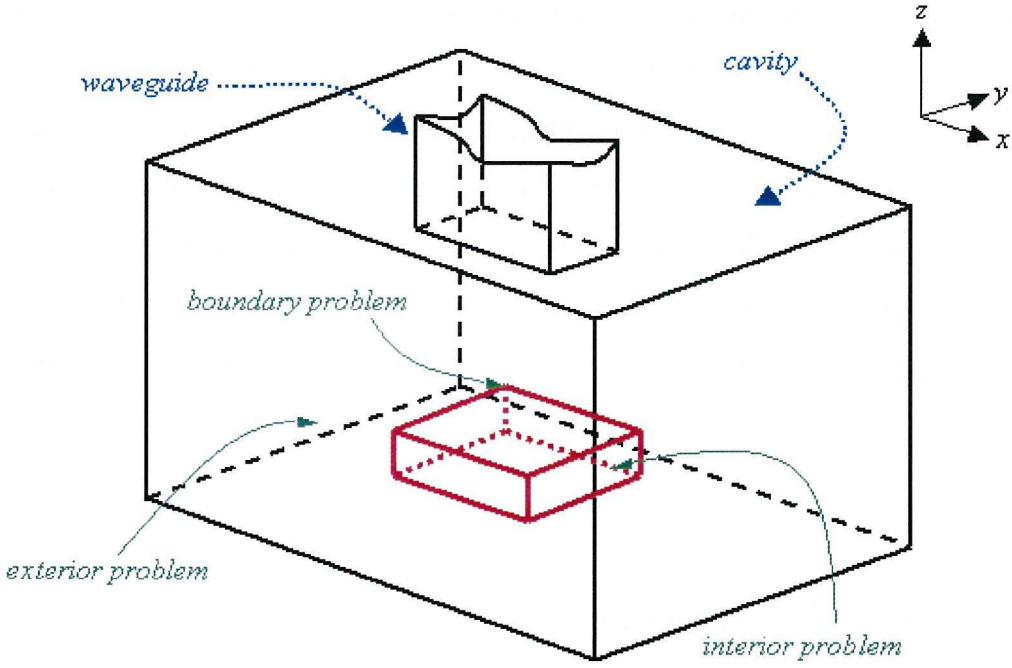


Figure 1.8: The exterior, interior and boundary problems for the Hybrid method.

mulated for unstructured meshes and it is shown that the discretisation of the time-marching algorithm is not restricted by the material and dielectric properties. Consequently, the time-marching algorithm can rapidly predict the electromagnetic fields in the free-space component of the problem.

The time-marching algorithms are all formulated for an unstructured mesh discretisation to enable the use of irregular shaped cavities and materials in the microwave heating simulation models. Technically, this allows for non-rectangular waveguides and cavities, and also caters for the heating of materials that do not necessarily resemble shapes with rectangular faces.

### 1.3.2 Boundary Problem

Once the field behaviour inside the apparatus has converged to some prescribed level of tolerance, the time-domain solution is used to predict the boundary in-

formation on the surface of the material. The electric field components on the material and free-space interface are calculated and recorded for one or two full wave periods before the interior problem is computed. From these time dependent fields on the material and free-space interface, frequency domain electric fields are generated using the Discrete Fourier Transform [48] (see Chapters 5 and 6 for full details). These frequency dependent electric field component unknowns are then used as the Dirichlet boundary condition for the interior problem.

### 1.3.3 Interior Problem

Given that the boundary information at a material interface is obtained accurately and efficiently, the Helmholtz equation can be resolved using a mesh imposed on the domain of the load alone. This technique allows for a different mesh for the material and free-space, provided that some accurate technique can be used to extrapolate the fields onto the correct material and free-space interface locations. The system of linear equations is then solved at a number of frequencies in the neighbourhood of the dominant frequency using a Krylov subspace method [51].

The proposed hybrid method combines a cell-centred time-domain solver with the Helmholtz equation implicit solution scheme, and obtains the power distribution from the electric fields that have been computed via the Helmholtz equation. This new hybrid method aims to utilise the time and frequency domain solvers to their full advantage. This process of determining the power distribution inside the load is fast, due to the fact that the time-stepping constraints of the time-domain solver are restricted by only the free-space properties.

## 1.4 Outline of Thesis

In this section an outline of the chapters of this thesis is given. The initial work considered existing methods in computational electromagnetics, whilst work performed later in the thesis is focused towards the development of the newly proposed computational algorithm that has been referred to as the hybrid method.

### 1.4.1 Chapter 2

The heating of a three-dimensional block requires knowledge of the input energy and also the heating that will take place due to the energy source. In microwave heating applications, the energy is delivered in the form of high frequency electromagnetic waves that are constricted by a cavity structure. The first paper of this thesis analyses the heating process and investigates thermal runaway for ceramic type materials inside a waveguide [58], which ties in with the objective to study the effects of thermal runaway, and how this phenomenon impacts upon the heating of certain types of materials. The paper associated with this Chapter makes most of its contribution towards the industrial microwave heating literature.

Chapter 2 outlines three different approaches to resolve the electromagnetic scattering within a certain waveguide loaded with a ceramic block. The first approach is a frequency-domain solution strategy, whilst the second approach uses the classical FD-TD method with some improvements for material interface wave propagation. A new semi-analytical algorithm is implemented also, and the performance of the three different schemes are compared. Once the electric field behaviour inside the apparatus has been determined, the forced heat equation is computed to obtain the heat distribution within the ceramic block. The input power of the magnetron is varied to monitor how this impacts upon the heating inside the ceramic, and hence, results of input power versus maximum heat inside

the ceramic block are produced to elucidate the thermal runaway for this process.

The primary finding of this work was to show that the semi-analytical method can adequately capture the nature of the heating within the ceramic block when compared to the frequency and time-domain strategies, and at the same time, offer significant savings in numerical computation times. It was shown also that for a small increase in input power a large increase in absorbed heat may be observed for ceramic type materials that have absorptivity that is temperature dependent and governed by an Arrhenius-type law.

#### 1.4.2 Chapter 3

The work in this chapter is related to the propagation of a Gaussian pulse at the microwave frequency within a constrained apparatus. The pulse was propagated inside a standard rectangular waveguide to show the dissipative and dispersive nature of the error for the different types of spatial and temporal discretisation strategies implemented in this paper [59].

The primary objective of the work related to this chapter is to demonstrate the nature of the errors within cell-centred spatial electromagnetic numerical schemes. To do this, staggered and unstaggered Leapfrog time integration methods were implemented and compared to third and fourth order Runge-Kutta ordinary differential equations solvers when resolving the time derivatives. All of the cell-centred schemes presented in this paper were benchmarked against the finite-difference time-domain methodology.

To obtain the finite-volume representation for the electromagnetic field equations, the Maxwell's equations were represented in a surface-volume form, and a number of different approaches were implemented to predict the electric and

magnetic field unknowns at the cell faces. Finally, a comparison of the classical finite-difference time-domain method and the different finite-volume time-domain numerical results for a standard case study in rectangular waveguides allowed the accuracy of the developed methods to be assessed.

The work illustrates that time-domain cell-centred Maxwell's equations solvers can be used to predict electromagnetic fields in free-space. It was observed that staggered Leapfrog and the Runge-Kutta methods produced results that were comparable to the classical finite-difference time-domain scheme.

### 1.4.3 Chapter 4

In Chapter 3, the free-space propagation of the electromagnetic fields was investigated. In this chapter, the previous work on the free-space Gaussian pulse propagation was adapted to a loaded waveguide to analyse the different errors of the schemes when material interactions are present. Moreover, the paper that comprises this chapter analyses techniques for implementing a cell-centred finite-volume time-domain computational methodology for the purpose of microwave heating [60].

To predict the heat dissipated within a certain object inside the apparatus, the power distribution has to be computed before an estimate of the dissipated heat can be calculated. To achieve this, time-averaged electric fields are obtained to predict the power distribution. As a consequence, only dissipative and dispersive errors tend to affect the final heat distribution, because the wave front speed and phase errors do not significantly alter the time-averaged electric fields. Therefore, the work was focused towards analysing the errors that can change the nature of the time-averaged fields, which are needed for microwave heating processes.

New cell-centred absorbing boundary conditions were formulated for the different cell-centred finite-volume time-domain strategies. Boundary conditions for the incident field and conducting walls were also investigated, and general equations for these are derived. The effect of computational fluid dynamics type algorithms was considered, and Riemann solvers and Intensity vector splitting approaches were implemented along with other spatial discretisation schemes. At material interfaces the methods from computational fluid dynamics aim to better capture the nature of the fields, and for comparison, plane wave assumptions were used in schemes that do not utilise Riemann solvers or Intensity vector splitting to show that these schemes are adequate for microwave power distribution calculations. All of the cell-centred finite-volume time-domain strategies investigated were compared to the finite-difference time-domain method with plane wave assumption at a material interface to correct the electromagnetic wave propagation defraction and reflection.

This work highlighted that for microwave heating purposes some cell-centred finite-volume time-domain solvers can be used to capture the nature of the electromagnetic wave propagation within a waveguide loaded with a dielectric material. It was shown also that certain numerical schemes are unstable and should not be used for simulating industrial microwave heating, while others have errors that are too large to accurately predict the power distribution, and hence, the dissipated heat within the material.

#### 1.4.4 Chapter 5

In this work, a novel hybrid approach is presented that uses a combination of both time-domain and frequency-domain solution strategies to predict the power distribution within a lossy medium loaded within a waveguide [61]. The work from

Chapter 4 on cell-centred finite-volume time-domain solvers allowed the choice of a suitable cell-centred solver to compute the electric and magnetic fields inside the free-space component of the waveguide. Within the material, a frequency-domain approach is used to solve the Helmholtz equation for the electric field, and subsequently, the power distribution.

The material boundary condition for the Helmholtz equation numerical solver was calculated by converting time-domain data computed using the cell-centered finite-volume time-domain strategy to the frequency-domain using the discrete Fourier transform. The generalised minimal residual Krylov subspace iterative method GMRES was used to resolve the discrete frequency-domain Helmholtz equation with Dirichlet boundary conditions.

It was shown that the hybrid solution methodology performs well when a single frequency is considered in the evaluation of the Helmholtz equation in a single mode waveguide. It is evident from this work that the hybrid methodology can predict with high accuracy the power distribution inside the material within the waveguide.

#### 1.4.5 Chapter 6

The main contribution of the thesis is presented in this chapter. The proposed hybrid method is tested thoroughly for different dielectric media loaded in either a waveguide configuration, or a multi-mode cavity [62]. A number of different case studies are presented and the hybrid method is validated using previously published thermal image data.

In this case, as opposed to Chapter 5, a multi-mode cavity is considered with all field components active. A full three-dimensional numerical strategy was em-

ployed to resolve the electromagnetic fields within both the waveguide and cavity. Due to the nature of the propagating fields inside the cavity, the waveguide feeding the cavity was adjusted to accommodate another absorbing boundary condition, ensuring that the true  $TE_{10}$  mode was retained in the waveguide. Numerical experimentation has shown that this additional absorbing boundary condition is necessary, otherwise the physics of the problem would be altered.

With multi-mode cavity calculations, the problem size tends to be much larger than for waveguide configurations. Therefore, it is essential that efficient numerical schemes are employed in the determination of the power distribution. The hybrid method has been shown to produce accurate results and also performs very efficiently when compared to existing algorithms, particularly the finite-difference time-domain method. It is evident from this work that it is not necessary to compute for as many periods inside the free-space component of the problem, as has been done in the past for time-domain numerical solution strategies.

#### **1.4.6 Chapter 7**

The final chapter states the findings of thesis and links the findings to the aims and objectives outlined in this chapter. A detailed discussion regarding the outcomes of the different papers is provided also, including recommendations for future research directions.

# Bibliography

- [1] Metaxas, A.C. and Meredith, R.J., *Industrial Microwave Heating*. Peter Peregrinus Ltd. London, UK, 1983.
- [2] Yee, K.S. *Numerical Solution of Initial Boundary Value Problem Involving Maxwell's Equations in Isotropic Media*. IEEE Trans. Antennas Propagat., 1966, **14**: p. 302-307.
- [3] Bosisio, R. G., Nachman, M., et al. *A Simple Method for Determining the Electric Field Distribution Along a Microwave Applicator*. J. Microwave Power and Electromagnetic Energy, 1975, **10.2**: p. 224-231.
- [4] Mur, G., *Absorbing Boundary Conditions for the Finite-Difference Approximation of the Time-Domain Electromagnetic-Field Equations*. IEEE Trans. Microwave Theory Tech., EMC-23, 1981, **4**: p. 377-382.
- [5] De Pourcq, M. and Eng, C., *Field and power-density calculations in closed microwave systems by three-dimensional finite differences*. IEEE Proceedings, 1985, **132**: p. 360-368.
- [6] Madsen, N.K. and Ziolkowski, R.W., *Numerical solution of Maxwell's' equations in the time domain using irregular nonorthogonal grids*. Wave Motion, 1988, **10**: p. 583-596.

- [7] Shankar, V. and Mohammadian, A.H., *A Time-Domain, Finite-Volume Treatment for the Maxwell Equations.*, 1990, J. Microwave Power and Electromagnetic Energy, p. 128-145.
- [8] Jia, X., Jolly, P., *Simulation of Microwave Field and Power Distribution in a Cavity by a Three-Dimensional Finite Element Method*. Journal of Microwave Power, 1992, 27(1): p. 11-22.
- [9] Berenger, J. P. *A Perfectly Matched Layer for the Absorption of Electromagnetic Waves*. Journal of Computational Physics, 1993, 114: p. 185-200.
- [10] Berenger, J.P., *Three-Dimensional Perfectly Matched Layer for the Absorption of Electromagnetic Waves*. Journal of Computational Physics, 1996, 127: p. 363-379.
- [11] Fu, W. and Metaxas, A., *Numerical Prediction of Three-Dimensional Power Density Distributions in a Multi-Mode Cavity*. J. Microwave Power and Electromagnetic Energy, 1994, 29(2): p. 67-75.
- [12] Dibben, D.C. and Metaxas, A.C., *Time Domain Finite Element Analysis of Multimode Microwave Applicators Loaded with Low and High Loss Materials*. Intl. Conf. Microwave and High Energy Heating, 1995, 1-3.4.
- [13] Zhao, H., *Computational Models and Numerical Techniques for Solving Maxwell's Equations: A Study of Heating of Lossy Dielectric Materials Inside Arbitrary Shaped Cavities*. Centre in Statistical Science and Industrial Mathematics, Queensland University of Technology, 1997.
- [14] Reader, H.C. and Chow Ting Chan, T.V., *Experimental and Numerical Field Studies in Loaded Multimode and Single Mode Cavities*. J. Microwave Power and Electromagnetic Energy, 1998, 33(2): p.103-112.

- [15] Ditkowski, A., Dridi, K. and Hesthaven, J.S., *Convergent Cartesian Grid Methods for Maxwell's Equations in Complex Geometries*. Journal of Computational Physics, 170(1): p.39-80, 2001.
- [16] Xie, Z., Chan, C. and Zhang, B., *An Explicit Fourth-Order Orthogonal Curvilinear Staggered-Grid FDTD Method for Maxwell's Equations*. Journal of Computational Physics, 175(2): p. 739-763, 2002.
- [17] Kraus, J. D. and Fleisch, D.A., *Electromagnetics with Applications*. McGraw-Hill, 1999.
- [18] Collin, R.E., *Field Theory of Guided Waves*. McGraw-Hill Book Company, 1960.
- [19] Dibben, D.C., *Numerical and Experimental Modelling of Microwave Applicators*. Department of Engineering, University of Cambridge, 1995, 188.
- [20] Perr, P. and Turner, I.W., *Microwave Drying of Softwood in an Oversized Waveguide: Theory and Experiment*. 2579-2600 AICHE J., 1997, 43(10).
- [21] Zhao, H. and Turner, H., *An analysis of the finite-difference time-domain method for modelling the microwave heating of dielectric materials within a three-dimensional cavity system*. Journal of Microwave Power and Electromagnetic Energy, 1996, 31(4): p. 199-214.
- [22] Madsen, N.K. and Ziolkowski, R.W., *A three-dimensional modified finite volume technique for Maxwell's equations*. Electromagnetics, 1990, (10): p. 147-161.
- [23] Harms, P.H., Chen, Y., Mittra, R. and Shimony, Y., *Numerical Modeling of Microwave Heating Systems*. J. Microwave Power and Electromagnetic Energy, 1996, 31(2): p. 114-121.

- [24] Malan, D.H. and Metaxas, A.C., *Domain Decomposition and Parallel Processing in Microwave Applicator Design*. Eleventh International Conference on Domain Decomposition Methods, 1999, p. 539-542.
- [25] Kenkre, V.M., Skala, L., Weiser, M.W. and Katz, J.D., *Theory of microwave effects on atomic diffusion in sintering: basic considerations of the phenomenon of thermal runaway*. Microwave processing of materials II (ed. W.B. Snyder, W.H. Sutton, M.F. Iskander & D.L. Johnson), Material Research Society Symposium Proceedings, 1991, **189**: p. 179-183, Material Research Society.
- [26] Kriegsmann, G.A., *Cavity effects in microwave heating of ceramics*. SIAM J. Appl. Math, 1997, **57**: p. 382-400.
- [27] Liu, B. and Marchant, T.R., *The microwave heating of three-dimensional blocks: semi-analytical solutions*. IMA J. Appl. Maths, 2002, **67**: p. 145-175.
- [28] Taflove, A., *Re-inventing Electromagnetics: Supercomputing Solution of Maxwell's Equations Via Direct Time Integration on Space Grids*. AIAA paper 92-0333, 1992, (New York).
- [29] Dean, E.J. and Glowinski, R., *Domain Decompositions of Wave Problems Using Mixed Finite Element Method*. Ninth International Conference on Domain Decomposition Methods, 1998, p. 326-333.
- [30] Brezzi, F., Franca, L.P., Marini, D. and Russo, A., *Stabilization Techniques for Domain Decomposition Methods with Non-Matching Grids*. Ninth International Conference on Domain Decomposition Methods, 1998, p. 1-10.
- [31] Munz, C.D., Schneider, R. and Voß, U., *A finite-volume method for the maxwell equations in the time-domain*. SIAM Journal of Statistical Computing, 2000, **22(2)**: p. 449-475.

- [32] Palaniswamy, S., Hall, W.F. and Shankar, V., *Numerical Solution to Maxwell's Equations in the Time Domain on Nonuniform Grids*. Radio Science, 1996, 31(4): p.905-912.
- [33] Gedney, S.D., Lansing, F.S. and Rascoe, D.L., *Full Wave Analysis of Microwave Monolithic Circuit Devices Using Generalized Yee-Algorithm Based on an Unstructured Grid*. Transactions on Microwave Theory and Techniques, 1996, 44(8): p. 1393-1400.
- [34] Assous, F., Ciarlet Jr., P. and Segre, J., *Numerical Solution to the Time-Dependent Maxwell Equations in Two-Dimensional Singular Domains: The Singular Complement Method*. J. Computational Physics, 2000, **161**: p. 218-249.
- [35] Driscoll, T.A. and Fornberg, B., *Note on Nonsymmetric Finite Differences for Maxwell's Equations*. J. Computational Physics, 2000, **161**: p. 723-727.
- [36] Hile, C.V. and Kriegsmann, G.A., *A hybrid numerical method for loaded highly resonant single mode cavities*. J. Comput. Phys, 1998, **142**: p. 506-520.
- [37] Toselli, A., *Overlapping Methods with Perfectly Matched Layers for the Solution of the Helmholtz Equation*. Eleventh International Conference on Domain Decomposition Methods, 1999, p. 552-557
- [38] Saad, Y., *Iterative Methods for Sparse Linear Systems*. Second Edition with Corrections, <http://www-users.cs.umn.edu/~saad/>, 2000.
- [39] Liu, Y., *Fourier Analysis of Numerical Algorithms for the Maxwell Equations*. Journal of Computational Physics, 1996, **124**: p. 396-416.
- [40] Munz, C.D., Omnes, P., Schneider, R., Sonnendrucker, E. and Voß, U., *Divergence Correction Techniques for Maxwell Solvers Based on a Hyperbolic Model*. J. Computational Physics, 1999, **161**: p. 484-511.

- [41] Assous, F., Degond, P. and Segre, J., *Numerical Approximation of the Maxwell Equations in Inhomogeneous Media by a  $P^1$  Conforming Finite Element Method*. J. Computational Physics, 1996, **128**: p. 363-380.
- [42] Jiang, B., Wu, J. and Povinelli, L.A., *The Origin of Spurious Solutions in Computational Electromagnetics*. Journal of Computational Physics, 1996, **125**: p. 104-123.
- [43] Zhu, S.Z. and Chen, H.K., *Power Distribution Analysis in Rectangular Microwave Heating Applicator with Stratified Load*. J. Microwave Power and Electromagnetic Energy, 1988, **23.3**: p. 139-143.
- [44] Hyman, J.M. and Shashkov, M., *Mimetic Discretizations for Maxwell's Equations*. Journal of Computational Physics, 1999, **151**: p. 881-909.
- [45] Shang, J.S., *High-Order Compact-Difference Schemes for Time-Dependent Maxwell Equations*. Journal of Computational Physics, 1999, **153**: p. 312-333.
- [46] Barth, T.J., *Aspects of Unstructured Grids and Finite-Volume Solvers for the Euler and Navier-Stokes Equations*. Lecture Notes Presented at the VKI Lecture Series, 1994-05, 1995.
- [47] Liu, Y. and Vinokur, M., *Exact Integrations of Polynomials and Symmetric Quadrature Formulas over Arbitrary Polyhedral Grids*. J. Computational Physics, 1998, **140**: p. 122-147.
- [48] Press, W.H., Teukolsky, S.A., et al., *Numerical Recipes in C: The Art of Scientific Computing*. Cambridge Press, 1997.
- [49] Burden, R. L. and Faires, J.D., *Numerical Analysis*. Brooks/Cole Publishing Company, 1997.

- [50] Ahuja, V. and Long, L.N., *A Parallel Finite-Volume Runge-Kutta Algorithm for Electromagnetic Scattering*. J. Computational Physics, 1997, **137**: p. 299-320.
- [51] Saad, Y., M.H.S., *GMRES: a generalized minimum residual algorithm for solving nonsymmetric linear systems*. SIAM Journal of Scientific and Statistical Computing, 1986, **7**: p. 856-869.
- [52] Mohammadian, A.H., Shankar, V. and Hall, W.F., *Computation of electromagnetic scattering and radiation using a time-domain finite-volume discretization procedure*. Comp. Phys. Comm., 1991, **68**: p. 175-196.
- [53] Petropoulos, P.G., Zhao, L., et al., *A Reflectionless Sponge Layer Absorbing Boundary Condition for the Solution of Maxwell's Equations with High-Order Staggered Finite Difference Schemes*. Journal of Computational Physics, 1998, **139**: p. 184-208.
- [54] Abarbanel, S. and Gottlieb, D., *A Mathematical Analysis of the PML Method*. J. Computational Physics, 1997, **134**: p. 357-363.
- [55] Yang, B. and Petropoulos, P.G., *Plane-Wave Analysis and Comparison of Split-Field, Biaxial, and Uniaxial PML methods as ABCs for Pseudospectral Electromagnetic Wave Simulations in Curvilinear Coordinates*. J. Computational Physics, 1998, **146**: p. 747-774.
- [56] Yang, B., Gottlieb, D. and Hesthaven, J.S., *Spectral Simulations of Electromagnetic Wave Scattering*. J. Computational Physics, 1997, **134**: p. 216-230.
- [57] Petropoulos, P.G., *NOTE on the Termination of the Perfectly Matched Layer with Local Absorbing Boundary Conditions*. J. Computational Physics, 1998, **143**: p.665-673.
- [58] Liu, B., Marchant, T.R., Turner, I.W., Vegh, V., *A Comparison of Three-dimensional Semi-analytical and Numerical Techniques for the Microwave*

*Heating of a Lossy Material in a Waveguide.* 3rd World Congress on Microwave and Radio Frequency Applications, September 2002.

- [59] Vegh, V., Turner, I.W., *Comparison of Time-Domain Numerical Solvers for the Propagation of a Gaussian Pulse Inside a Rectangular Waveguide*. Australian & New Zealand Industrial and Applied Mathematics Journal - Electronic Supplement, **44**, 2002–2003.
- [60] Vegh, V., Turner, I.W., Zhao, H., *Comparison of Time-Domain Solvers for the Solution of Maxwell's Equations*. Submitted in the International Journal of Applied Mathematical Modelling, 2001.
- [61] Vegh, V., Turner, I.W., *A Hybrid Approach for Resolving the Microwave Heating inside Lossy Media*. Advances in Microwave and Radio Frequency Processing, Ampere 8, Germany, 2002.
- [62] Vegh, V., Turner, I.W. *A Hybrid Technique for Computing the Power Distribution Generated in a Lossy Medium During Microwave Heating*. Submitted for publication in International Journal of Computational and Applied Mathematics, 2003.

# Chapter 2

## A Comparison of Semi-analytical and Numerical Solutions for the Microwave Heating of a Lossy Material in a Three-dimensional Waveguide

### Statement of Joint Authorship

**Liu, B.** Implemented the semi-analytic solution strategy, computed the power inside the medium, solved the heat equation to obtain the maximum temperature in the block, interpreted the results, wrote the semi-analytic part of the manuscript, proof read manuscript.

**Marchant, T. R.** Guided the research work, helped with the implementation and computation of the semi-analytic solution strategy, interpreted results, wrote the majority of manuscript, proof read the manuscript.

**Turner, I. W.** Suggested ways of improving the different numerical time domain solvers, directed and guided the work, assisted with interpretation of results and the preparation of the paper, proof read the manuscript.

**Vegh, V.** (Candidate) Numerically modelled the FD-TD method and the forced heat equation,

computed maximum power in the block, generated results, interpreted these results, wrote the time-domain solver section of the manuscript, proof read the manuscript.

NOMENCLATURE	
<b>A</b>	Coefficient matrix
<b>B</b>	Magnetic flux density ( $T$ )
<b>E</b>	Electric field intensity ( $V$ )
<b>H</b>	Magnetic field intensity ( $A/m$ )
<b>J</b>	Electric current density ( $A/m^2$ )
<i>c</i>	Speed of radiation ( $m/s$ )
<i>e</i>	Tolerance
<i>k</i>	Wave number in free-space
<i>l</i>	Block dimension ( $m$ )
<i>m</i>	Constant
<i>p</i>	Constant
<i>P</i>	Power ( $W$ )
$P_{av\_in}$	Average input power ( $W/m^2$ )
<i>t</i>	Time ( $s$ )
$T_a$	Ambient temperature ( $K$ )
<i>U</i>	Non-dimensional electric field
<i>V</i>	Non-dimensional magnetic field
$\beta$	Normalised power
$\delta_t$	Time step of numerical scheme ( $s$ )
$\epsilon$	Permittivity ( $F/m$ )
$\mu$	Permeability ( $H/m$ )
$\omega$	Angular frequency ( $2\pi f$ ) ( $rad/s$ )
$\rho$	Volume charge density ( $C/m^3$ )
<b>b</b>	Right hand vector
<b>D</b>	Electric flux density ( $V/m$ )
<b>E<sub>f</sub></b>	Electric field at material face ( $V$ )
<b>H<sub>f</sub></b>	Magnetic field at material face ( $A/m$ )
<i>a</i>	Broad dimension of waveguide ( $m$ )
<i>C</i>	Specific heat capacity ( $J/kg K$ )
$E_0$	Incident electric field ( $V$ )
$k_1$	Wave number
<i>l</i>	Krylov sub-space dimension
<i>n</i>	Constant
<i>q</i>	Constant
$P_{abs}$	Absorbed power ( $W/m^3$ )
<i>t</i>	Positive integer
<i>T</i>	Temperature ( $K$ )
$T_{max}$	Maximum temperature ( $K$ )
$U_{inc}$	Incident electric field
$\alpha$	Constant
$\delta$	Loss angle ( $rad$ )
$\delta_z$	Increment in the $z$ direction ( $m$ )
$\lambda_T$	Wave period
$\nu$	Thermal conductivity ( $W/m K$ )
$\rho$	Density of the material ( $kg/m^3$ )
$\sigma$	Electric conductivity ( $\Omega^{-1}/m$ )

Table 2.1: List of symbols used in Chapter 2.

## Abstract

The microwave heating of a three-dimensional block in an infinitely long rectangular waveguide propagating the  $TE_{10}$  mode is considered. The electrical conductivity (the dielectric loss) is assumed to be a function of temperature, and modelled by the Arrhenius law. A coupled set of equations is obtained that describes the electromagnetic fields and the temperature distribution in the block.

The numerical solutions of this problem are obtained by two methods, the well known FD-TD scheme and a frequency domain method which makes the

further assumption that a single  $TE_{10}$  mode exists in the waveguide and material. The results show that an S-shaped temperature versus power response curve is possible, with thermal runaway occurring when the solution jumps from the lower (cool) branch to the upper (hot) branch of this curve. The results confirm the validity of the single-mode assumption and show a good comparison between the numerical and semi-analytical solutions.

## 2.1 Introduction

Industrial microwave heating has a history dating back to the 1940s (see [5]), and there are many heating, drying and thawing applications in industry. One key benefit of microwave heating is its speed of processing compared to conventional convective heating, which arises primarily due to the volumetric heating phenomenon associated with microwave processing. This phenomenon, which sees the bulk of the energy delivered directly to the core of the sample, can be used to eliminate the case-hardening of products that are heated and dried by classical convective methods. Other advantages of microwave heating are the more compact heating systems offered by the technology, the superior final product quality, and cleaner heating and drying environments.

In general, controlled uniform heating is difficult to achieve with microwave processing, because rapid overheating (thermal runaway) can occur in some materials for a small increase in incident power. The phenomenon of thermal runaway is analogous to the combustion of an exothermic chemical reactant. The rate at which a chemical reaction proceeds increases with temperature, hence if the reaction is exothermic then the heat generated will result in positive feedback that can cause an explosion. The rate at which microwave radiation is absorbed by a material is also temperature-dependent. Hence, thermal runaway in this context is the result of an analogous feedback process.

A study of microwave heating involves solving both Maxwell's equations and the forced heat equation. Maxwell's equations describes the propagation of the microwave radiation in the material and the microwave waveguide or cavity, while the forced heat equation describes the heat absorption and diffusion in the block. Due to the temperature-dependent material properties, the governing equations are nonlinearly coupled and unable to be solved analytically. Numerical and semi-analytical solution methods have been used with success however, and are briefly reviewed below.

[4] considered the steady-state microwave heating of a three-dimensional block by the transverse magnetic waveguide mode  $TM_{11}$ , in a long rectangular waveguide. The electrical conductivity and the thermal absorptivity were assumed to be temperature dependent while both the electrical permittivity and magnetic permeability were assumed constant. Both a quadratic relation and an Arrhenius-type law were used for the temperature-dependency. Semi-analytical solutions, valid for small thermal absorptivity, were found for the steady-state temperature and the electric-field amplitude using the Galerkin method. At the steady-state, the temperature versus power relationship was found to be multivalued; at the critical power level, thermal runaway occurs when the temperature jumps from the lower (cool) temperature branch to the upper (hot) temperature branch of the solution. Examples were presented in the limits of small and large heat-loss with an excellent comparison with numerical solutions obtained.

[3] considered the small Biot-number heating of a ceramic slab in a  $TE_{103}$  waveguide applicator including an iris with a variable aperture. By considering the small Biot-number limit, which allows the heat equation to be averaged, an expression is obtained relating the temperature and incident power. This relation was shown to be bistable, or S-shaped. The microwave cavity can be tuned by

varying the aperture width because this changes the S-shaped response curve. Hence, there exists an optimal aperture width that sinters the ceramic with minimum power. Moreover, varying the aperture width (and hence the S-shaped curve) allows the sintering temperature on the upper branch to be reached without feedback control.

The finite-difference time-domain (FD-TD) method is commonly used to solve Maxwell's equations numerically (see [1, 6, 7, 8]). [6] applied the FD-TD method to the microwave heating of a lossy material in a three-dimensional cavity, where a rectangular waveguide propagating the  $TE_{10}$  mode excites a cavity. It was shown that the assumption of the existence of a single  $TE_{10}$  mode within the waveguide provided a computed electric-field that did not satisfy the divergence condition. The authors developed a full-mode numerical model that included improved numerical implementations of the appropriate boundary conditions at corners and at dielectric interfaces to improve the accuracy of the FD-TD field approximations. The numerical solutions corresponded closely to experimental results from case studies involving the heating of plastic blocks and food on a tray.

[1] considered a hybrid analytical and numerical method for the heating of a ceramic material in a single mode cavity containing an iris. For low-loss ceramics loaded within high-Q cavities, the usual FD-TD numerical scheme was shown to be inefficient. To overcome this inefficiency the authors split the problem by solving numerically with no iris, and then by analytically matching the numerical solution to theoretical results obtained for the electromagnetic field near the iris. The full solution is then obtained in a computationally efficient manner, with some six fold computation time improvements over the FD-TD numerical scheme alone.

The aim of this paper is to compare semi-analytical and numerical solutions

for the heating of a three-dimensional dielectric block in a rectangular waveguide by the  $TE_{10}$  mode. Numerical solutions will be obtained by time-domain (using the usual FD-TD scheme) and frequency domain methods. A key assumption of the frequency domain method is that of a single waveguide mode, the validity of which will be examined. The FD-TD method for solving Maxwell's equations in three-dimensions typically require excessive amounts of computer resources, so comparison of the CPU usage of each scheme will also be made. As the geometry of the problem is regular, semi-analytical solutions developed using the method of [4] are also presented, and shown to be reasonably accurate. It is envisaged that the techniques developed here will be useful for the development of efficient hybrid analytical and numerical schemes for the heating of blocks in arbitrarily shaped microwave cavities and thus forms the foundations of future research to be conducted by the authors.

In §2.2 the governing equations are presented, while §2.3 contains brief details of the numerical schemes. A comparison of the numerical and semi-analytical solutions is presented in §2.4. The results highlight the good agreement between the numerical and semi-analytical solutions for the computed steady-state power versus temperature S-shaped curves.

## 2.2 Governing equations

Maxwell's equations of electromagnetism are given by

$$\begin{aligned}\nabla \cdot \mathbf{D} &= \nabla \cdot (\epsilon \mathbf{E}) = \rho, & \nabla \cdot \mathbf{B} &= \nabla \cdot (\mu \mathbf{H}) = 0, \\ \nabla \times \mathbf{E} &= -\frac{\partial}{\partial t}(\mu \mathbf{H}), & \nabla \times \mathbf{H} &= \frac{\partial}{\partial t}(\epsilon \mathbf{E}) + \sigma \mathbf{E},\end{aligned}\tag{2.1}$$

based on the assumption that the material is homogeneous, isotropic and ohmic, so that the current  $\mathbf{J}$  and the displacement current  $\mathbf{D}$  are both proportional to the electric field  $\mathbf{E}$  and the magnetic field strength  $\mathbf{H}$  is proportional

to the magnetic flux density  $\mathbf{B}$ . Here  $\sigma$  is the electrical conductivity,  $\epsilon$  is the electrical permittivity and  $\mu$  is the magnetic permeability. In general all material properties are temperature dependent.

Maxwell's equations are coupled with the forced heat equation

$$\rho C T_t = \nu \nabla^2 T + \frac{1}{2} \omega \epsilon \tan \delta \mathbf{E} \cdot \bar{\mathbf{E}}, \quad (2.2)$$

where  $\nu$  is the thermal conductivity,  $\rho$  is the density,  $C$  is the specific heat of the material,  $\omega$  is the frequency of the radiation and  $\tan \delta$  is the loss tangent.

Typically the loss tangent is temperature dependent; power-law and exponential temperature dependencies have been widely used in modelling microwave heating phenomena. Arrhenius-type temperature dependencies, which are bounded at large temperatures, have also been used. This law is motivated from statistical mechanics and models the physical saturation of the conductivity at high temperatures. See [2] for a discussion of the physics of an Arrhenius-type absorption law and its application to the sintering of ceramics. In this paper, an Arrhenius-type temperature dependency, of the following form is used,

$$\tan \delta = \frac{\sigma}{\omega \epsilon} = \alpha(1 + 20e^{-\frac{T_a}{(T-T_a)}}), \quad (2.3)$$

where  $T_a$  is the ambient temperature and  $\alpha$  is a constant. Equation (2.3) is equal to unity at the ambient temperature of  $T_a$ , while as the temperature becomes large, (2.3) is bounded ( $\tan \delta \rightarrow 21$ ).

The boundary conditions for the electric-field at the interfaces with free space are

$$(\mathbf{E} - \mathbf{E}_f) \times \mathbf{n} = 0, \quad (\mathbf{H} - \mathbf{H}_f) \times \mathbf{n} = 0, \quad (\epsilon \mathbf{E} - \epsilon_0 \mathbf{E}_f) \cdot \mathbf{n} = 0, \quad (2.4)$$

where  $\mathbf{E}_f$  and  $\mathbf{H}_f$  are the electric and magnetic fields in the free space incident upon the material. On the surface of the waveguide  $\mathbf{E} \times \mathbf{n} = 0$ , as there is no electric-field in a conductor. For simplicity, this work assumes a fixed temperature boundary condition,  $T = T_a$ , is applied on each of the slab's surfaces.

### 2.2.1 The frequency domain

In their most general form the electric and magnetic fields can be written as follows:

$$\mathbf{E} = E_j \mathbf{e}_j = U_j(x, y, z) e^{-i\omega t} \mathbf{e}_j, \mathbf{H} = H_j \mathbf{e}_j = V_j(x, y, z) e^{-i\omega t} \mathbf{e}_j, j = 1, 2, 3, \quad (2.5)$$

where  $\mathbf{e}_1$ ,  $\mathbf{e}_2$  and  $\mathbf{e}_3$  are unit vectors in the x, y and z directions respectively. The electric and magnetic fields are written as steady-state amplitudes modulated by the frequency. As the time scale for electromagnetic propagation is much smaller than the time scale for thermal diffusion the time derivatives of the electric and magnetic field amplitudes,  $U_j$  and  $V_j$ , and of the electrical conductivity,  $\sigma$ , can be ignored. Substituting (2.5) into (2.1) gives

$$\nabla^2 U_j - \frac{\partial}{\partial x_j} \nabla \cdot \mathbf{U} + k_1^2 (1 + i\frac{\sigma}{\omega\epsilon}) U_j = 0, \quad j = 1, 2, 3, \quad (2.6)$$

as the governing equation for the steady-state components of the electric-field amplitude, where the wavenumber  $k_1 = \omega/c$  and c is the velocity of the radiation in the block.

A single-mode assumption, that the electric field in the block maintains the form of the  $TE_{10}$  mode, is made so that  $U_1 = U_3 = H_2 = 0$ , and there is only one electric-field amplitude component,  $U_2 = U_2(x, z)$ . The governing equation (2.6) then becomes

$$U_{2xx} + U_{2zz} + k_1^2(1 + i\frac{\sigma}{\omega\epsilon})U_2 = 0. \quad (2.7)$$

The steady-state amplitude equation (2.7) and the forced heat equation (2.2) are non-dimensionalised by the scalings

$$t' = \frac{t\nu}{\rho Cl^2}, \quad x' = \frac{x}{l}, \quad y' = \frac{y}{l}, \quad z' = \frac{z}{l}, \quad U'_j = \frac{U_j}{U_{inc}}, \quad T' = \frac{T}{T_a} - 1, \quad (2.8)$$

where  $2l$  is the length of the block,  $U_{inc}$  is the incident amplitude of one of the components of the electric-field,  $\nu$  is the thermal conductivity and  $T_a$  is the ambient temperature. The non-dimensionalisation results in the scaled frequency, power, electrical conductivity and wavenumbers having the forms

$$\omega' = \frac{\omega l^2 \rho C}{\nu}, \quad \beta' = \frac{l^2 \rho C U_{inc}^2 \omega \epsilon}{2\nu T_a}, \quad \sigma' = \frac{\sigma}{\omega \epsilon}, \quad k'_1 = k_1 l. \quad (2.9)$$

A finite three-dimensional block of non-dimensional length 2, width  $2n$  and height  $2m$  is considered. It is assumed that the waveguide has width  $2n$  and height  $2m$  so that the block completely fills the cross-section of the waveguide, which is infinitely long. The waveguide is aligned to ensure that the waveguide mode propagates in the z-direction. Here, the fundamental transverse electric waveguide ( $TE_{10}$ ) mode is considered. The  $TE_{10}$  waveguide mode, which is the usual choice for single-mode commercial waveguides, is

$$E_2 = \cos(\frac{\pi x}{2n})e^{i\theta}, \quad H_1 = -\frac{k_r}{\mu\omega} \cos(\frac{\pi x}{2n})e^{i\theta}, \quad H_3 = -\frac{i\pi}{2\mu\omega n} \sin(\frac{\pi x}{2n})e^{i\theta}, \quad (2.10)$$

where  $\theta = k_r z - \omega t$ ,  $k_r^2 = k^2 - \frac{\pi^2}{4n^2}$ , and  $k$  is the wave number in free space. Note that for the microwaves to propagate in the waveguide  $k > \frac{\pi}{2n}$ , which is the cut-off wavenumber.

In nondimensional form the equations are

$$U_{2xx} + U_{2zz} + k_1^2(1 + i \tan \delta)U_2 = 0, \quad (2.11)$$

$$T_t = T_{xx} + T_{yy} + T_{zz} + \beta \tan \delta |U_2|^2 = 0, \quad (2.12)$$

For the  $TE_{10}$  mode the boundary conditions, from (2.4), are

$$U_{2z} + ik_r U_2 = 2ik_r \cos\left(\frac{\pi x}{2n}\right), \quad z = -1, \quad (2.13)$$

$$U_{2z} - ik_r U_2 = 0, \quad z = 1, \quad (2.14)$$

$$U_2 = 0, \quad x = \pm n, \quad (2.15)$$

$$T = 0, \quad x = \pm n, \quad y = \pm m, \quad z = \pm 1. \quad (2.16)$$

## 2.3 The numerical schemes

### 2.3.1 The Frequency Domain Solution Method

The frequency domain solution is found by resolving (2.11) with boundary conditions (2.14). The heat equation is solved using the explicit DuFort-Frankel method, which gives second-order accuracy at each time step. The Helmholtz equation for the electric-field amplitude is discretized using central differences with the discretisation giving rise to the following matrix

$$A\mathbf{U}' = \mathbf{b}, \quad (2.17)$$

where the vector  $\mathbf{U}'$  represents the components of electric-field amplitude. The system matrix  $A \in \mathbb{C}^{n \times n}$  had dimension  $n = 5000$  and (2.17) is solved iteratively via *GMRES*, which is a Krylov subspace method. It was found that the subspace  $\mathcal{K}_\ell(\mathbf{A}, \mathbf{b})$  required dimension in the range  $\ell \in [100, 200]$  to reduce the system residual to  $1 \times 10^{-6}$ . The use of a preconditioner to improve the performance of the iterative solver will be the subject of future work.

### 2.3.2 The Time Domain Solution Method

The Maxwell's equations (2.1) were discretised using the FD-TD staggered in space and time methodology [5, 6, 7] over a given Cartesian *Yee* lattice. As discussed in §2.2, under the  $TE_{10}$  assumption the following field components are obtained from (2.1):

$$\frac{\partial \mathbf{H}_1}{\partial t} = \frac{1}{\mu} \frac{\partial \mathbf{E}_2}{\partial z}, \quad \frac{\partial \mathbf{H}_3}{\partial t} = -\frac{1}{\mu} \frac{\partial \mathbf{E}_2}{\partial x}, \quad \frac{\partial \mathbf{E}_2}{\partial t} + \frac{\sigma}{\epsilon} \mathbf{E}_2 = \frac{1}{\epsilon} \left( \frac{\partial \mathbf{H}_1}{\partial z} - \frac{\partial \mathbf{H}_3}{\partial x} \right). \quad (2.18)$$

To increase the spatial stability of the numerical solver [8], the electric and magnetic field components have been computed on cell edges and faces, respectively. By applying the leapfrog time discretisation [6] to (2.18) and rearranging the equation for  $H_1$  the following discrete analogue of the x-component of the magnetic field is obtained:

$$H_{1(i,j+\frac{1}{2},k+\frac{1}{2})}^{n+\frac{1}{2}} = H_{1(i,j+\frac{1}{2},k+\frac{1}{2})}^{n-\frac{1}{2}} + \frac{\delta_t}{\mu} \left( \frac{E_{2(i,j+\frac{1}{2},k+1)}^n - E_{2(i,j+\frac{1}{2},k)}^n}{\delta_z} \right). \quad (2.19)$$

Similar equations for  $H_3$  and  $E_2$  can also be obtained. Once the electric and magnetic fields have been computed for a sufficiently large number of periods, the power distribution can be calculated from the electric field alone:

$$P_{abs} = \frac{1}{q\lambda_T} \int_{p\lambda_T}^{(p+q)\lambda_T} \sigma \mathbf{E}^2(t) dt, \quad (2.20)$$

where  $p$  is the number of periods before the absorbed power ( $P_{abs}$ ) is computed,  $q$  is the number of periods for which the electric field has been time-averaged to obtain the power and  $\lambda_T$  is the period of the electromagnetic wave inside the waveguide. Typically  $p \gg q$  and  $q = 1$  is chosen so that the electric and magnetic fields have reached a so-called steady state inside the waveguide. In the numerical simulation performed here,  $p + q = 10$  was used and the power is computed according the following discrete form of (2.20):

$$P_{(i,j,k)}^n = \frac{1}{16} \sigma \left( E_{2(i,j+\frac{1}{2},k)}^n + E_{2(i+1,j+\frac{1}{2},k)}^n + E_{2(i,j+\frac{1}{2},k+1)}^n + E_{2(i+1,j+\frac{1}{2},k+1)}^n \right)^2. \quad (2.21)$$

The power distribution obtained from (2.21) is used in the forced heat equation (2.2) to compute the heat distribution inside the load. This is achieved through a forward time and centred space discretisation of equation (2.2) with the time step chosen to satisfy the stability requirement for this method.

The complete implementation of the coupled FD-TD and heat equation solution strategy is summarised in Figure 2.3.2. The figure illustrates the feedback mechanism used to compute, and hence, recompute the electromagnetic fields and consequently the heat distribution inside the ceramic load.

The time step associated with the FD-TD algorithm is  $O(10^{-12})$ , however, for the heat equation the time step of this scheme is much larger  $O(10^{-2})$ . Consequently, the power distribution can be obtained in an instance of the time scale of the heating. Therefore, the power is recomputed only when the properties of the material due to heating have substantially changed. Typically, the constraint on the recomputation of the power is triggered when

$$e = \left| \frac{\varepsilon''_{n+1}(T_{\max}) - \varepsilon''_n(T_{\max})}{\varepsilon''_n(T_{\max})} \right| < 5 \times 10^{-t}, \quad (2.22)$$

where,  $e$  is the measure of the error in the dielectric properties due to heating and  $t$  is a positive integer. In (2.22),  $n$  refers to the levels at which the power has been computed. It was found that varying the value of  $t$  in (2.22) slightly did not affect the quality of the final solution considerably. However larger values of  $t$  does impact substantially on the overall computational time. Equation (2.22) merely determines how long the heat equation is iterated before the power is recomputed and for the results reported here the value of  $t = 2$  was used.

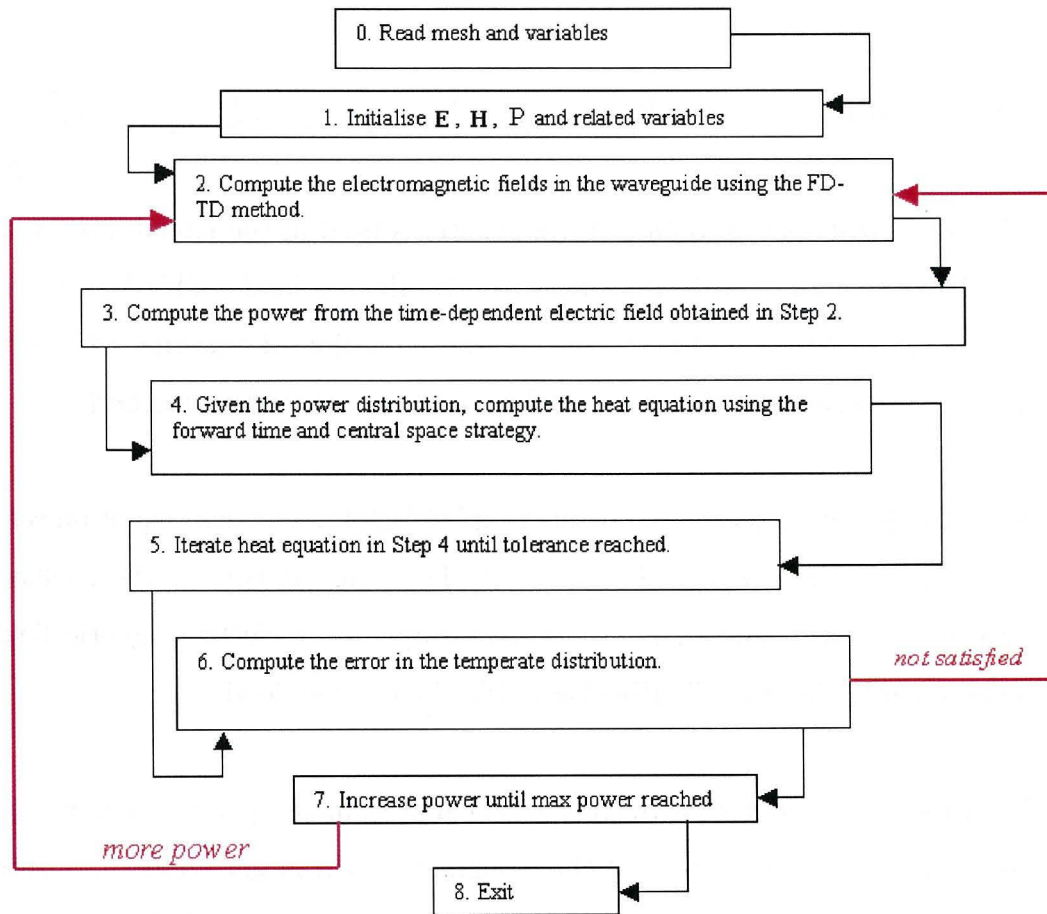


Figure 2.1: The flowchart of the numerical scheme.

## 2.4 Results and comparisons

The following physical properties were used for all simulation results given in this section:

$$\nu = 37.7 \text{ kg m s}^{-3} \text{ K}^{-1}, \quad C = 940 \text{ J kg}^{-1} \text{ K}^{-1}, \quad \rho = 3.58 \times 10^3 \text{ kg m}^{-3}. \quad (2.23)$$

The amplitude of the electric field is related to the average input power ( $P_{av\_in}$ ) by

$$E_0 = \sqrt{\frac{2P_{av\_in}\mu_0\omega}{\gamma}}, \quad \gamma = \sqrt{\omega^2\mu_0\varepsilon_0 - \left(\frac{\pi}{a}\right)^2}. \quad (2.24)$$

A cube of dimension  $a = 0.1m$  is considered where the cube fills the cross-section of the waveguide. The results are presented in non-dimensional form, with the FD-TD numerical solution non-dimensionalised for comparison purposes. As a cube is considered  $m = n = 1$  in (2.14). Other parameters in non-dimensional form are  $\alpha = 0.005$ ,  $k = k_1 = 2.57$  and  $k_r = 2.44$ .

Figure 2.2 shows the steady-state temperature versus power curve. Presented are the nondimensional maximum temperature in the block and the nondimensional power  $\beta$ . Shown are the semi-analytical solution and the frequency domain and FD-TD numerical solutions. The semi-analytical solution is found using the Galerkin method. Trial functions for the temperature and the electric-field amplitude are assumed and expressions for the decay of the electric-field and the power versus temperature curve are found by averaging over the slab, see [4] for more details of the technique.

The figure shows that an *S*-shaped response occurs. Thermal runaway arises at a critical  $\beta$  with the solution jumping from the lower (cool) branch to the upper (hot) branch. On the lower (cool) branch the comparison between the three solutions is excellent. On the upper (hot) branch the comparison is still very good with a difference of 8%, at  $\beta = 2$ . Moreover, the semi-analytical solution is very accurate, even for large  $\beta$ . The difference between the semi-analytical and frequency domain solutions at  $\beta = 2$  is 10%. No numerical results are available for the second solution branch, as it is unstable.

For the chosen value of  $k = 2.57$  both the  $TE_{10}$  and the  $TM_{11}$  modes can propagate in the waveguide as all higher modes are cut-off. However, examination of the FD-TD numerical solution shows that no other mode, besides the incident  $TE_{10}$  mode, is present in the waveguide or the heated material. Hence, the single-mode assumption, made in the frequency domain solution, is reason-

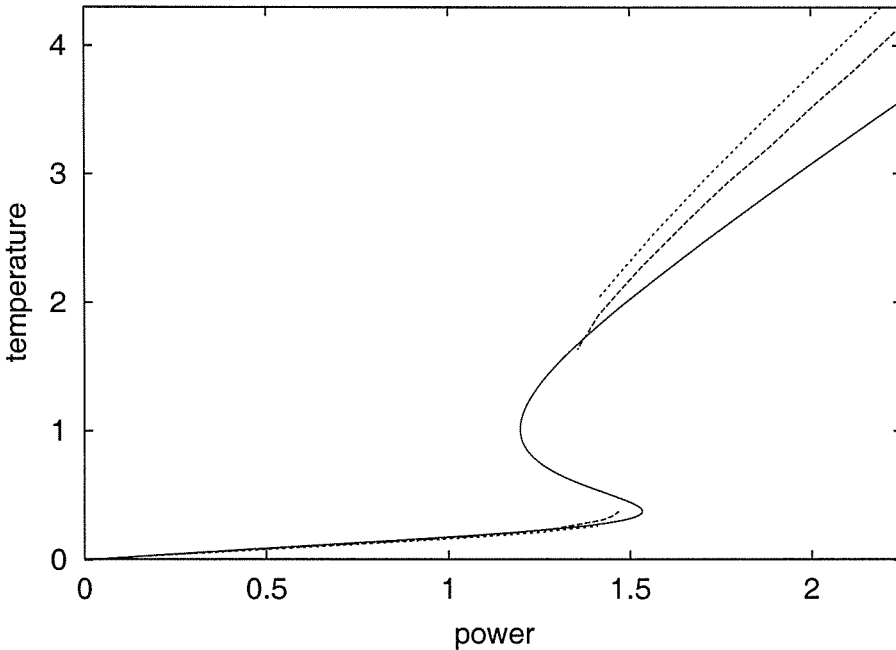


Figure 2.2: The steady-state power versus temperature curve. Shown are the semi-analytical solution, the frequency domain (large dashes) and the FD-TD (small dashes) numerical solutions.

able.

The frequency domain solutions are found using a spatial discretisation of  $\Delta z = 0.125$ , while the FD-TD solutions are found with a discretisation of  $\Delta z = 0.067$ . Hence the difference between the numerical solutions on the upper branch is most likely due to discretization error. Both the numerical solutions were found using a single Silicon Graphics processor capable of 800 MFlops. Each steady-state solution point takes a similar amount of CPU; 7 minutes for the frequency domain method and 10 minutes for the FD-TD method.

## 2.5 Conclusions

A comparison of the simulation results for a homogeneously loaded infinitely long waveguide using a semi-analytical method and both frequency and time domain numerical methods has been presented in this paper. The results highlight that all three methods show good agreement for the S-shaped curve for the ceramic like material. Furthermore, the assumption of a single mode within the waveguide is suitable for use in the frequency domain method.

Further work will concentrate on efficient numerical solutions for other waveguide scenarios such as a short-circuited guide and a cavity with an iris. The validity of the single mode assumption for other waveguide modes, such as the  $TM_{11}$  mode and in cavities will also be investigated. These investigations will lead to the authors developing efficient hybrid analytical and numerical schemes for microwave heating in waveguides and cavities.



# Bibliography

- [1] Hile, C.V. and Kriegsmann, G.A., *A hybrid numerical method for loaded highly resonant single mode cavities*. J. Comput. Phys, 1998, **142**: p. 506-520.
- [2] Kenkre, V.M., Skala, L., Weiser, M.W. and Katz, J.D., *Theory of microwave effects on atomic diffusion in sintering: basic considerations of the phenomenon of thermal runaway*. Microwave processing of materials II (ed. W.B. Snyder, W.H. Sutton, M.F. Iskander & D.L. Johnson), Material Research Society Symposium Proceedings, 1991, **189**: p. 179-183, Material Research Society.
- [3] Kriegsmann, G.A., *Cavity effects in microwave heating of ceramics*. SIAM J. Appl. Math, 1997, **57**: p. 382-400.
- [4] Liu, B. and Marchant, T.R., *The microwave heating of three-dimensional blocks: semi-analytical solutions*. IMA J. Appl. Maths, 2002, **67**: p. 145-175.
- [5] Metaxas, A.C. and Meredith, R.J., *Industrial Microwave Heating*. Peter Peregrinus Ltd. London, UK, 1983.
- [6] Zhao, H. & Turner, I.W., *An analysis of the finite-difference time-domain method for modelling the microwave heating of dielectric materials within a three-dimensional cavity system*. J. Micro. Power, 1996, **31**: p. 199-214.

- [7] Yee, K.S., *Numerical Solution of Initial Boundary Value Problem Involving Maxwell's Equations in Isotropic Media*. IEEE Trans. Antennas Propagat., 1966, **14**: p. 302-307.
- [8] Liu, Y., *Fourier Analysis of Numerical Algorithms for the Maxwell Equations*. J. Comput. Phys, 1996, **124**: p. 396-416.

# Chapter 3

## Comparison of Time Domain Numerical Solvers for the Propagation of a Gaussian Pulse Inside a Rectangular Waveguide

### Statement of Joint Authorship

**Vegh, V.** (Candidate) Numerically modelled a number of different time domain solvers for propagating a Gaussian pulse inside a waveguide, interpreted the results and wrote the manuscript, acted as corresponding author, proof read manuscript.

**Turner, I. W.** Suggested ways of improving the different numerical time domain solvers, directed and guided the work, assisted with interpretation of results and the preparation of the paper.

NOMENCLATURE	
<b>A</b>	Coefficient matrix
<b>d</b>	Right hand vector
<b>E</b>	Electric field intensity ( $V$ )
<b>J</b>	Electric current density ( $A/m^2$ )
<b>n</b>	Unit outward normal to face $F$
$a$	Broad dimension of waveguide ( $m$ )
$c_{max}$	Maximum wave speed ( $m/s$ )
$f$	Frequency ( $Hz$ )
$F$	Full field
$k$	Number of adjoining cells
$p$	The $p^{th}$ cell of the domain
$S$	Surface area ( $m^2$ )
$T$	Period inside waveguide ( $s$ )
$z_0$	Location of incident field ( $m$ )
$\delta$	Vector from cell centre to face
$\delta_y$	Cell dimension in the $y$ direction
$\Delta S$	Surface area of face $F$ ( $m^2$ )
$\Delta V$	Volume of the $p^{th}$ cell ( $m^3$ )
$\epsilon_0$	Free-space permittivity ( $8.85 \times 10^{-12}$ ) ( $F/m$ )
$\epsilon''$	Relative loss factor
$\omega$	Angular frequency ( $2\pi f$ ) ( $rad/s$ )
$\sigma$	Electric conductivity ( $\Omega^{-1}/m$ )
$\xi$	Discrete field component
<b>B</b>	Magnetic flux density ( $T$ )
<b>D</b>	Electric flux density ( $V/m$ )
<b>H</b>	Magnetic field intensity ( $A/m$ )
$\mathbf{J}^*$	Magnetic current density ( $\frac{HA}{F\Omega m^2}$ )
$\mathbf{r}$	Vector to node $p$
$c$	Wave speed ( $m/s$ )
$E_0$	Incident electric field amplitude
$F$	A face of cell $p$
$I$	Incident field
$n$	The $n^{th}$ time level
$S$	Scattered field
$t$	Time ( $s$ )
$V$	Volume ( $m^3$ )
$\beta_0$	Phase factor of free-space
$\delta_x$	Cell dimension in the $x$ direction
$\delta_z$	Cell dimension in the $z$ direction
$\Delta t$	Time step of numerical scheme ( $s$ )
$\epsilon$	Permittivity ( $F/m$ )
$\epsilon'$	Relative dielectric constant
$\mu_0$	Free-space permeability ( $4\pi \times 10^{-7}$ ) ( $H/m$ )
$\phi$	Continuous field component
$\sigma^*$	Magnetic conductivity ( $\frac{H}{F\Omega m}$ )
$\zeta_p$	Faces that constitute the $p^{th}$ cell

Table 3.1: List of symbols used in Chapter 3.

## Abstract

This research work analyses techniques for increasing the accuracy and efficiency of a finite-volume time-domain (FV-TD) cell-centred computational methodology. Various state-of-the-art spatial and temporal discretisation methods employed to solve Maxwell equations on multi-dimensional structured grid networks are investigated and the dispersive and dissipative errors inherent in those techniques examined. Both staggered and unstaggered grid approaches are considered. Staggered and unstaggered Leapfrog and Runge-Kutta time integration methods are analysed by the use of Gaussian microwave pulse simulations. The

implementation of typical electromagnetic boundary conditions is also deliberated. Finally, a comparison of the classical finite-difference time-domain (FD-TD) method and FV-TD numerical results for a standard case study in rectangular waveguides allows the accuracy of the developed methods to be assessed.

### 3.1 Introduction

In the past, a number of computational methodologies have been developed to solve Maxwell's Equations for a variety of important applications in Science and Engineering [1-4]. Although microwaves are frequently used for heating purposes, in this paper only microwave pulses are analysed for the purpose of radar and signal processing. Over the last two decades, research work in Computational Electromagnetics (CEM) has seen the development of approximations both for the integral and point forms of the governing Maxwell's equations. In this work, the traditional staggered in time and space FD-TD [5] scheme is compared to a number of cell-centred finite-volume time-domain approaches (ccFV-TD). Most of the schemes discussed here are formulated for generalised unstructured applications. However, this part of the research work is applied on a simpler structured mesh case study, to allow the numerical results to be compared directly to the FD-TD solution.

Staggered schemes store approximations of the components of the electromagnetic fields at different spatial locations within the computational domain. For example, FD-TD uses the Yee lattice to achieve that objective, as shown in Figure 3.1. In this case, the electric and magnetic fields are staggered also in time in order to stabilise the explicit time marching scheme. On the contrary, cell-centred schemes store all of the electromagnetic fields at the same spatial location (the cell centre). Typically, cell-centred schemes are much easier to manage and implement (in terms of algorithm planning, design and storage data structures)

in comparison with their staggered counterparts. Note however that even though the electric and magnetic field components are evaluated at the same locations inside a given cell, it is still possible to stagger the cell-centred in space schemes in time. These are usually classified as staggered and unstaggered leapfrog integrations in time, where the electric and magnetic field components are either stored at different locations or at the same location in time, respectively.

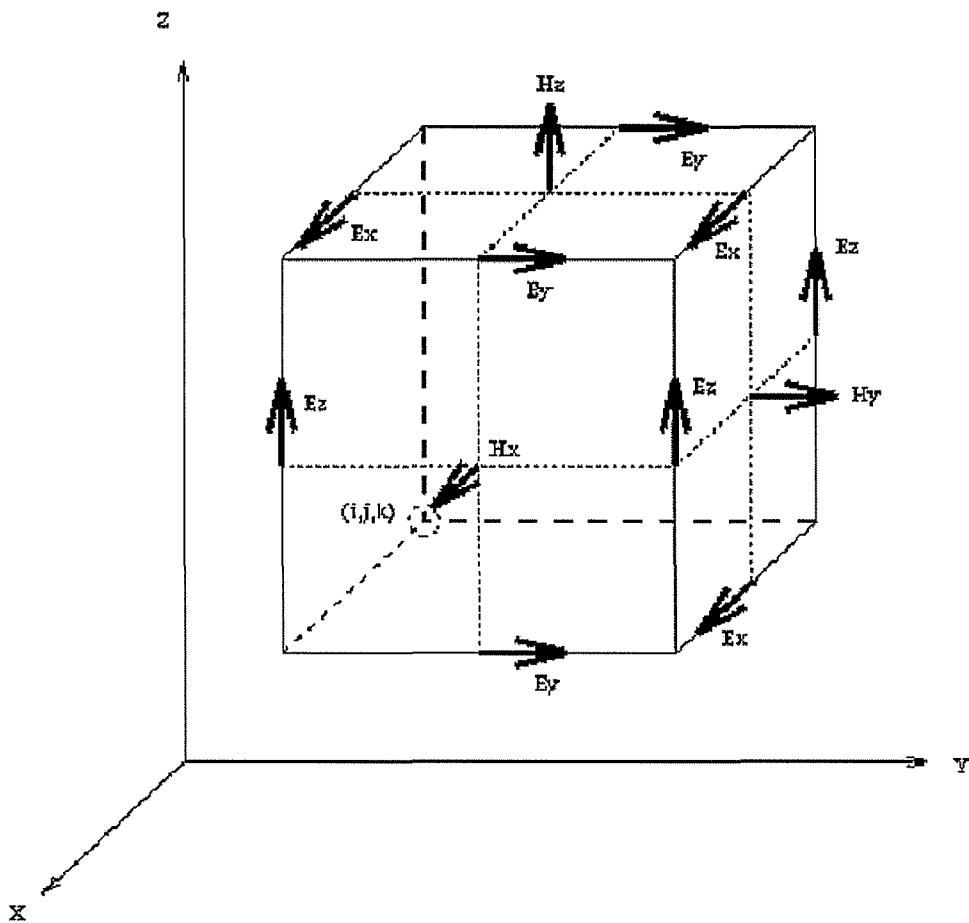


Figure 3.1: A Yee cell. The components of the electric (**E**) and magnetic (**H**) fields are stored at different locations along the cell edges and on the cell faces, respectively. For the FD-TD algorithm, the electric and magnetic fields are also staggered half a time step apart.

In this work,  $3^{rd}$  and  $4^{th}$  order Runge-Kutta (RK3 and RK4) methods are implemented also on the cell-centred in space approach to analyse their performance against the Leapfrog time marching schemes.

The problem studied here concerns a  $TE_{10}$  Gaussian pulse propagated longitudinally in a typical rectangular waveguide. The end of the waveguide is short-circuited, and the reflected waves are absorbed in the scattered field region of the waveguide. Initially, a detailed description of the mathematical formulation is provided for the time domain cell-centred in space methods, and typical boundary condition implementation for the conducting walls, input plane and absorbing boundary layer is deliberated. In the scattered field region of the waveguide, an existing Perfectly Matched Layer (PML) staggered in space methodology [6] is adapted to the cell-centred approaches to absorb any reflected impinging waves in the scattered field region of the waveguide.

Primarily, the propagating Gaussian pulse empty waveguide study allows the performance of the different Maxwell's equations time domain solvers to be analysed under free space conditions. The pulse presents a good test for the FV-TD methods, and highlights the evident dissimilarities between the different cell-centred schemes and shows also, the differences when compared to the FD-TD method. Depending on the spatial and temporal discretisation methods utilised, the schemes exhibit both dispersive and dissipative numerical errors. Dissipative errors cause the loss of wave amplitude, while dispersive errors affect the wave propagation speed. These errors are cumulative in nature and need to be monitored for a number of time steps.

This paper consists of five sections. In the next section the mathematical formulation for discretising Maxwell's equations using a finite-volume approach is presented, highlighting the different cell-centred schemes. Then there follows

a detailed discussion of the electromagnetic boundary condition implementation. In the proceeding section the results for the empty waveguide case study are presented, and comparisons between the different methods are provided via a number of graphical illustrations that elucidate the dissipative and dispersive nature of the different schemes. Finally, the conclusions of this work are summarised.

## 3.2 Cell-Centred Finite-Volume Time-Domain Methods

For the purpose of numerical simulation using a finite-volume methodology, the point form of the Maxwell's equations (3.1) must be recast into a discrete volumetric form:

$$\nabla \times \mathbf{E} = -\frac{\partial \mathbf{B}}{\partial t}, \quad \nabla \times \mathbf{H} = \frac{\partial \mathbf{D}}{\partial t} + \mathbf{J}, \quad (3.1)$$

$$\mathbf{B} = \mu_0 \mathbf{H}, \quad \mathbf{D} = \epsilon \mathbf{E}, \quad \mathbf{J} = \sigma \mathbf{E}, \quad \epsilon = \epsilon_0 \epsilon', \quad \sigma = \omega \epsilon_0 \epsilon'',$$

where,  $\mathbf{E}$  is the electric field,  $\mathbf{H}$  is the magnetic field,  $\mathbf{D}$  is the electric flux,  $\mathbf{B}$  is the magnetic flux,  $\mathbf{J}$  is the current density,  $\mu_0$  is the permeability of free-space,  $\epsilon_0$  is the permittivity of free-space,  $\epsilon$  is the permittivity,  $\epsilon'$  is the relative electric constant,  $\epsilon''$  is the relative loss factor,  $\sigma$  is the electric conductivity and  $\omega = 2\pi f$  where  $f$  is the input frequency. Note that for most microwave heating problems, the media are dielectric and current free. To arrive at the volumetric form, integration over a discrete finite volume cell is carried out. Unlike previous techniques where the integral was approximated using Stokes' theorem [3, 7], hence the Divergence theorem is applied to the volumetric representation to obtain a surface volume relationship between the electric and magnetic fields. The continuous equation is then cast into discrete form as follows:

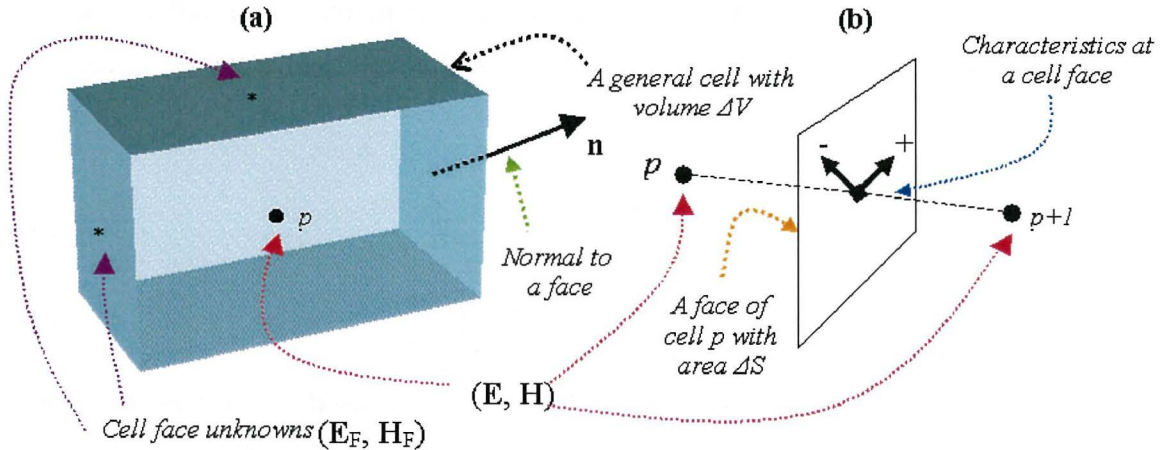


Figure 3.2: A general cell within the computational domain showing the locations of the unknowns.

$$\frac{\partial \mathbf{B}_p}{\partial t} = -\frac{1}{\Delta V} \sum_{F \in \zeta_p} \mathbf{n} \times \mathbf{E}_F \Delta S_F, \quad \frac{\partial \mathbf{D}_p}{\partial t} = \frac{1}{\Delta V} \sum_{F \in \zeta_p} \mathbf{n} \times \mathbf{H}_F \Delta S_F - \mathbf{J}_p, \quad (3.2)$$

where,  $\mathbf{n}$  is the unit outward normal through a face of a particular cell (see Figure 3.2). In equation (3.2),  $\zeta_p$  is the set of faces that constitute the  $p^{th}$  cell in a computational domain, and  $\Delta S_F$  and  $\Delta V$  are the surface area of a particular face in  $\zeta_p$  and the volume of the  $p^{th}$  cell, respectively. For the above discrete representation of Maxwell's equations (3.2), the surface integral approximation is second order in space if  $\mathbf{E}_F$  and  $\mathbf{H}_F$  are the values at the midpoint of the face. By visiting all of the cells that constitute the solution domain, a system of ordinary differential equations (ODEs) results. A number of methods are proposed to resolve the system of ODEs.

When approximating the differential operator in time, the discretisation can introduce either dispersion or dissipation errors (see [4]). Numerous techniques can be utilised to resolve (3.2) into time discrete form. In [8] a number of approaches similar to the FD-TD solution methodology have been investigated. For

a function  $\phi$ , equations (3.3) and (3.4) are the staggered (SLF) and unstaggered (ULF) leapfrog discretisations respectively, which are both  $O(\Delta t^2)$  approximations:

$$\frac{\partial \phi}{\partial t}^{n+\frac{1}{2}} = \frac{\phi^{n+1} - \phi^n}{\Delta t}, \quad (3.3)$$

$$\frac{\partial \phi}{\partial t}^n = \frac{\phi^{n+1} - \phi^{n-1}}{2\Delta t}. \quad (3.4)$$

Methods using the discretisations in (3.3) have been used in the past to numerically solve for the electromagnetic fields governed by Maxwell's equations. Using (3.3), the equations of (3.2) are written in discrete form as:

$$\mathbf{H}_p^{n+\frac{1}{2}} = \mathbf{H}_p^{n-\frac{1}{2}} - \frac{\Delta t}{\mu_0 \Delta V} \sum_{F \in \zeta_p} \mathbf{n} \times \mathbf{E}_F^n \Delta S_F, \quad (3.5)$$

$$\mathbf{E}_p^{n+1} = \frac{2\epsilon - \sigma \Delta t}{2\epsilon + \sigma \Delta t} \mathbf{E}_p^n - \frac{2\Delta t}{(2\epsilon + \sigma \Delta t) \Delta V} \sum_{F \in \zeta_p} \mathbf{n} \times \mathbf{H}_F^{n+\frac{1}{2}} \Delta S_F, \quad (3.6)$$

Similarly, (3.2) with the substitution of the discretisation in (3.4) becomes:

$$\mathbf{H}_p^{n+1} = \mathbf{H}_p^{n-1} - \frac{2\Delta t}{\mu_0 \Delta V} \sum_{F \in \zeta_p} \mathbf{n} \times \mathbf{E}_F^n \Delta S_F, \quad (3.7)$$

$$\mathbf{E}_p^{n+1} = \frac{\epsilon - \sigma \Delta t}{\epsilon + \sigma \Delta t} \mathbf{E}_p^{n-1} - \frac{2\Delta t}{(\epsilon + \sigma \Delta t) \Delta V} \sum_{F \in \zeta_p} \mathbf{n} \times \mathbf{H}_F^n \Delta S_F, \quad (3.8)$$

Equations (3.5) to (3.8) require the approximation to the electric and magnetic fields at the cell faces. It is possible to propose a number of interpolating and extrapolating schemes to approximate these cell face unknowns. On structured grids, the simplest way to approximate the unknowns at a cell face is by averaging the cell values about a particular face. Such a technique imposes second order in space and time for (3.5) to (3.8). These particular finite volume methods will be referred to as SLF (3.5)-(3.6), staggered in time and unstaggered in space, and ULF (3.7)-(3.8), unstaggered in space and unstaggered in time Leapfrog discretisations.

The averaging about a cell face demonstrates the simplest way to approximate the terms inside the summations in (3.5) to (3.8). At the  $p^{th}$  cell in equation (3.2), Intensity-Vector Splitting (IVS) [4], which is a concept that originated from Computational Fluid Dynamics (CFD), can be applied to replace the  $\mathbf{n} \times \mathbf{E}_F$  and  $\mathbf{n} \times \mathbf{H}_F$  terms. The notion behind IVS is to include an extra term in the flux facial expression to dampen any numerical oscillations, and to capture any discontinuities (such as shocks and contact surfaces in CFD) in the solution. At a cell face  $F$ , equations (3.9) and (3.10) depict the derived form of the IVS result:

$$\mathbf{n} \times \mathbf{E}_F = \frac{1}{2} \mathbf{n} \times (\mathbf{E}_F^+ + \mathbf{E}_F^-) + \frac{1}{2} \mathbf{n} \times ([\mu c]^+ \mathbf{n} \times \mathbf{H}_F^+ - [\mu c]^- \mathbf{n} \times \mathbf{H}_F^-), \quad (3.9)$$

$$\mathbf{n} \times \mathbf{H}_F = \frac{1}{2} \mathbf{n} \times (\mathbf{H}_F^+ + \mathbf{H}_F^-) - \frac{1}{2} \mathbf{n} \times ([\epsilon c]^+ \mathbf{n} \times \mathbf{E}_F^+ - [\epsilon c]^- \mathbf{n} \times \mathbf{E}_F^-), \quad (3.10)$$

where, the wave speed is given by  $c = \frac{1}{\sqrt{\mu\epsilon}}$ . It is evident from equations (3.9) and (3.10) that the + and – characteristics have to be approximated for a given cell face (see Figure 3.2). It should be noted that the IVS result cannot be implemented with (3.3), since the values for the magnetic and electric fields are required at different time levels. For this reason, time marching schemes that allow the electric and magnetic field components to be located at the same instant in time have to be employed. Numerical experimentation has shown that IVS when incorporated with (3.4) incurs large errors due to the time discretisation of the electric and magnetic fields [4]. Therefore, higher order time stepping methods are to be implemented. The following 3<sup>rd</sup> order Runge-Kutta (RK3) method was implemented with the IVS scheme discussed above:

$$\begin{aligned} \phi^{n+\frac{1}{3}} &= \phi^n + \frac{\Delta t}{3} \frac{\partial \phi^n}{\partial t}, & \phi^{n+\frac{2}{3}} &= \phi^n + \frac{2\Delta t}{3} \frac{\partial \phi^{n+\frac{1}{3}}}{\partial t}, \\ \phi^{n+1} &= \phi^n + \frac{\Delta t}{4} \left( 3 \frac{\partial \phi^{n+\frac{2}{3}}}{\partial t} + \frac{\partial \phi^n}{\partial t} \right). \end{aligned} \quad (3.11)$$

The outlined RK3 scheme is the one commonly used in CEM, and hence, it was

chosen to solve the equations of (3.2) that employ (3.9) and (3.10). Also, a 4<sup>th</sup> order Runge-Kutta (RK4) method was implemented:

$$\begin{aligned}\hat{\phi}^{n+\frac{1}{2}} &= \phi^n + \frac{\Delta t}{2} \frac{\partial \phi^n}{\partial t}, \quad \tilde{\phi}^{n+\frac{1}{2}} = \phi^n + \frac{\Delta t}{2} \frac{\partial \hat{\phi}^{n+\frac{1}{2}}}{\partial t}, \quad \bar{\phi}^{n+1} = \phi^n + \Delta t \frac{\partial \tilde{\phi}^{n+\frac{1}{2}}}{\partial t}, \\ \phi^{n+1} &= \phi^n + \frac{\Delta t}{6} \left( \frac{\partial \phi^n}{\partial t} + 2 \frac{\partial \hat{\phi}^{n+\frac{1}{2}}}{\partial t} + 2 \frac{\partial \tilde{\phi}^{n+\frac{1}{2}}}{\partial t} + \frac{\partial \bar{\phi}^{n+1}}{\partial t} \right).\end{aligned}\quad (3.12)$$

Substituting the IVS result into (3.2) and by applying the RK solvers of (3.11) and (3.12), the RK3-IVS and RK4-IVS techniques are obtained, respectively. Note that equation (3.2) can be solved using the RK3 and RK4 solvers without the inclusion of damping, and this suggestion is pursued later in this section. As shown in Figure 3.2, the + and – characteristics for the IVS are required at a particular cell face. Different strategies can be proposed and derived to approximate the values at the cell face joining any two adjacent cells. The simplest of these is the 0<sup>th</sup> order substitution for an unknown  $\xi$ :

$$\xi_{p+\frac{1}{2}}^- = \xi_p, \quad \xi_{p+\frac{1}{2}}^+ = \xi_{p+1}. \quad (3.13)$$

Imposing the 0<sup>th</sup> order approximation in RK3-IVS and RK4-IVS leads to a 1<sup>st</sup> order in space and 3<sup>rd</sup> order in time RK3-1-IVS numerical method, and a 1<sup>st</sup> order in space and 4<sup>th</sup> order in time RK4-1-IVS numerical method respectively. On a structured grid, a general linear extrapolation model that is 2<sup>nd</sup> order in space can also be derived:

$$\xi_{p+\frac{1}{2}}^- = \frac{1}{2} (3\xi_p - \xi_{p-1}), \quad \xi_{p+\frac{1}{2}}^+ = \frac{1}{2} (3\xi_{p+1} - \xi_{p+2}). \quad (3.14)$$

Using the approximations of (3.14), the RK3-2L-IVS and RK4-2L-IVS methods are developed, which are simultaneously the 3<sup>rd</sup> and 4<sup>th</sup> order in time and 2<sup>nd</sup> order in space linear extrapolation numerical schemes. By using discrete data points within the vicinity of the cell faces, it is possible to find least squares

gradient approximations at the cell centres [9]. Equation (3.15) is a truncated representation of the Taylor series:

$$\delta\mathbf{r} \cdot \nabla\xi(\mathbf{r}) \approx \xi(\mathbf{r} + \delta\mathbf{r}) - \xi(\mathbf{r}). \quad (3.15)$$

The above formula yields a system of linear equations that can be cast into matrix form as  $\mathbf{A} \cdot \nabla\xi_p = \mathbf{d}$ . The gradient that minimises  $\|\mathbf{A} \cdot \nabla\xi_p - \mathbf{d}\|^2$  with respect to the inner product on  $\mathbb{R}^k$  can be obtained by solving the normal equations. The value of  $k$  equals the number of neighbouring nodes utilised to obtain the gradient at the  $p^{th}$  cell. In this paper, the gradients were constructed using only the adjacent cells of  $\zeta_p$  (*i.e.*  $k = 6$ ). As a consequence, the gradients of the electric and magnetic fields can be used to approximate the + and – characteristics at the cell faces. Using these gradients, equation (3.16) establishes a  $2^{nd}$  order approximation for the + and – states:

$$\xi_{p+\frac{1}{2}}^- = \xi_p + \delta' \cdot \nabla\xi_p, \quad \xi_{p+\frac{1}{2}}^+ = \xi_{p+1} + \delta'' \cdot \nabla\xi_{p+1}. \quad (3.16)$$

In equation (3.16),  $\delta'$  and  $\delta''$  are the vectors from the nodes ( $p$ ) to ( $p + \frac{1}{2}$ ) and ( $p + 1$ ) to ( $p + \frac{1}{2}$ ), respectively (see Fig. 2). Subsequently, the methods that employ (3.16) are classified as RK3-2G-IVS and RK4-2G-IVS, depending on the time integration. The various IVS methods can also be implemented without flux splitting and are referred to here as the RK3(RK4)-2L and RK3(RK4)-2G methods, which are the  $3^{rd}$  ( $4^{th}$ ) order linear extrapolation and the spatial gradient approximations, respectively.

### 3.3 Boundary Conditions

In this section, the perfectly conducting wall, the incident field and absorbing boundary conditions are treated. On a perfectly conducting wall, the following conditions need to be satisfied [10]:

$$\mathbf{n} \times \mathbf{E} = 0, \quad \mathbf{n} \cdot \mathbf{H} = 0. \quad (3.17)$$

On structured grids, (3.17) implies that the tangential components of the electric field at a perfectly conducting wall boundary are zero. Equation (3.17) also entails that the magnetic components that are normal to that conducting wall are continuous across that wall.

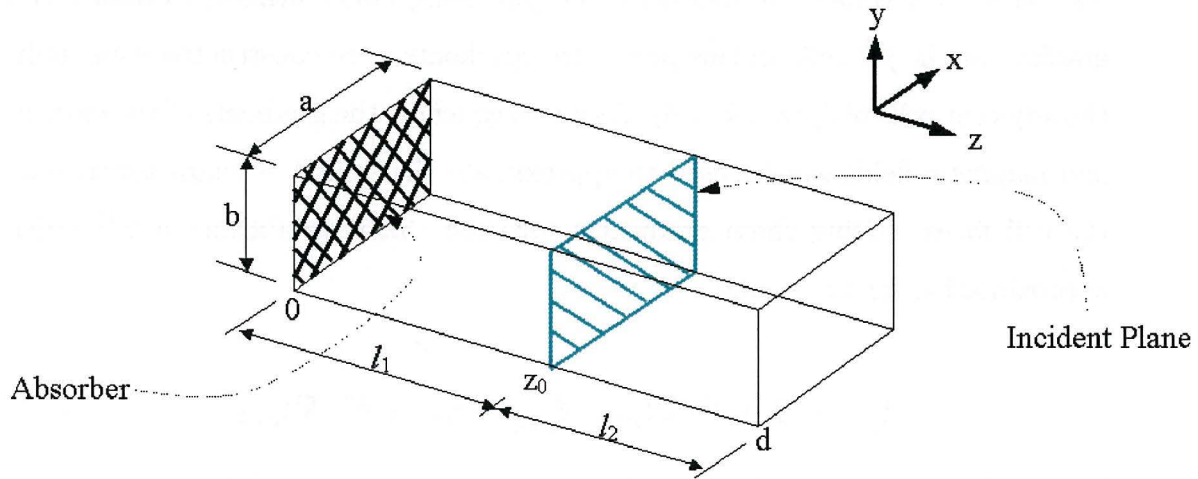


Figure 3.3: A waveguide with incident and absorbing boundary conditions.

For the implementation of the incident field boundary condition, a classical waveguide is depicted in Figure 3.3. Typically, a fictitious dielectric is introduced inside the scattered region to absorb any reflected backward travelling waves. In Figure 3.3 it is assumed that  $z_0$  represents the location where the incident field ( $I$ ) is located. The scatter field ( $S$ ) is the region between 0 and  $z_0$ , and the full field ( $F$ ) occupies the region between  $z_0$  and  $d$ . The scattered and full field regions have length  $l_1 = z_0$  and  $l_2 = d - z_0$ , respectively. At the input plane, the incident field is introduced using  $F = S + I$  and a continuous  $TE_{10}$  incident field is implemented as an input boundary condition. Across the input plane, the scattered and full fields are computed according to the following incident field

assumptions:

$$E_y^I = E_0 \sin \frac{\pi x}{a} \cos(\omega t - \beta_0 z_0), \quad (3.18)$$

$$H_x^I = -\frac{\beta_0}{\omega \mu_0} E_0 \sin \frac{\pi x}{a} \cos(\omega t - \beta_0 z_0), \quad (3.19)$$

$$H_z^I = -\frac{\pi}{\omega \mu_0 a} E_0 \cos \frac{\pi x}{a} \sin(\omega t - \beta_0 z_0), \quad (3.20)$$

$$\beta_0 = \sqrt{\omega^2 \mu_0 \epsilon_0 - \left(\frac{\pi}{a}\right)^2}.$$

In Figure 3.3, an absorbing boundary layer is represented inside the scatter field region of the waveguide. A previously proposed Perfectly Matched Layer (PML) boundary condition [6] has been used to absorb any waves inside the scattered field region of the waveguide. In this work, this boundary condition has been adapted for the use in the cell-centred schemes discussed in the previous section. The PML boundary condition is based on matching the impedance of the absorbing medium to the impedance of free-space. The PML boundary conditions are based on the following augmented Maxwell's equations:

$$\frac{\partial \mathbf{B}}{\partial t} + \mathbf{J}^* = \nabla \times \mathbf{E}, \quad \frac{\partial \mathbf{D}}{\partial t} + \mathbf{J} = -\nabla \times \mathbf{H}, \quad (3.21)$$

where,

$$\mathbf{J}^* = \sigma^* \mathbf{H}, \quad \sigma^* = \frac{\mu_0}{\epsilon_0} \sigma. \quad (3.22)$$

By satisfying (3.22), the impedance of the PML equals that of free-space, and no reflections occur. From the reformulation of the Maxwell's equations, (3.1) is replaced by (3.21) in the discretisations, and new discrete in space equations are obtained for the numerical simulation of the electromagnetic behaviour within the absorbing material. Specific implementation details of the PML absorber will be outlined in future work, which will demonstrate the cell-centred finite-volume time-domain methods for the purpose of microwave heating.

## 3.4 Results

The waveguide of Figure 3.3 is used as a case study to numerically simulate a Gaussian microwave pulse inside the apparatus. The full field region of the waveguide is truncated via a short-circuit, and the scattered field region employs the Petropoulos type PML boundary condition to absorb any backward travelling waves. The dimension of the waveguide is  $a = 0.1\text{ m}$ ,  $b = 0.05\text{ m}$  and  $d = 0.4\text{ m}$ . At  $z_0 = 0.1\text{ m}$ , the incident plane is excited using a  $TE_{10}$   $2.45GHz$  electromagnetic wave, with an average input power of  $1W$ . The  $TE_{10}$  wave is multiplied by a Gaussian function to propagate a microwave pulse inside the waveguide:

$$Gauss(t) = e^{(-\frac{2.5t}{T}-1)^2}. \quad (3.23)$$

In equation (3.23),  $T$  represents the wave period inside the waveguide. The instantaneous electromagnetic fields were monitored over two periods. The domain of the waveguide is discretised into 54 000 ( $30 \times 15 \times 120$ ) Cartesian cells. The time stepping of the numerical solvers is constrained by the relationship:

$$\Delta t = \frac{0.9}{c_{\max} \sqrt{\frac{1}{\delta_x^2} + \frac{1}{\delta_y^2} + \frac{1}{\delta_z^2}}}, \quad (3.24)$$

where,  $c_{\max}$  is the maximum expected wave speed in the waveguide, and  $\delta_x$ ,  $\delta_y$  and  $\delta_z$  are the minimum mesh dimensions in the  $x$ ,  $y$  and  $z$  coordinate directions [2]. Figures 3.4 and 3.5 show the results for the simulated  $TE_{10}$  Gaussian pulse using the numerical techniques discussed throughout the previous sections. Since it is well known that the FD-TD scheme is highly accurate, all of the established cell-centred numerical techniques have been compared to the FD-TD method to demonstrate the relative accuracy of each scheme. It is evident from the figures that the unstaggering of the unknowns introduces errors, and hence, higher order time marching schemes are required to better capture the FD-TD solution.

In the proceeding paragraphs, specific comments regarding the accuracy of the schemes presented in §3.2 and exhibited in Figures 3.4 and 3.5 are given. The introduction of intensity vector splitting smoothes the noise that is apparent in the ULF, SLF and RK3(RK4)-2G techniques (see Figures 3.4[a], 3.4[b], 3.4[c] and 3.5[c]). It is well known that using higher order time integration techniques requires more computational effort to resolve the unknowns (*i.e.* CPU time and memory requirements), and consequently, the techniques that employ IVS with RK3 and RK4 time integration are more computationally intensive than the FD-TD method. In this work, only the accuracy of the different cell centred schemes are compared, an analysis of the times to compute the numerical solutions has been left for future investigations. It can be seen from the figures that the methods that make use of the gradients to approximate the + and – characteristics at the cell faces can capture the pulse as well as any of the other cell-centred numerical schemes discussed (see Figures 3.4[c-d] and 3.5[c-d]). Note that the results for RK3(RK4)-2L-IVS have not been shown, since they were comparable to those obtained using RK4-2G-IVS. In the numerical solutions it was observed also that results for RK3-2L were comparable to the RK4-2L scheme, and as a consequence, only the RK4-2L results are illustrated.

From the figures it is evident that the adaptation of IVS in the schemes (see Figures 3.4[d], 3.5[b] and 3.5[d]) smooth the results. Although, it should be noted that the RK4-2L scheme has apparent smoothing also. This is because the approximation uses a second order linear extrapolation, which removes any rapid changes or oscillations in the numerical time marching. In Figure 3.4[a] it is observed that the ULF scheme is conditionally unstable [4]. Figure 3.5[b] highlights that the RK4-1-IVS scheme, which utilises the 0<sup>th</sup> order extrapolation for the + and – characteristics, is highly dissipative as observed by Liu [4]. Furthermore, the first order spatial discretisation inadequately captures the behaviour of the

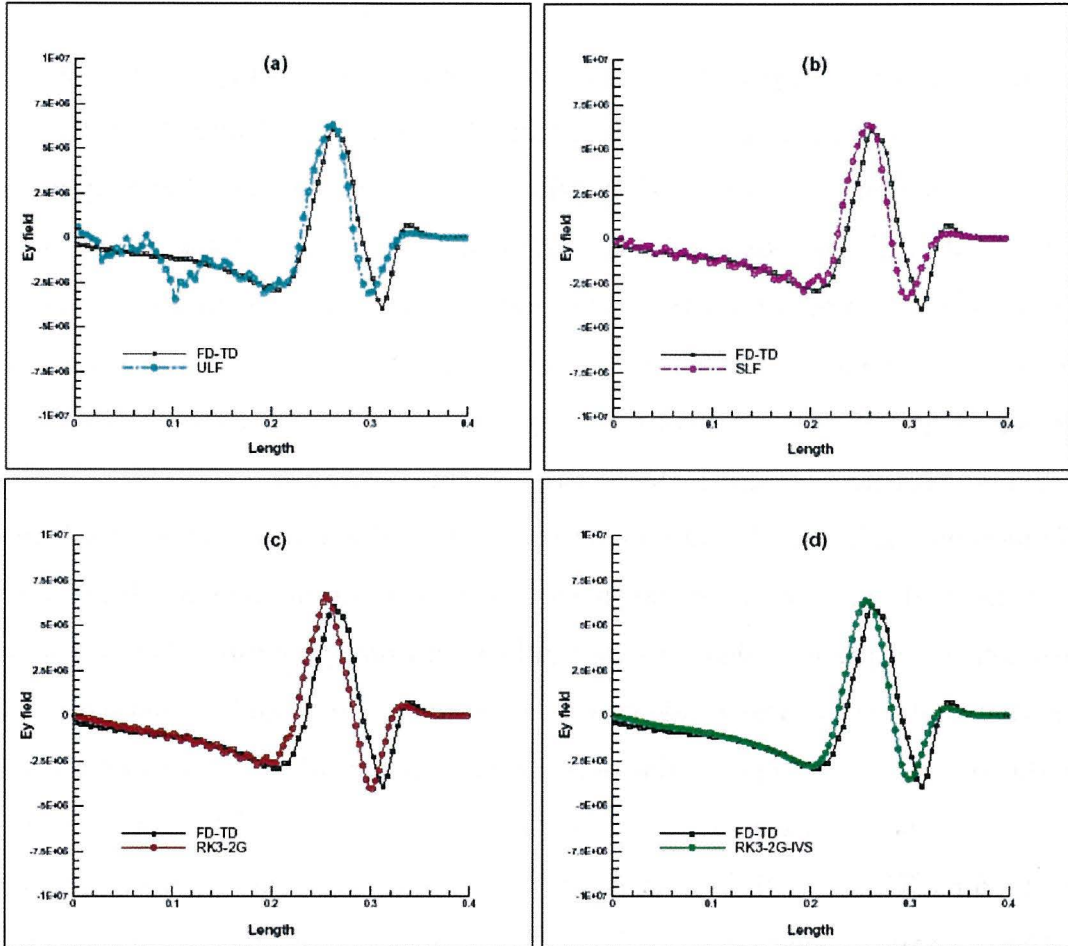


Figure 3.4: A two period pulse inside a  $TE_{10}$  waveguide showing time versus the  $y$ -coordinate of the Electric field ( $V/m$ ); (a) ULF; (b) SLF; (c) RK3-2G and (d) RK3-2G-IVS.

solution. However, it must be noted that such methods are able to capture the wave phase, but the amplitude is smeared considerably.

In Figures 3.4[c-d] and 3.5[c-d] it is observed that the numerical solution is out of phase with the FD-TD benchmark solution. In Figure 3.5[a] the RK4-2L scheme, which is suitable only for structured grids, appears to capture the wave phase. These findings are an artifact of the spatial discretisation, and to further investigate how the phase errors could be reduced, higher order spatial

discretisations would have to be adapted to the previously outlined cell-centred schemes. The ULF, SLF, RK3(RK4)-2L and RK4-1-IVS techniques exhibit substantial wave front amplitude errors (see Figures 3.4[a-b] and 3.5[a-b]). For the RK3(RK4)-2L method this is because of the grid used in the approximation of the cell face unknowns is four grid cells wide. Hence, as the incident field is propagated, the apparent noise due to the introduction of the microwave energy is propagated with the pulse.

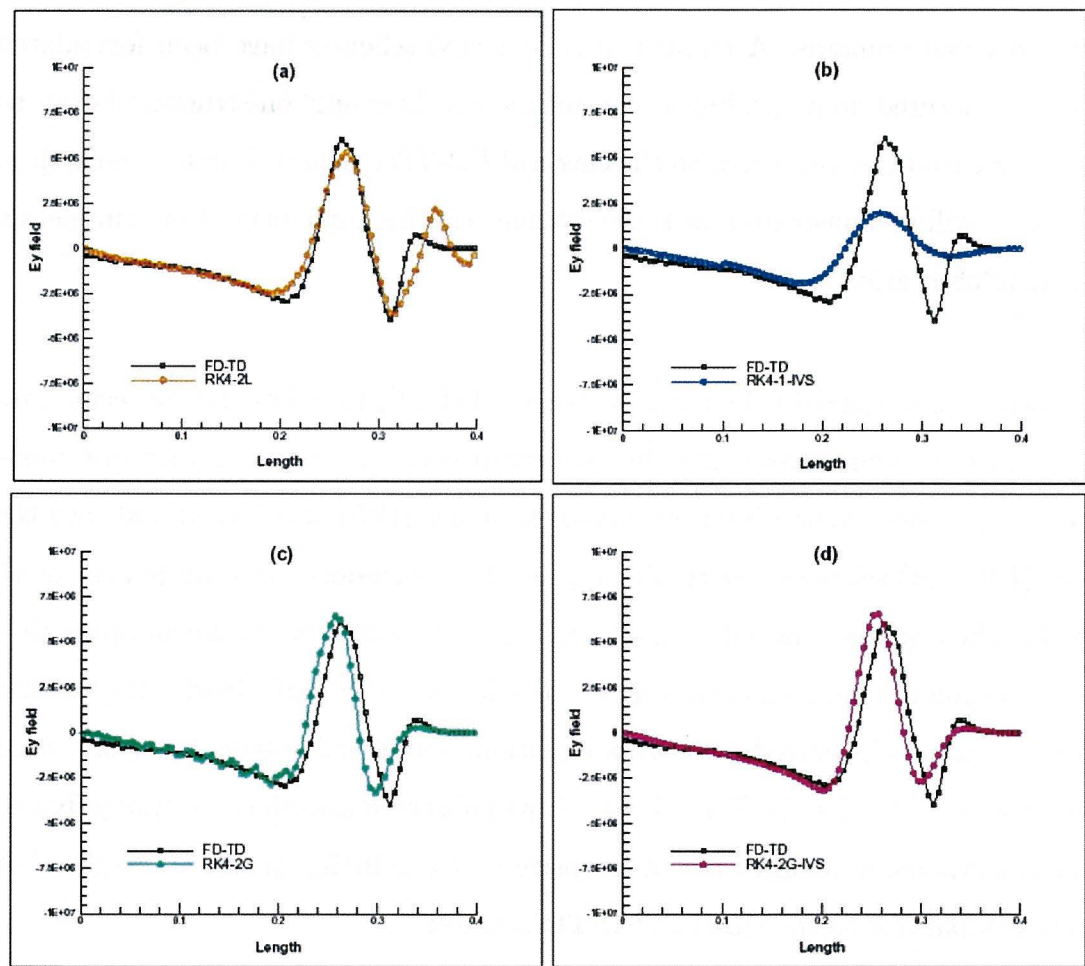


Figure 3.5: A two period pulse inside a  $TE_{10}$  waveguide showing time versus the  $y$ -coordinate of the Electric field ( $V/m$ ); (a) RK4-2L; (b) RK4-1-IVS; (c) RK4-2G and (d) RK4-2G-IVS.

### 3.5 Conclusion

In this work, cell centred time domain solvers for the Maxwell's equations were investigated and a number of solution strategies have been applied to resolve the Gaussian pulse waveguide study. The governing equations were discretised using non-traditional techniques to obtain a surface-volume representation that was solved numerically using a number of different numerical strategies. It is well known that the FD-TD method is very accurate, but it is not easily migrated to unstructured domains. A number of cell-centred schemes have been formulated for unstructured domains, but were implemented here only on structured grids so that they could be compared to the classical FD-TD method. Further research in the area will demonstrate how these schemes can be implemented on completely unstructured grids.

Leapfrog staggered (SLF) and unstaggered (ULF) time integration techniques were used to time march the discrete surface-volume representation of Maxwell's equations. When intensity vector splitting (IVS) was introduced into the RK3(RK4)-2G schemes, the results appeared to be smooth, and the evident noise in the schemes was removed. This reduction in noise was due to the damping that these techniques induced in the numerical solution. The work clearly showed that time domain cell-centred Maxwell's equations numerical solvers have produced reasonable results for the SLF scheme. It was observed also that the Runge-Kutta based methods, with and without intensity vector splitting produced results that were comparable to the classical FD-TD method.

For the purpose of microwave heating, future research will analyse in more detail the effect that a lossy material can have on the electromagnetic phenomenon evolving on the grid. In that work, more rigorous tests are to be conducted regarding dispersion and dissipation errors.

**Acknowledgements:** The authors would like to thank Dr. Huawei (Bob) Zhao for his input into the development of this paper. Also, many thanks to Dr. Joseph Young for his help with the visualisations in the accompanying presentation.



# Bibliography

- [1] Dibben, D.C. and Metaxas, A.C., *Time Domain Finite Element Analysis of Multimode Microwave Applicators Loaded with Low and High Loss Materials*. Intl. Proceedings 5th Microwave and High Frequency Heating Conf., St John's College, Cambridge, pp. A3.1-A3.4, September 1995.
- [2] Zhao, H. and Turner, H., *An analysis of the finite-difference time-domain method for modelling the microwave heating of dielectric materials within a three-dimensional cavity system*. Journal of Microwave Power and Electromagnetic Energy, 1996, 31(4): p. 199-214.
- [3] Madsen, N.K. and Ziolkowski, R.W., *A three-dimensional modified finite volume technique for Maxwell's equations*. Electromagnetics, 1990, (10): p. 147-161.
- [4] Liu, Y., *Fourier Analysis of Numerical Algorithms for the Maxwell Equations*. Journal of Computational Physics, 1996, 124: p. 396-416.
- [5] Yee, K.S., *Numerical Solution of Initial Boundary Value Problem Involving Maxwell's Equations in Isotropic Media*. IEEE Trans. Antennas Propagat., 1966, 14: p. 302-307.
- [6] Petropoulos, P.G., Zhao, L. and Cangellaris, A.C., *A Reflectionless Sponge Layer Absorbing Boundary Condition for the Solution of Maxwell's Equations*.

*tions with High-Order Staggered Finite Difference Schemes.* Journal of Computational Physics, 1998, **139**: p. 184-208.

- [7] Madsen, N.K. and Ziolkowski, R.W., *Numerical solution of Maxwell's equations in the time domain using irregular nonorthogonal grids.* Wave Motion, 1988, **(10)**: p. 583-596.
- [8] Taflove, A., *Re-inventing Electromagnetics: Supercomputing Solution of Maxwell's Equations Via Direct Time Integration on Space Grids.* AIAA paper 92-0333, 1992, (New York).
- [9] Barth, T.J., *Aspects of Unstructured Grids and Finite-Volume Solvers for the Euler and Navier-Stokes Equations.* Lecture Notes Presented at the VKI Lecture Series, 1994-05, 1995.
- [10] Collin, R.E., *Field Theory of Guided Waves.* 1960, McGraw-Hill Book Company.

# Chapter 4

## Effective Cell-Centred Time-Domain Maxwell's Equations Numerical Solvers for the Purpose of Microwave Heating

### Statement of Joint Authorship

**Vegh, V.** (Candidate) Numerically modelled various cell-centred time domain solvers for the modelling of electromagnetic fields inside an empty and loaded waveguide, interpreted the results and wrote the manuscript, acted as corresponding author, proof read manuscript.

**Turner, I. W.** Suggested ways of improving the different numerical time domain solvers, directed and guided the work, assisted with interpretation of results and the preparation of the paper.

**Zhao, H.** Provided feedback on the various cell-centred time-domain solvers, assisted with the FD-TD method, interpreted the results and proof read the manuscript.

NOMENCLATURE	
<b>A</b>	Coefficient matrix
<b>d</b>	Right hand vector
<b>E</b>	Electric field intensity ( $V$ )
<b>J</b>	Electric current density ( $A/m^2$ )
<b>n</b>	Unit outward normal to face $F$
$a$	Broad dimension of waveguide ( $m$ )
$c$	Wave speed ( $m/s$ )
$f$	Frequency ( $Hz$ )
$E_{av}$	Time averaged electric field
$F$	A face of cell $p$
$I$	Variable
$L$	Left state
$n$	The $n^{th}$ time level
$p$	The $p^{th}$ cell of the domain
$R$	Right state
$S$	Surface area ( $m^2$ )
$t$	Time ( $s$ )
$T$	Total field
$V_p$	Volume of cell $p$ ( $m^3$ )
$\beta$	Phase factor
$\delta$	Vector from cell centre to face
$\delta_y$	Cell dimension in the $y$ direction
$\Delta S$	Surface area of face $F$ ( $m^2$ )
$\Delta V$	Volume of the $p^{th}$ cell ( $m^3$ )
$\epsilon_0$	Free-space permittivity ( $8.85 \times 10^{-12}$ ) ( $F/m$ )
$\epsilon''$	Relative loss factor
$\omega$	Angular frequency ( $2\pi f$ ) ( $rad/s$ )
$\sigma$	Electric conductivity ( $\Omega^{-1}/m$ )
$\xi$	Discrete field component
<b>B</b>	Magnetic flux density ( $T$ )
<b>D</b>	Electric flux density ( $V/m$ )
<b>H</b>	Magnetic field intensity ( $A/m$ )
$J^*$	Magnetic current density ( $\frac{H_A}{F\Omega m^2}$ )
$r$	Vector to node $p$
$b$	Narrow dimension of waveguide ( $m$ )
$c_{max}$	Maximum wave speed ( $m/s$ )
$E_0$	Incident electric field amplitude
$E_c$	Computed electric field
$I$	Incident field
$k$	Number of adjoining cells
$n$	Normal component
$N$	Number of time samples
$P_0$	Average input power ( $W/m^2$ )
$S$	Scattered field
$t$	Tangential component
$T$	Period inside waveguide ( $s$ )
$V$	Volume ( $m^3$ )
$z_0$	Location of incident field ( $m$ )
$\beta_0$	Phase factor of free-space
$\delta_x$	Cell dimension in the $x$ direction
$\delta_z$	Cell dimension in the $z$ direction
$\Delta t$	Time step of numerical scheme ( $s$ )
$\epsilon$	Permittivity ( $F/m$ )
$\epsilon'$	Relative dielectric constant
$\mu_0$	Free-space permeability ( $4\pi \times 10^{-7}$ ) ( $H/m$ )
$\phi$	Continuous field component
$\sigma^*$	Magnetic conductivity ( $\frac{H}{F\Omega m}$ )
$\zeta_p$	Faces that constitute the $p^{th}$ cell

Table 4.1: List of symbols used in Chapter 4.

## Abstract

This research work analyses techniques for implementing a cell-centred finite-volume time-domain computational methodology for the purpose of microwave heating. Various state-of-the-art spatial and temporal discretisation methods

employed to solve Maxwell's equations on multi-dimensional structured grid networks are investigated, and the dispersive and dissipative errors inherent in those techniques examined. Both staggered and unstaggered grid approaches are considered. Upwind schemes using a Riemann solver and intensity vector splitting are studied and evaluated. Staggered and unstaggered Leapfrog and Runge-Kutta time integration methods are analysed in terms of phase and amplitude error to identify which method is the most accurate and efficient for simulating microwave heating processes. The implementation and migration of typical electromagnetic boundary conditions from staggered in space to cell-centred approaches also is deliberated. In particular, an existing Perfectly Matched Layer absorbing boundary methodology is adapted to formulate a new cell-centred boundary implementation for the ccFV-TD solvers. Finally for microwave heating purposes, a comparison of analytical and numerical results for standard case studies in rectangular waveguides allows the accuracy of the developed methods to be assessed.

## 4.1 Introduction

Over the years, numerous computational models have been investigated and developed for the solution of Maxwell's equations for a variety of important applications in Science and Engineering [1-4]. Typically, researchers implement solution methodologies that simulate instantaneous electromagnetic fields, and these are used to obtain the steady-state electromagnetic wave phenomena inside a microwave heating apparatus.

The scope of this research work focuses on the use of cell-centred time-domain finite-volume (ccFV-TD) solvers for investigating electromagnetic field behaviour during microwave heating processes. For domestic and industrial microwave heating applications, the time-averaged electric and magnetic fields have to be computed. From the computed time-averaged fields the power can be obtained easily,

and hence, the microwave power distribution can be coupled with the forced heat equation to obtain the temperature distribution inside the dielectric medium.

In this paper, numerous cell-centred time-domain schemes are presented and assessed in terms of computational speed, phase and amplitude error, in order to identify the most accurate and efficient method that can be used to obtain the time-averaged electric field distribution inside the load in a waveguide. The time-averaged fields are computed for various case studies, and are compared to the results obtained using the classical finite-difference time-domain (FD-TD) [5] and the analytic solutions where possible. The computation of the power and subsequently the determination of the heat distribution inside the medium are left to future research by the authors.

Historically, both the integral and point forms of the governing Maxwell's equations have been approximated in Computational Electromagnetics (CEM). The ccFV-TD methods discussed here are formulated from a discrete volume-surface representation of the governing equations. When developing finite-volume or finite-difference stencils to locate the electromagnetic unknowns within a discrete cell, the approximations to the components of the electromagnetic fields are stored at different spatial locations. For example, FD-TD uses the Yee lattice to locate the components of the unknowns around a cell. The electric and magnetic fields are staggered also in time in order to stabilise the explicit time marching scheme.

Cell-centred schemes store all of the electromagnetic fields at the same spatial location, which is normally at the centre of the finite-volume cell. Given that the spatial locations of the electric and magnetic field components are located at the same point, cell-centred schemes are much easier to manage, develop and implement in comparison with their staggered counterparts. By the nature of

the staggering of the unknowns in the FD-TD method, the inherent errors are reduced and this location in time and space of the electric and magnetic field components establishes a highly accurate scheme for structured grids. Unfortunately due to this staggering, the FD-TD scheme is difficult to implement on unstructured grids, and in this case cell-centred schemes are more viable. Nevertheless, rigorous consideration needs to take place to achieve sufficient accuracy in the cell-centred schemes. Despite the fact that for each cell the unknowns are positioned at the same spatial location, it is still possible to stagger the electric and magnetic field components in time. For cell-centred schemes this can stabilise the time marching of the numerical solver. It is possible also that higher order approximations in both time and space have to be considered to obtain a more accurate ccFV-TD scheme.

In the last decade, techniques from Computational Fluid Dynamics (CFD) have been adapted to CEM [4, 6, 7] with reasonable success. In this work, the uses of intensity vector splitting (IVS) and Riemann solvers (RS) are analysed, and mathematical formulations are given. Methods that employ techniques from CFD are known to be dissipative by nature. Munz et al [8] discuss a finite-volume solver for the Maxwell's equations in curvilinear non-orthogonal coordinates without the use of dimensional splitting. The local wave propagation between adjacent grid cells is determined by the solution of Riemann problems. A thorough analysis of the characteristic methods used to determine the required solution is given in [4] and the reader is referred there for the finer details.

The characteristic theory [4] requires the flux to be split into + and - states at a cell interface, then a number of different numerical approximations are applied to determine these states. In this work, the schemes used to approximate the states are presented in a way that can easily be generalised to a completely unstructured mesh framework. However, in an attempt to gauge the accuracy

and efficiency of the schemes investigated, it was decided to restrict the study here only to a structured mesh domain based on hexahedra, since the FD-TD method performs accurately on such grids and can be used for comparison. The migration of the cell-centred finite-volume method to an unstructured case will be the subject of future research.

Note that when these CFD type schemes are used to dampen any oscillatory behaviour due to spatial discretisation errors caused by the cell-centred strategy, it becomes necessary to employ higher order time integration techniques to resolve the differential system in time. Here 3rd and 4th order Runge-Kutta (RK3, RK4) methods are implemented on the cell-centred approaches to analyse their performance. However, the schemes that do not contain the damping term are discretised in time using second order Leapfrog time marching schemes that are staggered and unstaggered in time. Also, the schemes that utilise RK3 and RK4 time integrations with damping are implemented without the inclusion of the damping term, so that the effect of the term from the CFD methodology can be analysed for CEM applications.

In this paper, the solutions of typical waveguide problems are presented for two distinct case studies. The first concerns an empty waveguide study and the second a loaded waveguide study. The same numerical solvers are implemented in both cases. Initially, a detailed description of the mathematical formulation is provided for the time domain cell-centred in space methods, and typical boundary condition implementation for the conducting walls, input plane, material interface and a new cell-centred absorbing boundary layer is deliberated. In the scattered region of the waveguide, an existing Perfectly Matched Layer (PML) methodology [9] is reformulated and complemented for cell-centred schemes. As a subsequence, this new PML formulation is adapted to the cell-centred finite-volume schemes to absorb any reflected impinging waves in the scattered field

region of the waveguide.

Primarily, the empty waveguide study allows the performance of the different Maxwell's equation time-domain solvers to be analysed under free space conditions. Depending on the spatial and temporal discretisation methods utilised, the schemes exhibit both dispersive and dissipative numerical errors. Dissipative errors cause the loss of wave amplitude, while dispersive errors affect the wave propagation speed. These errors are cumulative in nature and their analyses are provided in the form of phase and loss or gain in amplitude. The time-averaged electric fields inside an empty waveguide are investigated. The computed fields are compared to both the FD-TD and exact solutions. It is observed that the second order accurate in space and time cell-centred methods are competitive in terms of accuracy and efficiency when compared to the FD-TD solver.

For the next case study, the waveguide is analysed when loaded with a dielectric material. A number of simulations for a short-circuited rear end loaded waveguide are presented. The simulation results are then compared to the analytic and FD-TD solutions. A loaded multi-mode waveguide is analysed also, and the results are compared to the FD-TD method. It is shown that cell-centred schemes can be implemented in a straightforward manner to resolve the time averaged electric fields inside a waveguide structure, and capture the analytic and FD-TD solutions more than adequately. The outcomes indicate that cell-centred schemes can be used with confidence for simulating the microwave power inside a load within a microwave apparatus.

This paper is organised as follows. In the next section, the mathematical formulation for discretising Maxwell's equations using a finite-volume approach is presented, highlighting the different cell-centred schemes. Followed by a detailed discussion of the EM boundary condition implementation. Thereafter, the results

for the different waveguide case studies are presented and comparisons between the various methods are provided via a number of graphical illustrations that elucidate the dissipative and dispersive nature of the different schemes. A table of amplitude and phase errors is provided also to highlight the evident differences between the methods. Finally, the main conclusions of this work are summarised.

## 4.2 Mathematical Formulations

For the purpose of numerical simulation using a finite-volume methodology, the point form of the Maxwell's equations:

$$\nabla \times \mathbf{E} = -\frac{\partial \mathbf{B}}{\partial t}, \nabla \times \mathbf{H} = \frac{\partial \mathbf{D}}{\partial t} + \mathbf{J} \quad (4.1)$$

$$\mathbf{B} = \mu_0 \mathbf{H}, \mathbf{D} = \epsilon \mathbf{E}, \mathbf{J} = \sigma \mathbf{E}, \epsilon = \epsilon_0 \epsilon', \sigma = \omega \epsilon_0 \epsilon''.$$

must be recast into a discrete volumetric form by integrating over a discrete finite-volume cell to obtain:

$$\iiint_V \nabla \times \mathbf{E} \partial V = - \iiint_V \frac{\partial \mathbf{B}}{\partial t} \partial V, \iiint_V \nabla \times \mathbf{H} \partial V = \iiint_V \frac{\partial \mathbf{D}}{\partial t} \partial V + \iiint_V \mathbf{J} \partial V. \quad (4.2)$$

Unlike approximating an integral formulation based on the Stokes' theorem [3, 10], the Divergence theorem together with the relevant vector identities are applied to (4.2), to obtain the following surface-volume representation:

$$\iint_S \mathbf{n} \times \mathbf{E} \partial S = - \iiint_V \frac{\partial \mathbf{B}}{\partial t} \partial V, \iint_S \mathbf{n} \times \mathbf{H} \partial S = \iiint_V \frac{\partial \mathbf{D}}{\partial t} \partial V + \iiint_V \mathbf{J} \partial V. \quad (4.3)$$

The continuous equation (4.3) is then approximated by the discrete form as follows:

$$\frac{\partial \mathbf{B}_p}{\partial t} = -\frac{1}{\Delta V} \sum_{F \in \zeta_p} \mathbf{n} \times \mathbf{E}_F \Delta S_F, \quad \frac{\partial \mathbf{D}_p}{\partial t} = \frac{1}{\Delta V} \sum_{F \in \zeta_p} \mathbf{n} \times \mathbf{H}_F \Delta S_F - \mathbf{J}_p, \quad (4.4)$$

where,  $\mathbf{n}$  is the unit outward normal through a face of a particular cell (see Figure 4.1). In the equations,  $\zeta_p$  is the set of faces that constitute the  $p^{th}$  cell in the computational domain.  $\Delta S_F$  and  $\Delta V$  are the surface area of a particular face in  $\zeta_p$  and the volume of the  $p^{th}$  cell, respectively. If  $\mathbf{E}_F$  and  $\mathbf{H}_F$  represent the values at the midpoint of the face, the above discrete surface integral approximation is second order in space. When all of the cells that constitute the mesh that describe the solution domain are visited, a system of ordinary differential equations (ODEs) results. Numerous methods are applied to resolve this ODE system.

Time discretisation can introduce either dispersion or dissipation errors (see [4]). Numerous techniques are utilised to resolve (4.4) into time discrete form. In [11] a number of approaches similar to the FD-TD technique have been investigated. For a function  $\phi$ , equations (4.5-4.6) represent the staggered (SLF) and unstaggered (ULF) leapfrog discretisations respectively. The SLF and ULF schemes are both  $O(\Delta t^2)$ :

$$\frac{\partial \phi^n}{\partial t} = \frac{\phi^{n+\frac{1}{2}} - \phi^{n-\frac{1}{2}}}{\Delta t}, \quad (4.5)$$

$$\frac{\partial \phi^n}{\partial t} = \frac{\phi^{n+1} - \phi^{n-1}}{2\Delta t}. \quad (4.6)$$

Methods using the discretisations in (5) have been used in the past to numerically solve for the electromagnetic fields governed by the Maxwell's equations. Using (4.5), (4.4) can be written in discrete form as:

$$\mathbf{H}_p^{n+\frac{1}{2}} = \mathbf{H}_p^{n-\frac{1}{2}} - \frac{\Delta t}{\mu_0 \Delta V} \sum_{F \in \zeta_p} \mathbf{n} \times (\mathbf{E}_F)^n \Delta S_F, \quad (4.7)$$

$$\mathbf{E}_p^{n+1} = \frac{2\varepsilon - \sigma\Delta t}{2\varepsilon + \sigma\Delta t} \mathbf{E}_p^n + \frac{2\Delta t}{(2\varepsilon + \sigma\Delta t)\Delta V} \sum_{F \in \zeta_p} \mathbf{n} \times (\mathbf{H}_F)^{n+\frac{1}{2}} \Delta S_F \quad (4.8)$$

Similarly, (4.4) for the ULF discretisation becomes:

$$\mathbf{H}_p^{n+1} = \mathbf{H}_p^{n-1} - \frac{2\Delta t}{\mu_0 \Delta V} \sum_{F \in \zeta_p} \mathbf{n} \times (\mathbf{E}_F)^n \Delta S_F \quad (4.9)$$

$$\mathbf{E}_p^{n+1} = \frac{\varepsilon - \sigma\Delta t}{\varepsilon + \sigma\Delta t} \mathbf{E}_p^{n-1} + \frac{2\Delta t}{(\varepsilon + \sigma\Delta t)\Delta V} \sum_{F \in \zeta_p} \mathbf{n} \times (\mathbf{H}_F)^n \Delta S_F \quad (4.10)$$

Equations (4.7-4.10) require the approximation to the electric and magnetic fields on the cell faces. It is possible to postulate a number of interpolation and extrapolation schemes to approximate these cell face unknowns. On structured grids, the simplest way to approximate the unknowns at a cell face is by averaging the values about a particular face. Such a technique yields a second order in space and time approximation to (4.7) to (4.10). These particular finite-volume methods will be referred to as SLF (4.7-4.8), staggered in time and unstaggered in space, and ULF (4.9-4.10), unstaggered in time and space Leapfrog discretisations.

At the  $p^{\text{th}}$  cell in (4.4), intensity vector splitting (IVS) [4] is applied to replace the  $\mathbf{n} \times \mathbf{E}_F$  and the  $\mathbf{n} \times \mathbf{H}_F$  terms. The idea of IVS is to include an extra term in the flux facial expression to dampen any numerical oscillations, and to capture any discontinuities (such as shocks and contact surfaces in CFD) in the solution. Intensity vector splitting originally from CFD, is based on the + and - characteristics to approximate the unknowns at a cell face. Equation (4.11-4.12) shows the general form at a cell face  $F$  of the IVS result:

$$\mathbf{n} \times \mathbf{E}_F = \frac{1}{2}\mathbf{n} \times (\mathbf{E}_F^+ + \mathbf{E}_F^-) + \frac{1}{2}\mathbf{n} \times \{[\mu c]^+ \mathbf{n} \times \mathbf{H}_F^+ - [\mu c]^- \mathbf{n} \times \mathbf{H}_F^-\}, \quad (4.11)$$

$$\mathbf{n} \times \mathbf{H}_F = \frac{1}{2}\mathbf{n} \times (\mathbf{H}_F^+ + \mathbf{H}_F^-) - \frac{1}{2}\mathbf{n} \times \{[\varepsilon c]^+ \mathbf{n} \times \mathbf{E}_F^+ - [\varepsilon c]^- \mathbf{n} \times \mathbf{E}_F^-\}, \quad (4.12)$$

where, the wave speed is given by  $c = 1/\sqrt{\mu\varepsilon}$ . Riemann invariants can also be applied to determine the left and right states at a cell face. The Riemann solver (RS) was introduced by Shankar [6]:

$$\mathbf{n} \times \mathbf{E}_F = \mathbf{n} \times \left\{ \frac{(\varepsilon c)_R}{(\varepsilon c)_R + (\varepsilon c)_L} \mathbf{E}_R + \frac{(\varepsilon c)_L}{(\varepsilon c)_R + (\varepsilon c)_L} \mathbf{E}_L \right\} + \mathbf{n} \times \frac{1}{(\varepsilon c)_R + (\varepsilon c)_L} \mathbf{n} \times \{ \mathbf{H}_R - \mathbf{H}_L \} \quad (4.13)$$

$$\mathbf{n} \times \mathbf{H}_F = \mathbf{n} \times \left\{ \frac{(\mu c)_R}{(\mu c)_R + (\mu c)_L} \mathbf{H}_R + \frac{(\mu c)_L}{(\mu c)_R + (\mu c)_L} \mathbf{H}_L \right\} - \mathbf{n} \times \frac{1}{(\mu c)_R + (\mu c)_L} \mathbf{n} \times \{ \mathbf{E}_R - \mathbf{E}_L \} \quad (4.14)$$

In free space, it can be shown that RS reduces to IVS. It is evident from IVS and RS that the + and - characteristics, or the right ( $R$ ) and left ( $L$ ) states must be approximated for each cell face. Note that IVS cannot be implemented with (4.7-4.8), since the values for the magnetic and electric fields are required at different time levels. Numerical experimentation has shown that IVS and RS with (4.9-4.10) incurs large errors due to the time discretisation [4]. Therefore, higher order time stepping methods are to be implemented. The following 3<sup>rd</sup> order Runge-Kutta (RK3) method is used for the numerical schemes discussed above:

$$\begin{aligned} \phi^{n+\frac{1}{3}} &= \phi^n + \frac{\Delta t}{3} \frac{\partial \phi^n}{\partial t}, \\ \phi^{n+\frac{2}{3}} &= \phi^n + \frac{2\Delta t}{3} \frac{\partial \phi^{n+\frac{1}{3}}}{\partial t}, \\ \phi^{n+1} &= \phi^n + \frac{\Delta t}{4} \left( 3 \frac{\partial \phi^{n+\frac{2}{3}}}{\partial t} + \frac{\partial \phi^n}{\partial t} \right). \end{aligned} \quad (4.15)$$

A 4<sup>th</sup> order Runge-Kutta (RK4) method is implemented also, and is formulated below:

$$\begin{aligned}
\hat{\phi}^{n+\frac{1}{2}} &= \phi^n + \frac{\Delta t}{2} \frac{\partial \phi^n}{\partial t}, \\
\tilde{\phi}^{n+\frac{1}{2}} &= \phi^n + \frac{\Delta t}{2} \frac{\partial \hat{\phi}^{n+\frac{1}{2}}}{\partial t}, \\
\bar{\phi}^{n+1} &= \phi^n + \Delta t \frac{\partial \tilde{\phi}^{n+\frac{1}{2}}}{\partial t}, \\
\phi^{n+1} &= \phi^n + \frac{\Delta t}{6} \left( \frac{\partial \phi^n}{\partial t} + 2 \frac{\partial \hat{\phi}^{n+\frac{1}{2}}}{\partial t} + 2 \frac{\partial \tilde{\phi}^{n+\frac{1}{2}}}{\partial t} + \frac{\partial \bar{\phi}^{n+1}}{\partial t} \right). \quad (4.16)
\end{aligned}$$

Substituting either of the IVS or RS results leads to numerical techniques referred to as RK3-IVS (RK3-RS) and RK4-IVS (RK4-RS), respectively. Note that (4.4) can be solved without the inclusion of damping, and this idea is pursued later in this section. Furthermore, other Runge-Kutta methods can be used to resolve the system of ODEs from above. These are not discussed here, but will be analysed in another paper where the schemes highlighted here will be applied on unstructured grids.

For simplicity, Figure 4.1 illustrates a typical cell within a 3D-structured computational domain. As depicted, the + and – characteristics for IVS, and

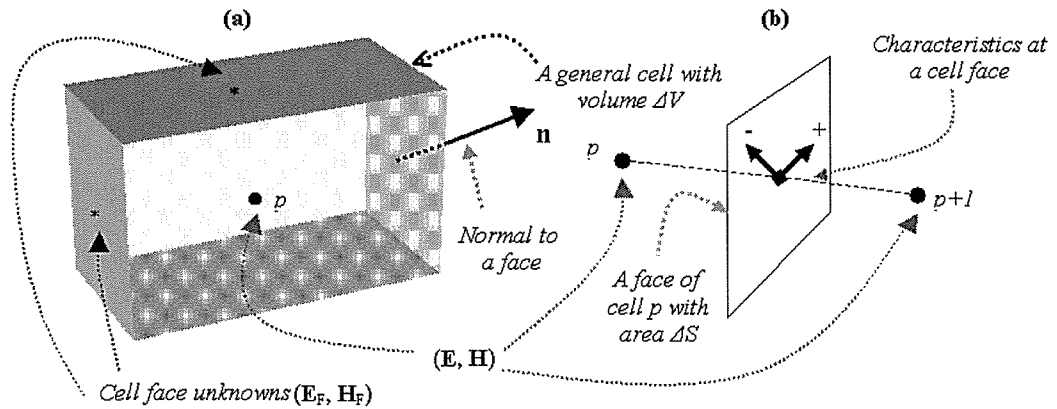


Figure 4.1: A general cell within the computational domain; (a) 3D cell with unknown locations; (b) The characteristics at a face of a particular cell.

the right and left states for RS are required on a particular cell face and different strategies can be derived to approximate the values at the cell face joining any two adjacent cells. For example, an unknown  $\xi$  can be approximated using the  $0^{th}$  order substitution:

$$\xi_{p+\frac{1}{2}}^- = \xi_p, \quad \xi_{p+\frac{1}{2}}^+ = \xi_{p+1}. \quad (4.17)$$

Imposing the  $0^{th}$  order approximation in RK3/RK4-IVS/RS leads to two first order in space and  $3^{rd}$  order in time approximations known as RK3-1-IVS and RK3-1-RS, and two first order in space and  $4^{th}$  order in time approximations identified as RK4-1-IVS and RK4-1-IVS. For a structured uniform mesh, it is possible to derive a general one-sided linear extrapolation model that is  $2^{nd}$  order in space:

$$\xi_{p+\frac{1}{2}}^- = \frac{1}{2}(3\xi_p - \xi_{p-1}), \quad \xi_{p+\frac{1}{2}}^+ = \frac{1}{2}(3\xi_{p+1} - \xi_{p+2}). \quad (4.18)$$

As for the  $0^{th}$  order extrapolations, using (4.18) the equivalent  $3^{rd}$  and  $4^{th}$  order in time and  $2^{nd}$  order in space numerical schemes are called RK3-2L-IVS/RS and RK4-2L-IVS/RS, respectively. It is important to note that (4.18) is developed for uniform in  $x$ ,  $y$  and  $z$  coordinate structured grids. Such extrapolations are complicated to implement on unstructured meshes, and are demonstrated only to assess the errors between the different schemes.

Given discrete data points, it is also possible to find least squares gradient approximations at cell centres [12]. Eq. (4.19) expresses a truncated representation of the Taylor series:

$$\delta\mathbf{r} \cdot \nabla \xi(\mathbf{r}) \approx \xi(\mathbf{r} + \delta\mathbf{r}) - \xi(\mathbf{r}). \quad (4.19)$$

The above system can be cast into matrix form as  $\mathbf{A} \cdot \nabla \xi_p = \mathbf{d}$ . The gradient that minimises  $\|\mathbf{A} \cdot \xi_p - \mathbf{d}\|^2$  with respect to the inner product on  $\mathbb{R}^k$  can be

obtained by solving the normal equations. The value of  $k$  equals the number of neighbouring nodes utilised to obtain the gradient at the  $p^{th}$  cell. Although approximations for the gradients that utilise the hypercube ( $k = 26$ ) have been investigated, in this paper the gradients were constructed using only adjacent cells of  $\zeta_p$  (*i.e.*  $k = 6$ ). Hence by evaluating (4.19), the gradients of the fields are used to approximate the characteristics at the cell faces. Accordingly, (4.20) provides a  $2^{nd}$  order approximation for the + and - fields, or the right and left states and the subsequent methods are classified as RK3-2G-IVS, RK4-2G-IVS, RK3-2G-RS and RK4-2G-RS, depending on the time integration and whether intensity vector splitting or the Riemann solver is applied:

$$\xi_{p+\frac{1}{2}}^- = \xi_p + \delta' \cdot \nabla \xi_p, \quad \xi_{p+\frac{1}{2}}^+ = \xi_{p+1} + \delta'' \cdot \nabla \xi_{p+1}. \quad (4.20)$$

In (4.20),  $\delta'$  and  $\delta''$  are the vectors from the nodes  $(p)$  to  $(p + \frac{1}{2})$  and  $(p + 1)$  to  $(p + \frac{1}{2})$ , respectively (see Figure 4.1). Also, the gradients can be approximated using the Gauss-Green reconstruction [12]:

$$\nabla \xi_p \approx \frac{1}{V_p} \sum_{F \in \zeta_p} \mathbf{n} \xi_F,$$

where,  $V_p$  is the volume of the  $p^{th}$  cell and  $\mathbf{n}$  is the unit outward normal to face  $F$ . On structured grids, when the Gauss-Green reconstruction is used to approximate the values of characteristics at the cell faces in RK3/RK4-IVS and RK3/RK4-RS, the resulting equations reduce to that obtained by the least squares gradients (4.19).

The RK3/RK4-2L-IVS/RS and RK3/RK4-2G-IVS/RS methods can also be applied without flux splitting (*i.e.* IVS and RS). These techniques will be referred to as the RK3/RK4-2L and RK3/RK4-2G schemes, which are the linear extrapolation and the spatial gradient approximations without intensity vector splitting and Riemann invariants, respectively.

## 4.3 Implementation of Boundary Conditions

In this section, the perfectly conducting wall, incident field, material interface and absorbing boundary conditions are treated. On a perfectly conducting wall in a microwave heating apparatus, the following conditions need to be satisfied [13]:

$$\mathbf{n} \times \mathbf{E} = 0, \quad \mathbf{n} \cdot \mathbf{H} = 0. \quad (4.21)$$

Equation (4.21) makes the assumption that there is no loss through the perfect conductor. If there is some loss associated with the conducting wall boundaries, then impedance conditions should be used instead of (4.21). Figure 4.2 shows the characteristics in the proximity of a perfectly conducting wall. It can be seen from the figure, that at the wall, only one of the characteristics exists. For the numerical treatment of the conducting wall boundary condition, a spurious external layer surrounding the whole computational domain is introduced, as shown in Figure 4.2. The numerically simulated boundary information of (4.22-4.23) is constructed in a way that ensures the conditions of (4.21) are enforced at the cell faces that lie on the conducting wall. Hence, the following spurious fields are constructed:

$$(\mathbf{E}_0^*)_t = -(\mathbf{E}_1)_t, \quad (\mathbf{E}_0^*)_n = (\mathbf{E}_1)_n, \quad (4.22)$$

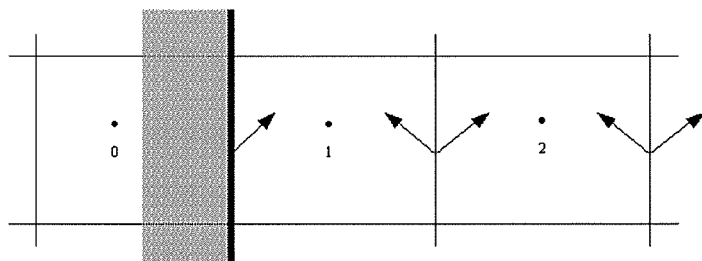


Figure 4.2: Boundary condition treatment at a Perfectly Conducting Wall.

$$(\mathbf{H}_0^*)_t = (\mathbf{H}_1)_t, \quad (\mathbf{H}_0^*)_n = -(\mathbf{H}_1)_n. \quad (4.23)$$

where, \* represents the fields introduced externally to the original domain to satisfy the boundary conditions (4.21), when the standard discrete in space Maxwell's equations (4.4) are used on the perfectly conducting boundary. For the spurious field evaluations,  $t$  and  $n$  are the tangential and normal components of the electric and magnetic fields, respectively. The conditions (4.22-4.23) are used in the ULF, SLF, RK3/RK4-2G and RK3/RK4-1-IVS/RS simulations. For the RK3/RK4-2L with and without IVS/RS, a secondary layer is introduced for the extrapolations. For the second order linear extrapolation models, (4.24-4.25) has to be implemented together with (4.22-4.23):

$$(\mathbf{E}_{-1}^*)_t = -(\mathbf{E}_2)_t, \quad (\mathbf{E}_{-1}^*)_n = (\mathbf{E}_2)_n, \quad (4.24)$$

$$(\mathbf{H}_{-1}^*)_t = (\mathbf{H}_2)_t, \quad (\mathbf{H}_{-1}^*)_n = -(\mathbf{H}_2)_n. \quad (4.25)$$

Techniques such as RK3/RK4-2G-IVS/RS that employ the gradients for the approximations at the cell faces require (4.24-4.25) together with the following spurious field conditions to be satisfied:

$$(\nabla \mathbf{E}_0^*)_t = -(\nabla \mathbf{E}_1)_t, \quad (\nabla \mathbf{E}_0^*)_n = (\nabla \mathbf{E}_1)_n, \quad (4.26)$$

$$(\nabla \mathbf{H}_0^*)_t = (\nabla \mathbf{H}_1)_t, \quad (\nabla \mathbf{H}_0^*)_n = -(\nabla \mathbf{H}_1)_n. \quad (4.27)$$

Equation (4.26-4.27) is necessary in the boundary information evaluation for schemes that obtain the facial values according to (4.20), since it satisfies (4.21) at a cell face that lies on a perfectly conducting wall boundary. Given the above formulations, the boundary conditions on a perfectly conducting wall are guaranteed in (4.4) according to (4.21). Similarly, other discrete conditions can be

developed that provide continuity of the tangential magnetic fields and ensure zero tangential electric fields at a perfectly conducting wall, but these are not discussed here.

A classical waveguide is demonstrated in Figure 4.3. In the figure,  $S$  and  $F$  represent the scattered and full field regions inside a waveguide, respectively. Typically, a fictitious dielectric is introduced inside the scattered region to absorb any reflected backward travelling waves.

Figure 4.4 illustrates the situation arising at the incident plane, where the electromagnetic fields are excited. It is assumed that  $z_0$  represents the location where the incident field is applied.  $T$ ,  $S$  and  $I$  are the total, scattered and incident field classifications, respectively. In the full field region of the waveguide the total fields have to be computed, while in the scattered field region only the scattered fields are computed. Across an input plane this is achieved by adding the incident field to the scattered field in  $F$ , and subtracting the incident field from the total field in  $S$  (see Figure 4.4). This is sufficient to propagate a wave in the  $z$ -coordinate direction. In this paper, a continuous  $TE_{10}$  incident field has

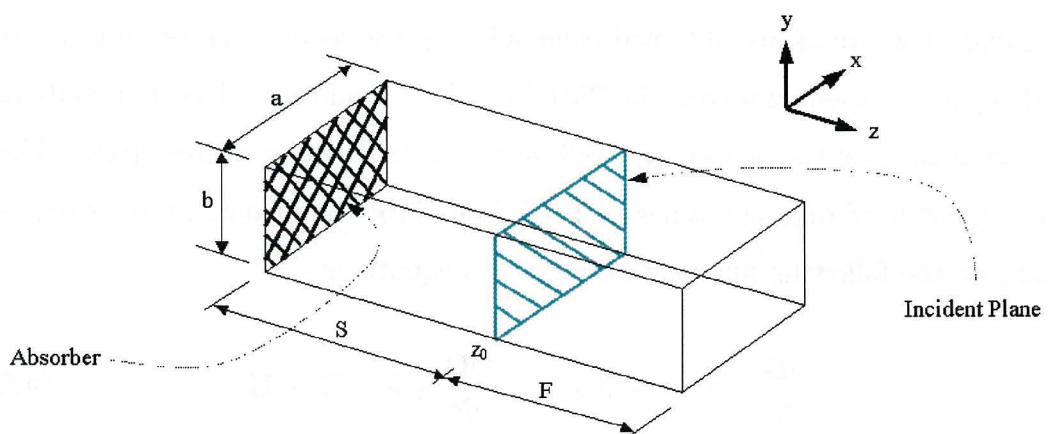


Figure 4.3: A waveguide with incident and absorbing boundary conditions.

been implemented for the input boundary condition. At the input plane, the scattered and full fields were computed according to the following expressions:

$$E_y^I = E_0 \sin\left(\frac{\pi x}{a}\right) \cos(\omega t - \beta_0 z_0), \quad (4.28)$$

$$H_x^I = -\frac{\beta_0}{\omega \mu_0} E_0 \sin\left(\frac{\pi x}{a}\right) \cos(\omega t - \beta_0 z_0), \quad (4.29)$$

$$H_z^I = -\frac{\pi}{\omega \mu_0 a} E_0 \cos\left(\frac{\pi x}{a}\right) \sin(\omega t - \beta_0 z_0), \quad (4.30)$$

$$E_0 = 2 \sqrt{\frac{P_0}{ab\varepsilon_0}}, \quad \beta_0 = \sqrt{\omega^2 \mu_0 \varepsilon_0 - \left(\frac{\pi}{a}\right)^2}.$$

In (4.28-4.30),  $P_0$  is the average input power, and  $a$  and  $b$  are the dimensions as labelled in Figure 4.3. Figure 4.3 also illustrates an absorbing boundary layer. There are two main types of absorbers, the MUR type absorbing boundary condition [14] and the Perfectly Matched Layer (PML) [9, 15, 16]. The 1<sup>st</sup> order MUR type boundary condition is given as:

$$\left[ \left( \frac{\partial}{\partial z} - \frac{1}{c} \frac{\partial}{\partial t} \right) \phi \right]_{z=0} = 0, \quad (4.31)$$

where,  $c$  is the wavefront speed inside the waveguide. In the past, this boundary condition has been widely implemented in the FD-TD scheme. In this paper, it is employed in the FD-TD and ULF numerical simulations. While MUR type boundary conditions are obtained from splitting the wave equation into positive and negative travelling waves, the PML boundary condition is based on matching the impedance of the absorbing medium to the impedance of free-space. There are a number of different types of PML boundary conditions, all of which are based on the following augmented Maxwell's equations:

$$\frac{\partial \mathbf{B}}{\partial t} + \mathbf{J}^* = -\nabla \times \mathbf{E}, \quad \frac{\partial \mathbf{D}}{\partial t} + \mathbf{J} = \nabla \times \mathbf{H}, \quad (4.32)$$

where,

$$\mathbf{J}^* = \sigma^* \mathbf{H}, \quad \sigma^* = \frac{\mu_0}{\varepsilon_0} \sigma. \quad (4.33)$$

The Berenger type PML [16] absorber splits some of the components of the fields inside the absorption layer. Such a methodology increases memory usage and is also more computationally exhaustive, as opposed to more recent PML absorbers that do not split the fields [9]. If (4.33) is satisfied for the absorbing boundary condition, then the impedance of the PML equals that of free-space, and no reflections occur. Now, (4.1) can be replaced by (4.32) in the discretisation, and new discrete in space equations can be obtained for the simulation of Maxwell's equations within the absorbing material:

$$\frac{\partial \mathbf{B}}{\partial t} = -\frac{1}{\Delta V} \sum_F \mathbf{n} \times \mathbf{E}_F \Delta S_F - \mathbf{J}_p^*, \quad \frac{\partial \mathbf{D}}{\partial t} = \frac{1}{\Delta V} \sum_F \mathbf{n} \times \mathbf{H}_F \Delta S_F - \mathbf{J}_p. \quad (4.34)$$

For the schemes discussed in this paper, (4.34) is implemented using a new cell-centred adaptation of the Petropoulos PML boundary condition [9]. For the absorbing boundary region, only the normal components need to be treated in (4.34). The tangential components are still governed by (4.4). Consequently, (4.34) can be discretised and formulated with and without IVS/RS.

In the theory by Petropoulos, an extra term in the evaluations of the normal components inside the PML region has to be approximated. This extra term consists of an integral from time zero to the current time step of the numerical solver. The approximation of this time integral has to be carefully treated, so that the time stepping of the numerical solver is consistent with the computation of the time integral. Hence, the step size in the numerical integration must coincide with the time marching of the discrete Maxwell's equations solver (4.34). The update for the numerical integration is therefore a sum, which is accumulated according to the time resolution of (4.34). The PML formulation for the SLF technique is similar to that discussed in [9], the only difference being in the location of the spatial unknowns. The SLF implementation for the normal component at a point  $p$  of (for example) the magnetic field is formulated from (4.34) as follows:

$$\Delta V \left( \frac{\partial \mathbf{B}}{\partial t} \right)_p = - \sum_{F \in \zeta_p} (\mathbf{n} \times \mathbf{E}_F) \Delta S_F - \frac{\sigma^*}{\mu_0} \int_0^t \iint_S (\mathbf{n} \times \mathbf{E}_F) \partial S dt, \quad (4.35)$$

$$\Delta V \left( \frac{\partial \mathbf{B}}{\partial t} \right)_p = - \sum_{F \in \zeta_p} (\mathbf{n} \times \mathbf{E}_F) \Delta S_F - I, \quad (4.36)$$

where,

$$I = \frac{\sigma^*}{\mu_0} \int_0^t \sum_{F \in \zeta_p} (\mathbf{n} \times \mathbf{E}_F) \Delta S_F dt = \frac{\sigma^*}{\mu_0} \int_0^{n\Delta t} \sum_{F \in \zeta_p} (\mathbf{n} \times \mathbf{E}_F) \Delta S_F d\tau. \quad (4.37)$$

In (4.35-4.37), the integral has to be approximated using numerical integration techniques. For the SLF method, the components of the electric and magnetic fields are located at the  $n^{th}$  and the  $(n + \frac{1}{2})^{th}$  time levels. The numerical integration that approximates (4.37) has to ensure that the scheme updates the integral at every  $\frac{1}{2}$  time steps. For this reason, the numerical integration is performed using a two increment trapezoidal rule. Given that at time zero the electric and magnetic fields are zero, then (4.37) can be approximated as:

$$I = \frac{\sigma^*}{\mu_0} \Delta t \sum_{m=0}^{n-1} \left[ \sum_{F \in \zeta_p} (\mathbf{n} \times \mathbf{E}_F)^m \Delta S_F \right] + \frac{\sigma^*}{2\mu_0} \Delta t \sum_{F \in \zeta_p} (\mathbf{n} \times \mathbf{E}_F)^n \Delta S_F. \quad (4.38)$$

The following expression is obtained when (4.38) is substituted back into (4.37) and resolved using SLF (4.5):

$$\mathbf{H}_p^{n+\frac{1}{2}} = \mathbf{H}_p^{n-\frac{1}{2}} - \left( \frac{2\mu_0 \Delta t + \sigma^* \Delta t^2}{2\mu_0^2 \Delta V} \right) \sum_{F \in \zeta_p} (\mathbf{n} \times \mathbf{E}_F)^n \Delta S_F - \frac{\sigma^* \Delta t^2}{\mu_0^2 \Delta V} \mathbf{F}_p^{n-1}, \quad (4.39)$$

$$\mathbf{F}_p^n = \mathbf{F}_p^{n-1} + \sum_{F \in \zeta_p} (\mathbf{n} \times \mathbf{E}_F)^n \Delta S_F. \quad (4.40)$$

Similarly, the normal component of the electric field within the PML region is defined as:

$$\mathbf{E}_p^{n+1} = \mathbf{E}_p^n + \left( \frac{2\varepsilon\Delta t + \sigma\Delta t^2}{2\varepsilon^2\Delta V} \right) \sum_{F \in \zeta_p} (\mathbf{n} \times \mathbf{H}_F)^{n+\frac{1}{2}} + \frac{\sigma\Delta t^2}{\varepsilon^2\Delta V} \mathbf{G}_p^{n-\frac{1}{2}}, \quad (4.41)$$

$$\mathbf{G}_p^{n+\frac{1}{2}} = \mathbf{G}_p^{n-\frac{1}{2}} + \sum_{F \in \zeta_p} (\mathbf{n} \times \mathbf{H}_F)^{n+\frac{1}{2}} \Delta S_F. \quad (4.42)$$

The following equations are generated for the 3<sup>rd</sup> order ODE solver, when the above theory is reformulated to cater for the RK time integrations:

$$\left( \frac{\partial \mathbf{H}_p}{\partial t} \right)^n = - \left( \frac{\sigma^*\Delta t + 6\mu_0}{6\mu_0^2\Delta V} \right) \sum_{F \in \zeta_p} (\mathbf{n} \times \mathbf{E}_F)^n \Delta S_F - \frac{\sigma^*\Delta t}{3\mu_0^2\Delta V} \mathbf{F}_p^{n-1}, \quad (4.43)$$

$$\left( \frac{\partial \mathbf{E}_p}{\partial t} \right)^n = \left( \frac{\sigma\Delta t + 6\varepsilon_0}{6\varepsilon_0^2\Delta V} \right) \sum_{F \in \zeta_p} (\mathbf{n} \times \mathbf{H}_F)^n \Delta S_F + \frac{\sigma\Delta t}{3\varepsilon_0^2\Delta V} \mathbf{G}_p^{n-1}, \quad (4.44)$$

where,

$$\mathbf{F}_p^n = \mathbf{F}_p^{n-1} + \sum_{F \in \zeta_p} (\mathbf{n} \times \mathbf{E}_F)^{n-\frac{2}{3}} \Delta S_F + \sum_{F \in \zeta_p} (\mathbf{n} \times \mathbf{E}_F)^{n-\frac{1}{3}} \Delta S_F + \sum_{F \in \zeta_p} (\mathbf{n} \times \mathbf{E}_F)^n \Delta S_F, \quad (4.45)$$

$$\mathbf{G}_p^n = \mathbf{G}_p^{n-1} + \sum_{F \in \zeta_p} (\mathbf{n} \times \mathbf{H}_F)^{n-\frac{2}{3}} \Delta S_F + \sum_{F \in \zeta_p} (\mathbf{n} \times \mathbf{H}_F)^{n-\frac{1}{3}} \Delta S_F + \sum_{F \in \zeta_p} (\mathbf{n} \times \mathbf{H}_F)^n \Delta S_F. \quad (4.46)$$

For the 4<sup>th</sup> order Runge-Kutta method, the normal equations inside the PML are treated by the following discretisations:

$$\left( \frac{\partial \mathbf{H}_p}{\partial t} \right)^n = - \left( \frac{\sigma^*\Delta t + 4\mu_0}{4\mu_0^2\Delta V} \right) \sum_{F \in \zeta_p} (\mathbf{n} \times \mathbf{E}_F)^n \Delta S_F - \frac{\sigma^*\Delta t}{2\mu_0^2\Delta V} \mathbf{F}_p^{n-1}, \quad (4.47)$$

$$\left( \frac{\partial \mathbf{E}_p}{\partial t} \right)^n = \left( \frac{\sigma\Delta t + 4\varepsilon_0}{4\varepsilon_0^2\Delta V} \right) \sum_{F \in \zeta_p} (\mathbf{n} \times \mathbf{H}_F)^n \Delta S_F + \frac{\sigma\Delta t}{2\varepsilon_0^2\Delta V} \mathbf{G}_p^{n-1}, \quad (4.48)$$

where,

$$\mathbf{F}_p^n = \mathbf{F}_p^{n-1} + \sum_{F \in \zeta_p} (\mathbf{n} \times \mathbf{E}_F)^{n-\frac{1}{2}} \Delta S_F + \sum_{F \in \zeta_p} (\mathbf{n} \times \mathbf{E}_F)^n \Delta S_F, \quad (4.49)$$

$$\mathbf{G}_p^n = \mathbf{G}_p^{n-1} + \sum_{F \in \zeta_p} (\mathbf{n} \times \mathbf{H}_F)^{n-\frac{1}{2}} \Delta S_F + \sum_{F \in \zeta_p} (\mathbf{n} \times \mathbf{H}_F)^n \Delta S_F. \quad (4.50)$$

For the different time levels of the RK3 solver, (4.45-4.46) are updated at the  $n^{th}$ ,  $(n + \frac{1}{3})^{th}$  and  $(n + \frac{2}{3})^{th}$  time levels, while for the RK4 solver, (4.49-4.50) are determined at the  $n^{th}$  and the  $(n + \frac{1}{2})^{th}$  time levels. For the Petropoulos approximation within the PML region, the  $\mathbf{F}$  and  $\mathbf{G}$  terms are obtained using a trapezoidal integration. The number of steps taken to update the equations of (4.45-4.46) and (4.49-4.50) depends on the number of time levels for which the time integration is considered (see equation (4.15-4.16)).

Figure 4.5 depicts an interface between free-space and a material inside a waveguide. To treat and propagate an electromagnetic wave across an interface in Figure 4.5, the following conditions have to be satisfied across a material

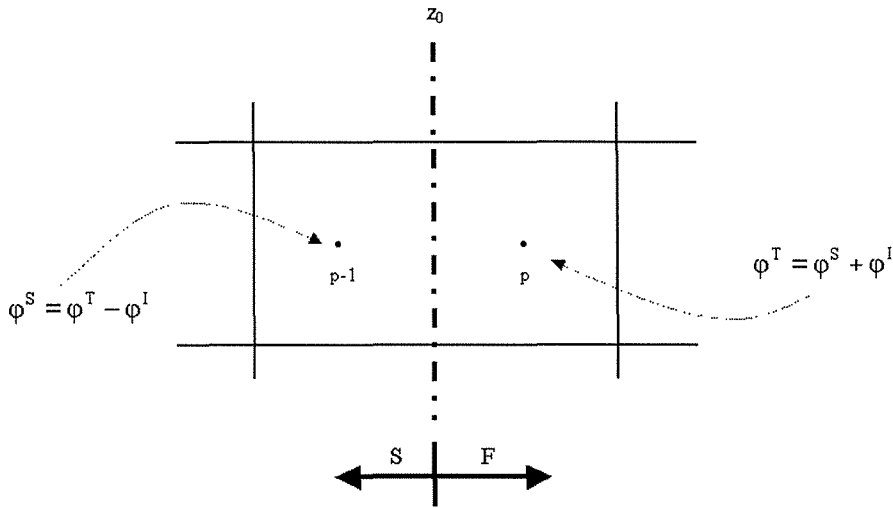


Figure 4.4: The 2D Input Plane implementation.

boundary:

$$\mathbf{n} \times (\mathbf{E}_2 - \mathbf{E}_1) = \mathbf{0}, \quad (4.51)$$

$$\mathbf{n} \cdot (\varepsilon_2 \mathbf{E}_2 - \varepsilon_1 \mathbf{E}_1) = 0, \quad (4.52)$$

$$\mathbf{n} \times (\mathbf{H}_2 - \mathbf{H}_1) = \mathbf{0}, \quad (4.53)$$

$$\mathbf{n} \cdot (\mathbf{H}_2 - \mathbf{H}_1) = 0. \quad (4.54)$$

On Cartesian grids, (4.51) and (4.53) imply that the tangential fields across a material interface have to be equal. Equation (4.51-4.54) assumes that the permeability of the different materials across an interface is constant. In the past, schemes that utilise IVS/RS were developed to capture any discontinuities across such interfaces.

It is well known that discontinuities can occur in the derivatives of the electromagnetic fields across a material interface. According to [17], plane wave assumptions can be made to capture the solution more accurately across a material interface in the FD-TD scheme. The plane wave assumption at an interface proposed by Zhao is adapted for particular ccFV-TD schemes, and the theory is demonstrated via a simplified Taylor expansion:

$$\xi_{p+1} = \xi_{p+\frac{1}{2}}^+ + \delta_x \left( \frac{\partial \xi}{\partial x} \right)_{p+\frac{1}{2}}^+ + O(\delta_x^2), \quad \xi_p = \xi_{p+\frac{1}{2}}^- - \delta_x \left( \frac{\partial \xi}{\partial x} \right)_{p+\frac{1}{2}}^- + O(\delta_x^2), \quad (4.55)$$

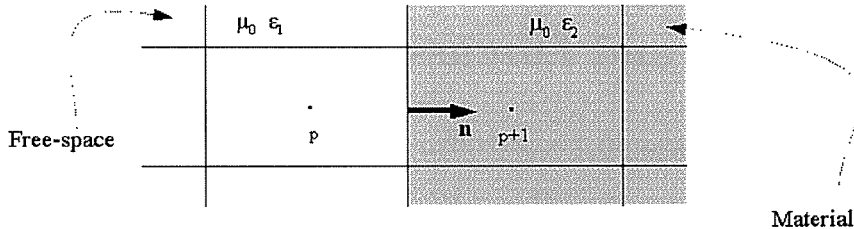


Figure 4.5: Free-space and material interface boundary.

where,  $\delta_x$  on a structured uniform grid is the distance from any cell-centre to any face. Assuming that the waves near an interface behave in a plane wave manner, the following condition has to be satisfied at a material interface [17]:

$$\frac{1}{\beta_2} \left( \frac{\partial \xi}{\partial x} \right)_{p+\frac{1}{2}}^+ = \frac{1}{\beta_1} \left( \frac{\partial \xi}{\partial x} \right)_{p+\frac{1}{2}}^- . \quad (4.56)$$

The  $(p + \frac{1}{2})$  spatial location can be thought of as the material interface, and then by substituting (4.56) into (4.55), the following approximation at a dielectric interface is obtained:

$$\xi_{p+\frac{1}{2}} = \frac{\beta_2}{\beta_1 + \beta_2} \xi_p + \frac{\beta_1}{\beta_1 + \beta_2} \xi_{p+1} + O(\delta_x^2), \quad (4.57)$$

$$\beta_i \propto \sqrt{\epsilon'_i \left( 1 + \sqrt{1 + \left( \frac{\epsilon''_i}{\epsilon'_i} \right)^2} \right)}, \quad i = 1, 2.$$

Generally,  $\beta_1$  is associated with the properties of free space and  $\beta_2$  is associated with the properties of the dielectric material. Equation (4.57) can be shown to be a second order approximation to the facial values at the interface. This technique is applied in the SLF, RK3-2G and RK4-2G approximations to propagate the numerical estimates across a dielectric boundary. Note that if  $\beta_1 = \beta_2$ , as is the case for free space cell faces, (4.57) is equivalent to averaging  $\xi_p$  and  $\xi_{p+1}$  to obtain the required facial value. Consequently, (4.57) can be employed everywhere within the ccFV-TD solver to estimate values at the cell faces.

## 4.4 Results and Discussion

A waveguide of dimension  $0.1\text{ m} \times 0.05\text{ m} \times 0.4\text{ m}$  was excited using a  $TE_{10}$  wave, with an average input power of  $P_0 = 1\text{ W}$ . The ccFV-TD solvers established in the previous sections were used to simulate the electromagnetic wave phenomenon for fourteen periods, and fields for the last two periods were averaged and illustrated

graphically. The incident field has been smoothed according to the following Gaussian pulse to remove any rapid changes in the introduction of the  $TE_{10}$  fields [17]:

$$gauss(t) = \begin{cases} e^{-(\frac{t}{T}-3)^2} & t \leq 3T \\ 1 & t > 3T \end{cases}. \quad (4.58)$$

In (4.58),  $T$  represents the wave period inside the waveguide. In all of the studies, the time stepping of the numerical solver was constrained by the following relationship:

$$\Delta t = \frac{0.9}{c_{max} \sqrt{\frac{1}{\delta_x^2} + \frac{1}{\delta_y^2} + \frac{1}{\delta_z^2}}}, \quad (4.59)$$

where,  $c_{max}$  is the maximum wave speed expected in the waveguide, and  $\delta_x$ ,  $\delta_y$  and  $\delta_z$  are the minimum mesh dimensions in the  $x$ ,  $y$  and  $z$  coordinate directions. The domain of the waveguide was discretised into 96000 ( $40 \times 20 \times 120$ ) Cartesian cells. In Table 4.2 the components together with their acronyms for each numerical solver investigated throughout this section are summarised.

For the empty waveguide study, the instantaneous electromagnetic fields were monitored over a number of periods. The fields were compared to the exact solution. From the comparison, the phase difference was approximated using a least squares technique. Given the exact solution, it was assumed that the computed fields had some phase error associated with them. Using this assumption, the exact solution was formulated using a phase angle relation:

$$E_C = E_0 \cos(\omega t + \beta z + \theta), \quad (4.60)$$

where,  $E_C$  is the computed field value at a particular point in space and after some number of time steps.  $E_0$  is the exact electric field amplitude, and  $\theta$  is the phase error.  $\beta$  and  $z$  are dependent on the microwave heating apparatus.

Acronym	Definition
FD-TD	Finite-Difference Time-Domain Method with beta correction at an interface and MUR type absorbing layer
ULF	Unstaggered in time and centred in space Leapfrog method with MUR type absorber
SLF	Staggered in time and centred in space Leapfrog method with Petropoulos type PML absorbing layer
Beta	Any method that utilises beta correction at an interface between free-space and material
1	One sided 1st order in space extrapolation to approximate cell face unknowns
2L	One sided 2nd order in space linear extrapolation is used in the numerical solver
2G	The gradients are calculated and used via the Taylor series to approximate the values at a cell face
RK3	Time marching was performed using the 3rd order Runge Kutta method and Petropoulos type absorbing layer is used to absorb the waves in the scattered region of the waveguide
RK4	The ODEs in time were approximated via the 4th order Runge Kutta scheme and Petropoulos type absorber is used for the absorbing boundary condition
RS	The Riemann Solver equations were used to replace the terms at a cell face
IVS	Intensity-Vector Splitting was used to dampen any oscillatory behaviour in the numerical solutions
Int or Interface	Case of IVS, where IVS was applied only at a material interface
Not Int or Not Interface	IVS was applied everywhere inside the computational domain, except at a material interface
Mat or Material	IVS was applied inside the domain of the material, and not anywhere else

Table 4.2: The definitions of the numerous numerical schemes that are exhibited.

At a point in space, the values were computed for a period of the microwave, and the phase error was approximated using a least squares technique. Once the phase angle between the computed and analytic solutions was established, the amplitude error evident in the schemes was estimated using the standard norms. The results for the different schemes are outlined in Table 4.3. It should be noted that due to the implementation of the smoothing of (4.58), the results obtained from the simulations performed much better than expected. At the input plane if no smoothing was applied, then the FD-TD method clearly outperformed the ccFV-TD schemes. The schemes when implemented without smoothing had a tendency to oscillate around the analytic solution. The reason for this is that initially all fields are zero and the electromagnetic waves without (4.58) are not introduced into the apparatus in a smooth manner, but rather as a step function from which numerical noise tends to be generated in the approximations. At a node  $p$ , the time averaged solutions in the figures were obtained according to the expression:

$$(E_{av})_p = \frac{1}{N} \sum_{i=1}^N (|E_x(i\Delta t)|_p + |E_y(i\Delta t)|_p + |E_z(i\Delta t)|_p). \quad (4.61)$$

For a  $TE_{10}$  empty waveguide, the  $E_x$  and  $E_z$  fields are zero, therefore for all nodes, (4.61) reduces to a time averaged  $E_y$  field:

$$(E_y)_{av} = \frac{1}{N} \sum_{i=1}^N |E_y(i\Delta t)|. \quad (4.62)$$

In free-space, the RS scheme reduces to the IVS scheme, and hence in this case study, references will be made only to the IVS simulations.

It is important to note that during the numerical simulations, not all of the  $E_x$ ,  $E_z$  and  $H_y$  fields were zero, as expected for an empty  $TE_{10}$  waveguide. It was found that the schemes that utilise the IVS strategy produced a slight error of 0.1 % in these fields. This error was thought to be a side effect of the implemen-

SCHEME	AMPLITUDE ERROR			PHASE ERROR		CPU TIME
	1-Norm	2-Norm	inf-Norm	Mean	Variance	Normalised
FD-TD	0.0741637	0.0694287	0.0672323	0.6818206	0.0008836	0.0666667
SLF	0.0681339	0.0643379	0.0643557	0.6784976	0.0007899	0.0797814
RK4-2L	0.0672170	0.0620855	0.0550679	0.7249154	0.0008259	0.6464480
RK3-2G	0.0647705	0.0624504	0.0660729	0.4855492	0.0007476	0.4557377
RK4-2G	0.0647643	0.0624570	0.0662543	0.4855753	0.0007509	0.6289617
RK3-1-IVS	0.0892745	0.1024925	0.1375204	0.5302919	0.0007921	0.6420765
RK4-1-IVS	0.0892570	0.1024751	0.1374970	0.5303072	0.0007920	0.8715847
RK3-2G-IVS	0.0879133	0.1015108	0.1274249	0.6106417	0.0006905	0.7404371
RK4-2G-IVS	0.0879282	0.1015241	0.1274409	0.6106659	0.0006905	1.0000000

Table 4.3: Analysis of the different ccFV-TD methods. Instantaneous amplitude and phase errors are illustrated for an empty waveguide.

tation of damping, and regarded as negligible in comparison with the  $E_y$  field. In fact, the use of (4.61) instead of (4.62) to compute the time averaged fields revealed no significant change in the graphs. From Table 4.3, it can be seen that the methods that utilise IVS tend to have larger amplitude errors. This is due to the fact that the CFD type algorithms dampen any oscillatory behaviour, and through this process the amplitude of the wave is somewhat reduced also. It is observed that RK4-1-IVS incurs large dissipation errors in the amplitude of the wave (see Figure 4.6(d)). This is due to the lower order spatial discretisation utilised. It is seen from Figures 4.7(c-d) that the introduction of IVS reduces the amplitude of the wave. It is not evident in the full field region of the guide, but can be clearly seen in the scattered field region, when compared to RK4-2G. There appears to be no obvious difference between RK3 and RK4 time integration techniques for the empty waveguide study. This is observed in Table 4.3 and Figures 4.7(a-b).

The phase errors in Table 4.3 are of less significance for microwave heating

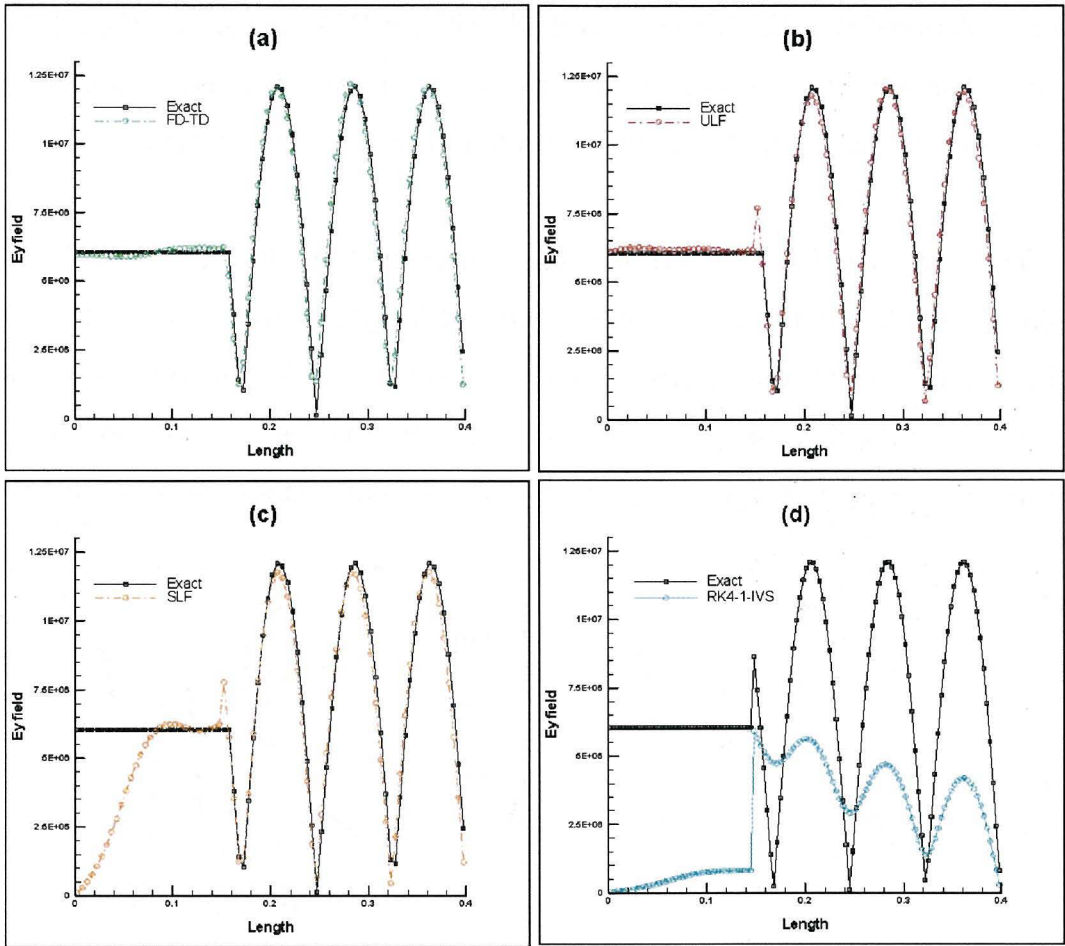


Figure 4.6: A fourteen period time averaged continuous  $TE_{10}$  wave inside a waveguide; (a)FD-TD; (b) ULF; (c) SLF; (d) RK4-1-IVS.

purposes. Phase errors are related to the speed at which the wave travels along the waveguide. The observed differences in phase are of the order of nanoseconds in time, and hence, when numerically computing electromagnetic waves for the purpose of microwave heating, nanosecond shifts in the solutions are of little importance. Although, the phase analysis does provide a good estimate of the accuracy of the different ccFV-TD schemes. It should be noted that the values in Table 4.3 were calculated after two periods. Numerical error can be cumulative in nature, and hence, the clear distinctions between the observed and the calculated values (*eg.* RK4-1-IVS in Table 4.3 and Figure 4.6(d)). From the table it

can be observed that the RK type methods without IVS can capture the solution better than any other scheme highlighted here. Though, it must be noted that this study does not reflect the situation when there is a material present.

The Leapfrog time integration numerical simulations illustrated in Figures 4.6(a-c) are observed to be performing well, although, it can be shown that the ULF scheme (see Figure 4.6(b)) is conditionally unstable [4]. Since the ULF scheme was found to unstable when an object was present, it will not be discussed hereafter. In Figures 4.6(a) and 4.6(c) the only difference is the location

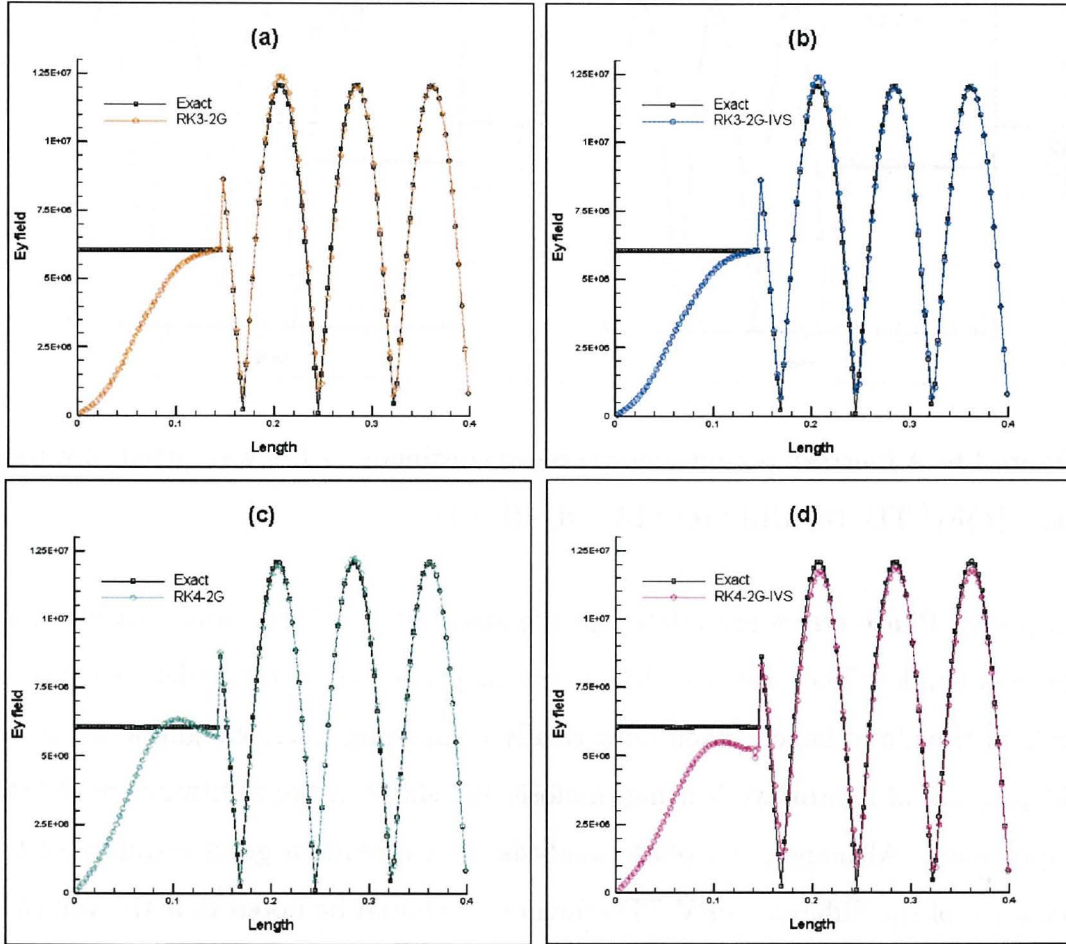


Figure 4.7: A fourteen period time averaged continuous  $TE_{10}$  wave inside a waveguide; (a) RK3-2G; (b) RK3-2G-IVS; (c) RK4-2G; (d) RK4-2G-IVS.

of the spatial unknowns. It is clear that in an empty waveguide the SLF method is more than comparable to the FD-TD scheme.

Results for the empty waveguide have been tabulated. For the other studies conducted hereafter, results will be demonstrated graphically. This is because for microwave heating purposes, the requirement is for time averaged solutions. It is not possible to determine the phase error from values that have been averaged over a number of periods. It should also be noted that in Table 4.2 the CPU time has been normalised against the biggest. This is because the computations were performed on a workstation, with limited amounts of memory. It is expected that given more memory (RAM), the performance of the schemes would dramatically increase. The large differences observed between the low and high order time integration methods is largely due to the fact that the storage requirements of the solver exceeded the available memory, and the computer was forced into using some virtual memory for the computations. Future research will investigate unstructured methods for the solution of microwave heating problems. These will be implemented on high performance computers with large amounts of memory, and hence, more comparable results with regards to CPU time will be demonstrated.

Figures 4.8 to 4.11 depict the results generated for a waveguide that is fully loaded from  $z = 0.25\text{ m}$  metres to  $z = 0.4\text{ m}$  metres. In Figures 4.8 and 4.9 the permittivity of the load is  $\epsilon_r = 1 - 0.2j$ , while in Figures 4.10 and 4.11 the dielectric property of the material is  $\epsilon_r = 2 - 0.5j$ . In the second case, the absorptivity of the material is much larger, and due to the material's properties, more waves should reflect at the dielectric interface. The electric fields have been computed according to (4.62). In all of the studies, the FD-TD scheme has been implemented with the beta correction (4.57) at an interface.

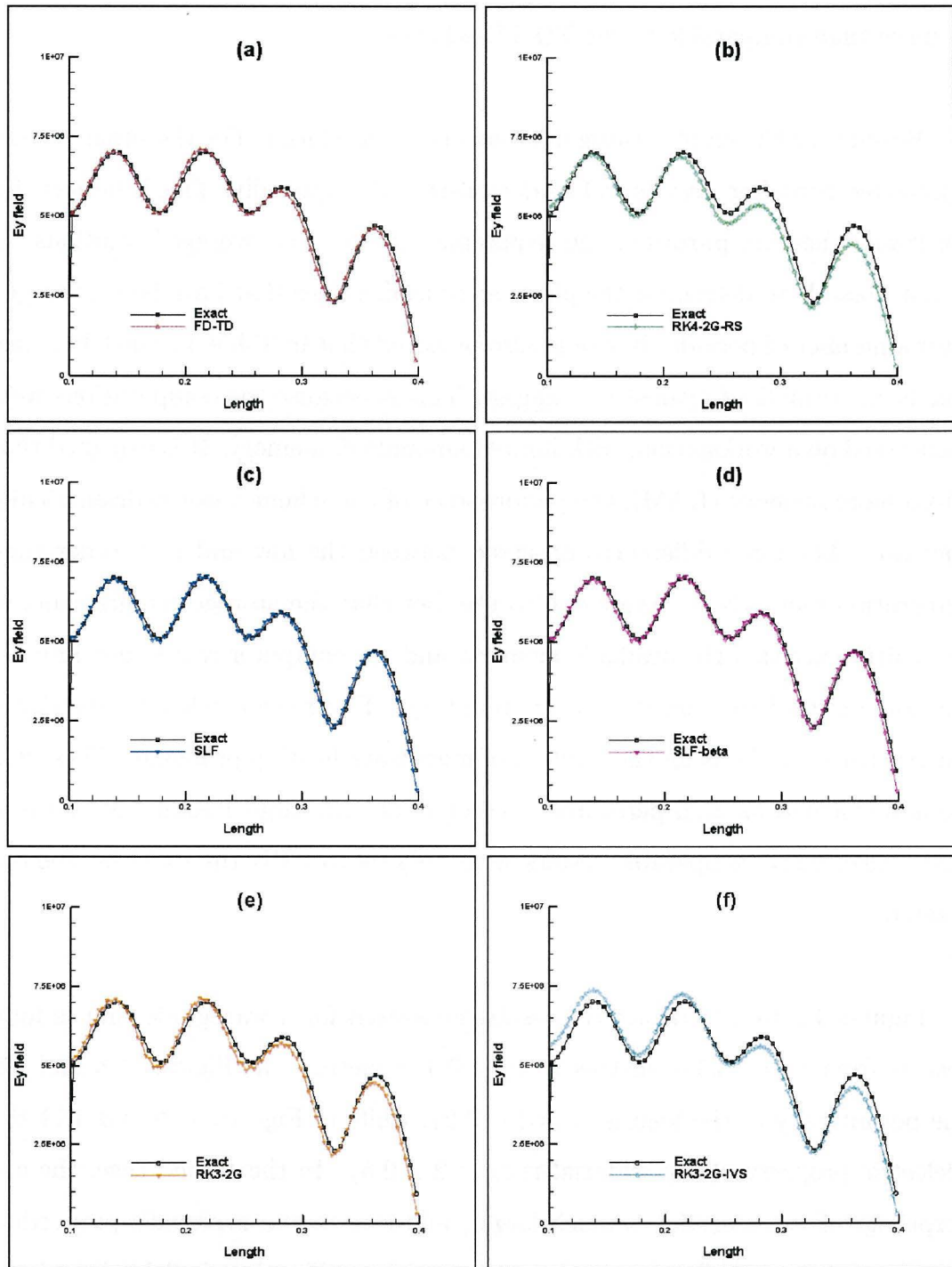


Figure 4.8: A fully loaded waveguide with  $\epsilon_r = 1 - 0.2j$ ; (a) FD-TD; (b) RK4-2G-RS; (c) SLF; (d) SLF-beta; (e) RK3-2G; (f) RK3-2G-IVS.

Figure 4.8(d) shows the result for the SLF method under the plane wave assumption (4.47-4.50), and Figure 4.9(b) shows the beta correction when RK4 time integration is applied. In these figures, it can be seen that for the first dielectric property investigated, the plane wave assumption is of little significance (see Figures 4.8(c-d) and 4.9(a-b)).

It can be seen in Figures 4.8 and 4.9 that when using the beta correction at an interface, the results are comparable to the related schemes that do not utilise the beta correction. However, as the absorptivity of the material is increased the reflections due to the phase changes become more evident. It is therefore clear that by applying the beta correction in the SLF and RK4-2G schemes, the results are smoother (see Figures 4.10(c-d) and 4.11(a-b)).

By placing the unknowns **E** and **H** at the cell-centres, the schemes discussed in this paper evidently introduce oscillations in the numerical solutions, and these oscillations or errors cannot be completely removed without the inclusion of the damping effect in the discrete in space Maxwell's equations.

In Figures 4.9(c-f), the RK4 time integration with a number of applications of intensity vector splitting is established. It is clear from Figures 4.9 and 4.11 that when IVS is used everywhere inside the computational domain there is damping in the solution.

Depending on the implementation of IVS (see Table 4.2) within the numerical solver, the amount of reflection occurring at an interface can be subsequently affected. Figures 4.11(c-f) illustrate that by using the IVS result at a dielectric interface, the wave is better approximated. To reduce the loss of amplitude in the solution, the IVS result should only be used at an interface if there are gradient approximations present (4.20). Although, this is not to say that given higher

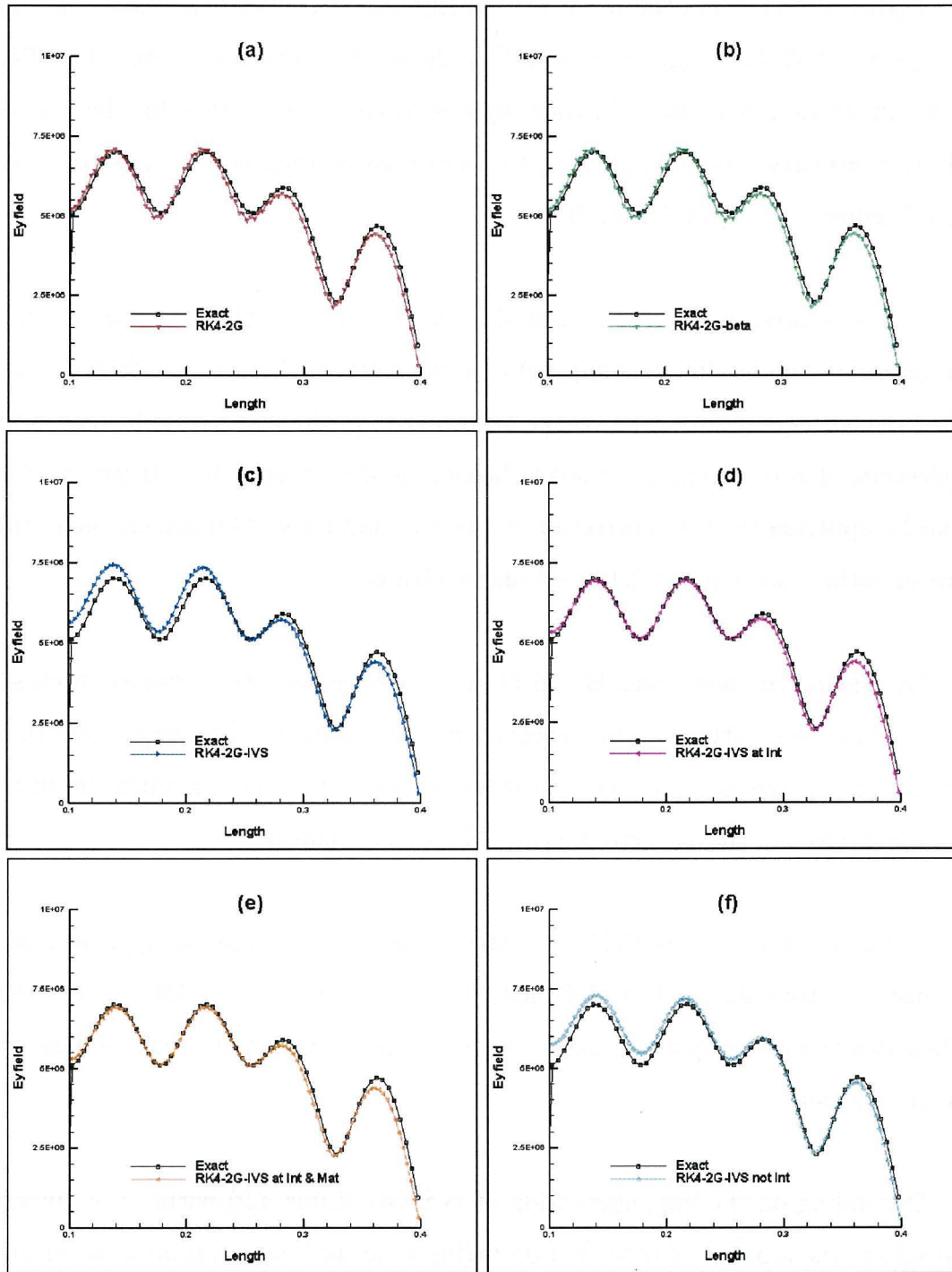


Figure 4.9: A fully loaded waveguide with  $\epsilon_r = 1 - 0.2j$ ; (a) RK4-2G; (b) RK4-2G-beta; (c) RK4-2G-IVS; (d) RK4-2G-IVS at interface; (e) RK4-2G-IVS at interface and material; (f) RK4-2G-IVS not interface.

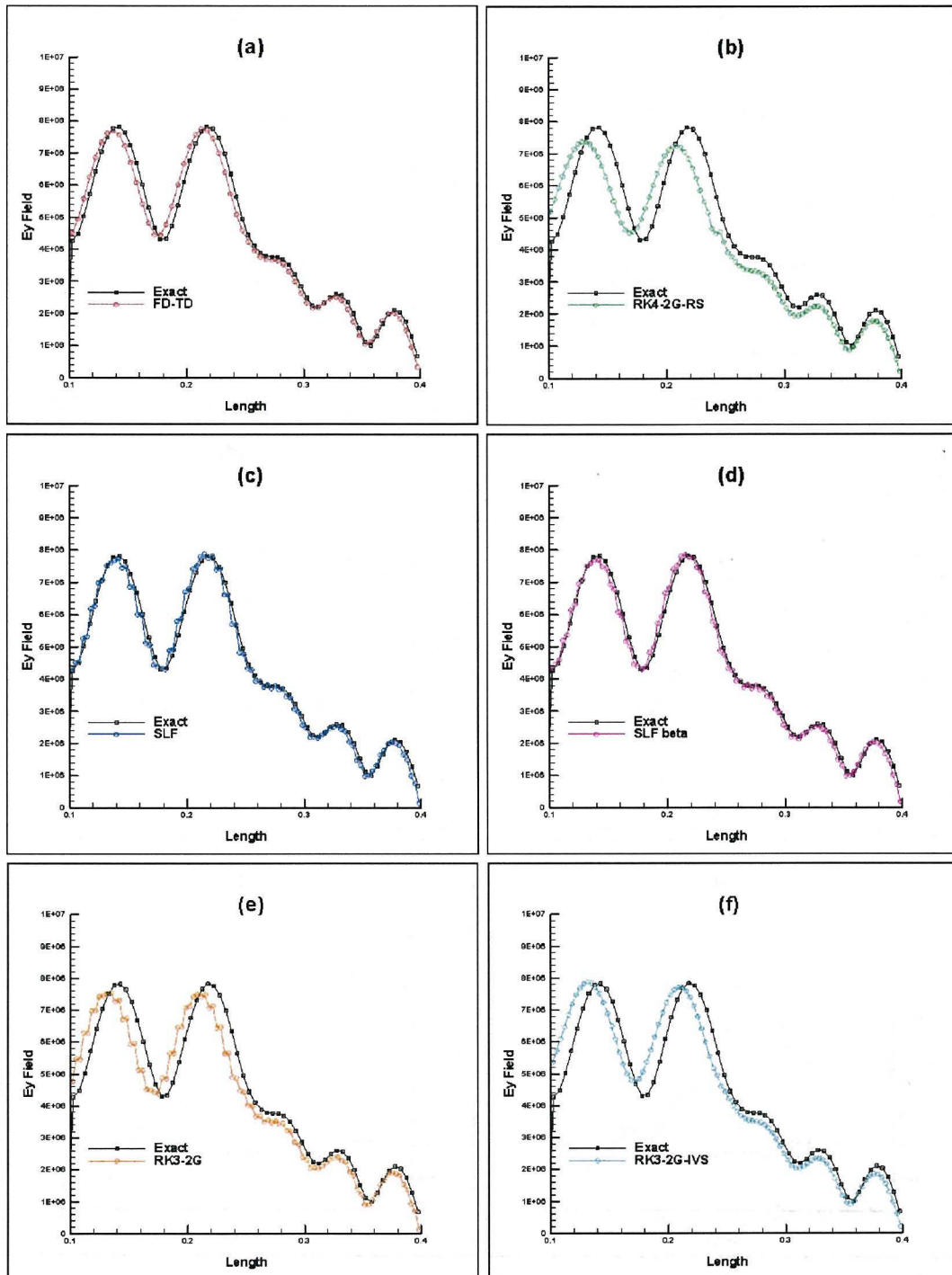


Figure 4.10: A fully loaded waveguide with  $\epsilon_r = 2 - 0.5j$ ; (a) FD-TD; (b) RK4-2G-RS; (c) SLF; (d) SLF-beta; (e) RK3-2G; (f) RK3-2G-IVS.

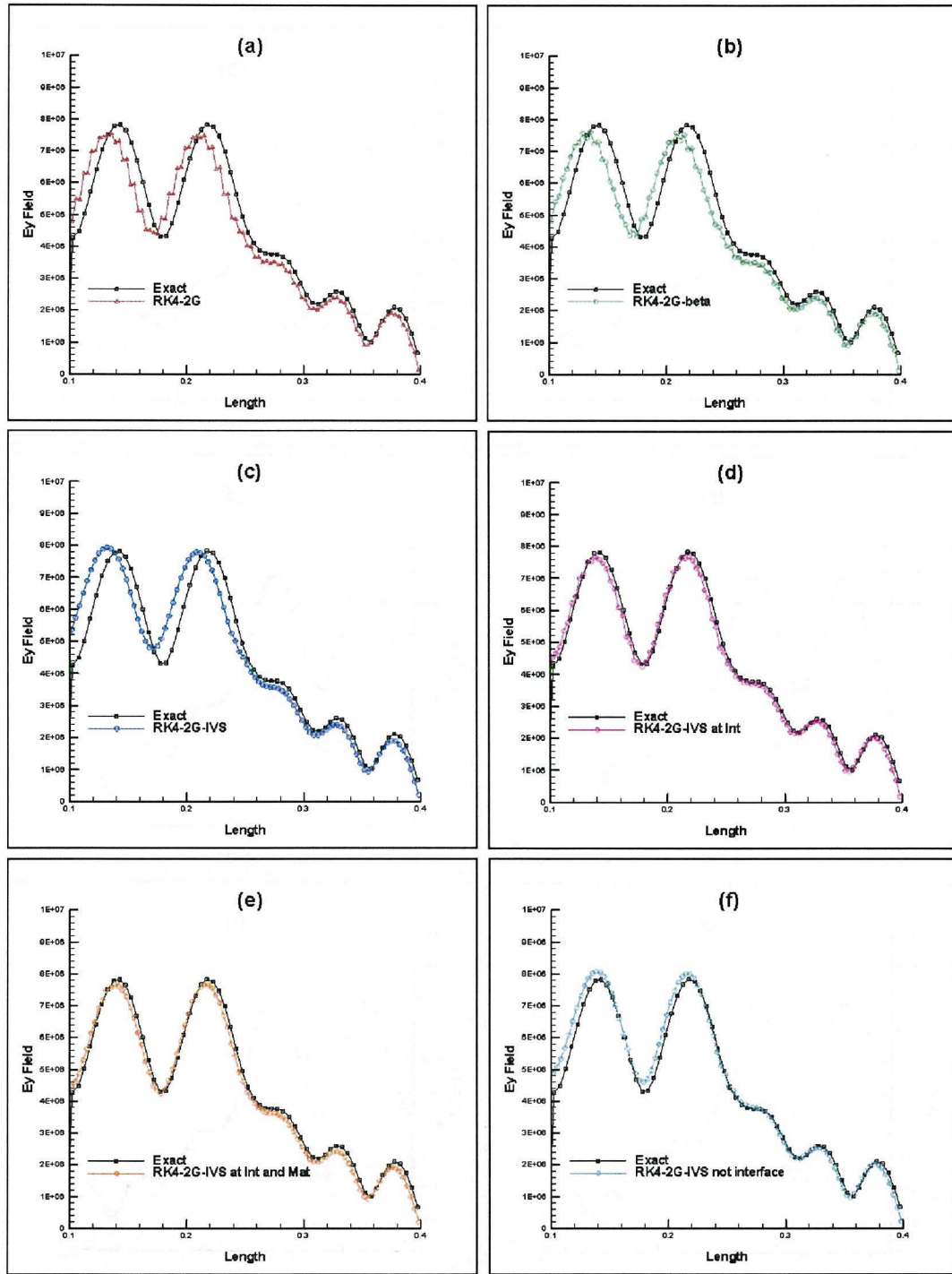


Figure 4.11: A fully loaded waveguide with  $\epsilon_r = 2 - 0.5j$ ; (a) RK4-2G; (b) RK4-2G-beta; (c) RK4-2G-IVS; (d) RK4-2G-IVS at interface; (e) RK4-2G-IVS at interface and material; (f) RK4-2G-IVS not interface.

order spatial discretisations, and hence higher order gradient approximations, the IVS schemes would not perform adequately everywhere. Higher order spatial discretisations will be the topic of future research.

The studies conducted so far have all been on a single mode waveguide. The following sets of simulations were performed on the same waveguide with a load of permeability  $\varepsilon_r = 2 - j$ . The positioning of the load, incident field and PML absorbing layer is shown in Figure 4.12. The simulations were run for sixteen periods, where the last two periods were averaged according to (4.61). The results shown are electric fields for the  $y = 0.025 \text{ m}$  plane. Figure 4.13 exhibits the contour plots of the fields.

The material has height  $0.05 \text{ m}$ , so that it completely fills the waveguide in the  $y$ -coordinate direction. Similarly to the previous examples, the domain has 96000 ( $40 \times 20 \times 120$ ) cells. The time stepping is chosen according to the restriction described in the first study.

It is clear in Figure 4.13 that the introduction of damping removes the noise apparent in the other schemes that do not utilise IVS. FD-TD due to its staggered in space and time discretisation eliminates this error. The introduction of the beta correction tends to smooth the solution (see Figures 4.13(c-d)). For the

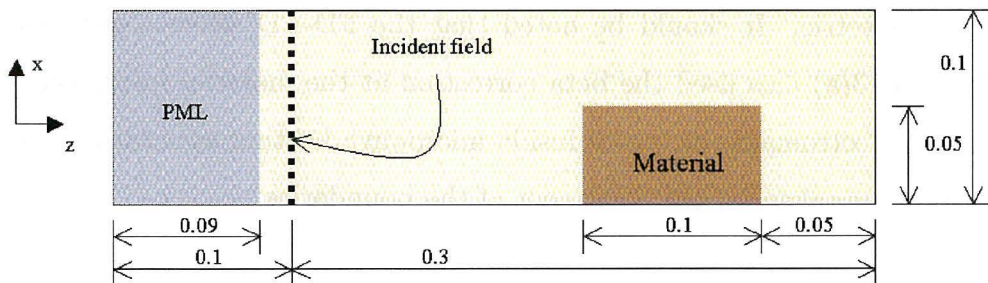


Figure 4.12: The waveguide set up with dielectric for the multi-mode study.

SLF method with beta correction, the plane wave assumption was made on faces adjoining free space.

From the Figures 4.13(c-d) there is an evident difference in the noise inside the guide. The effect of the beta correction slightly dampens the noise that is transmitted and reflected at a boundary. The methods that utilise IVS in Figure 4.13 clearly approximate the solution in a smooth manner.

Figures 4.13(e-f) demonstrate that the RK3-2G technique does not perform as well as the RK4-2G time integration procedure, whether with or without IVS. It can be concluded that RK3-2G methods have high loss of amplitude in waveguides where all the components of the fields exist. That is to say that when there is a load present, the lower order RK methods tend to have larger amplitude losses, even though they performed well in empty waveguide structures. When IVS was applied at the interface of free space and the material alone, the trends in the solution were very similar that to the RK4-2G solution (see Figure 4.13(g)). The difference between the RK4-2G and the RK4-2G method that utilised IVS at an interface was the same as the difference between the SLF and SLF with beta correction techniques (see Figures 4.13(c-d)).

In waveguides that exhibit full field behaviour, the solution can be obtained to higher accuracy by applying some correction to the interface between free space and the dielectric. It should be noted that the FD-TD scheme demonstrated in Figure 4.13(a) also used the beta correction at the material interface. When simulating electromagnetic waves inside microwave heating apparatuses, special care should be taken for the treatment of the boundaries.

In summary, from the previous case studies, the differences between the RK3 and RK4 time integration methods when applied to (4.4) were not obvious in

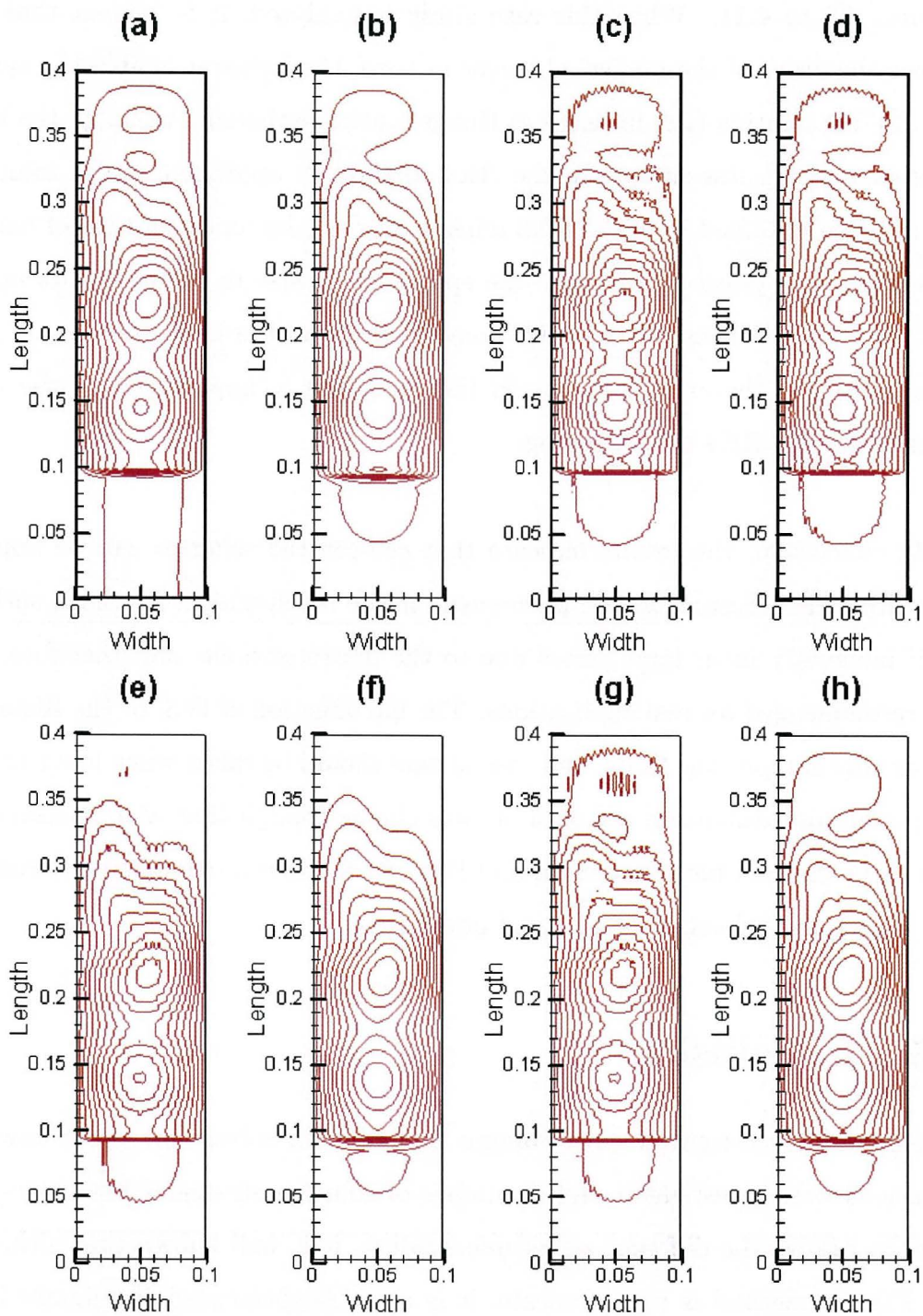


Figure 4.13: Normalised 2D Contour plots of the electric field in a loaded multi-mode waveguide; (a) FD-TD; (b) RK4-2G-IVS not interface; (c) SLF; (d) SLF-beta; (e) RK3-2G; (f) RK3-2G-IVS; (g) RK4-2G; (h) RK4-2G-IVS.

Figures 4.8 to 4.11. When this case study is analysed, it is evident that the higher the order of the numerical solver in time, the better it is able to capture the FD-TD solution (*i.e.* in terms of Runge-Kutta methods). Although the RK3 method requires less time than the RK4 method to approximate the solution, the solution obtained from the RK3 scheme may not be representative of reality. Although, it is possible to reduce the spatial mesh size to reduce errors in the RK3 methods, the cost of the extra computations on the larger number of grid cells outweighs the extra iteration in time required in approximating the next solution for the RK4 time stepping.

In conclusion, the results indicate that cell-centred schemes can be applied to capture the electromagnetic phenomena inside a waveguide. Methods such as ULF inherently incur large errors due to the discretisations, and therefore, are not recommended for real applications. The introduction of IVS, or the Riemann solver may dampen the fields, and special care should be taken when lower orders of spatial approximations are used. It was shown though that with special care and consideration, beta correction and IVS can be used in confidence to correct any oscillatory behaviour at material interfaces.

## 4.5 Conclusion

In this work, cell-centred finite-volume time-domain solvers for the Maxwell's equations were investigated and a number of solution strategies have been applied to resolve the different waveguide studies. It is well known that although the FD-TD method is very accurate, it is not straightforward to migrate it to unstructured domains. A number of cell-centred schemes have been formulated for structured domains, and further research in the area will demonstrate how these schemes can be implemented on completely unstructured grids.

An existing Petropoulos type PML boundary region was investigated and the governing equations reformulated to enable it to be implemented in the new cell-centred solution methodology. It was shown that such an absorbing layer could be applied when simulating microwave heating problems using a cell-centred approach. The plane wave assumption around a material interface has been applied to schemes that do not utilise intensity vector splitting. Depending on the time integration technique and the properties of the material, the results were improved using this strategy.

When intensity vector splitting or the Riemann solver was used, the results appeared to be smooth. This was due to the damping effect that these techniques induced in the numerical solution. Furthermore, it was shown that when using such techniques, care must be taken to insure that the solution is not over-damped, which could impose loss of significance in the solution. Special boundary treatments to cater for lower order dielectric interface conditions were formulated and demonstrated. Taking this into account, structured time-domain cell-centred numerical solvers for the solution of Maxwell's equations in both an empty and loaded waveguide have produced reasonable results that were able to capture the time averaged electric fields sufficiently accurately. These time averaged electric fields are required to predict the power, and hence, the heating distribution inside a load within a waveguide.

This research demonstrates that for the purpose of microwave heating, cell-centred in space techniques can be applied to resolve the microwave power inside a dielectric material. Future research will analyse the techniques described here when applied on tetrahedral meshes both in a waveguide and a cavity structure.



# Bibliography

- [1] Dibben, D.C. and Metaxas, A.C., *Time Domain Finite Element Analysis of Multimode Microwave Applicators Loaded with Low and High Loss Materials.* Intl. Conf. Microwave and High Energy Heating, 1995, 1-3.4.
- [2] Zhao, H. and Turner, I., *An analysis of the finite-difference time-domain method for modelling the microwave heating of dielectric materials within a three-dimensional cavity system.* Journal of Microwave Power and Electromagnetic Energy, 1996, 31(4): p. 199-214.
- [3] Madsen, N.K. and Ziolkowski, R.W., *A three-dimensional modified finite volume technique for Maxwell's equations.* Electromagnetics, 1990, 10: p. 147-161.
- [4] Liu, Y., *Fourier Analysis of Numerical Algorithms for the Maxwell Equations.* Journal of Computational Physics, 1996, 124: p. 396-416.
- [5] Yee, K.S., *Numerical Solution of Initial Boundary Value Problem Involving Maxwell's Equations in Isotropic Media.* IEEE Trans. Antennas Propagat., 1966, 14: p. 302-307.
- [6] Shankar, V. and Mohammadian, A.H., *A Time-Domain, Finite-Volume Treatment for the Maxwell Equations.* 1990, p. 128-145.

- [7] Mohammadian, A.H., Shankar, V. and Hall, W.F., *Computation of electromagnetic scattering and radiation using a time-domain finite-volume discretization procedure*. Comp. Phys. Comm., 1991, **68**: p. 175-196.
- [8] Munz, C.D., Schneider, R. and Voß, U., *A finite-volume method for the maxwell equations in the time-domain*. SIAM Journal of Statistical Computing, 2000, **22(2)**: p. 449-475.
- [9] Petropoulos, P.G., Zhao, L. and Cangellaris, A.C., *A Reflectionless Sponge Layer Absorbing Boundary Condition for the Solution of Maxwell's Equations with High-Order Staggered Finite Difference Schemes*. Journal of Computational Physics, 1998, **139**: p. 184-208.
- [10] Madsen, N.K. and Ziolkowski, R.W., *Numerical solution of Maxwell's equations in the time domain using irregular nonorthogonal grids*. Wave Motion, 1988, **10**: p. 583-596.
- [11] Taflove, A., *Re-inventing Electromagnetics: Supercomputing Solution of Maxwell's Equations Via Direct Time Integration on Space Grids*. AIAA paper 92-0333, 1992, (New York).
- [12] Barth, T.J., *Aspects of Unstructured Grids and Finite-Volume Solvers for the Euler and Navier-Stokes Equations*. Lecture Notes Presented at the VKI Lecture Series, 1994-05, 1995.
- [13] Collin, R.E., *Field Theory of Guided Waves*. 1960, McGraw-Hill Book Company.
- [14] Mur, G., *Absorbing Boundary Conditions for the Finite-Difference Approximation of the Time-Domain Electromagnetic-Field Equations*. IEEE Trans. Microwave Theory Tech. EMC-23, 1981, **4**: p. 377-382.
- [15] Berenger, J.P., *A Perfectly Matched Layer for the Absorption of Electromagnetic Waves*. Journal of Computational Physics, 1993, **114**: p. 185-200.

- [16] Berenger, J.P., *Three-Dimensional Perfectly Matched Layer for the Absorption of Electromagnetic Waves*. Journal of Computational Physics, 1996, **127**: p. 363-379.
- [17] Zhao, H., *Computational Models and Numerical Techniques for Solving Maxwell's Equations: A Study of Heating of Lossy Dielectric Materials Inside Arbitrary Shaped Cavities*. Centre in Statistical Science and Industrial Mathematics, 1997, Queensland University of Technology, Brisbane.



# Chapter 5

## A Hybrid Approach for Resolving the Microwave Heating Inside Lossy Media

### Statement of Joint Authorship

**Vegh, V.** (Candidate) Numerically modelled a number of different time domain solvers for propagating a Gaussian pulse inside a waveguide, interpreted the results and wrote the manuscript, acted as corresponding author, proof read manuscript.

**Turner, I. W.** Suggested ways of improving the different numerical time domain solvers, directed and guided the work, assisted with interpretation of results and the preparation of the paper.

NOMENCLATURE	
<b>B</b>	Magnetic flux density ( $T$ )
<b>E</b>	Electric field intensity ( $V$ )
<b>J</b>	Current density ( $A/m^2$ )
<i>f</i>	Frequency ( $Hz$ )
<i>j</i>	Imaginary unit ( $\sqrt{-1}$ )
<i>p</i>	The $p^{th}$ cell of the domain
<i>S</i>	Surface area ( $m^2$ )
<i>T</i>	Period inside waveguide ( $s$ )
$\Delta S$	Surface area of face $F$ ( $m^2$ )
$\Delta V$	Volume of the $p^{th}$ cell ( $m^3$ )
$\epsilon_0$	Free-space permittivity ( $8.85 \times 10^{-12} (F/m)$ )
$\epsilon'$	Relative dielectric constant
$\mu_0$	Free-space permeability ( $4\pi \times 10^{-7} (H/m)$ )
$\sigma$	Electric conductivity ( $\Omega^{-1}/m$ )
<b>D</b>	Electric flux density ( $V/m$ )
<b>H</b>	Magnetic field intensity ( $A/m$ )
<b>n</b>	Unit outward normal to face $F$
<i>F</i>	A face of cell $p$
<i>n</i>	The $n^{th}$ time level
<i>P</i>	Power ( $W$ )
<i>t</i>	Time ( $s$ )
<i>V</i>	Volume ( $m^3$ )
$\Delta t$	Time step of numerical scheme ( $s$ )
$\epsilon$	Permittivity ( $F/m$ )
$\epsilon_r$	Relative permittivity ( $\epsilon' - \epsilon'' j$ )
$\epsilon''$	Relative loss factor
$\omega$	Angular frequency ( $2\pi f$ ) ( $rad/s$ )
$\zeta_p$	Faces that constitute the $p^{th}$ cell

Table 5.1: List of symbols used in Chapter 5.

## Abstract

In this work a novel hybrid approach is presented that uses a combination of both time domain and frequency domain solution strategies to predict the power distribution within a lossy medium loaded within a waveguide. The problem of determining the electromagnetic fields evolving within the waveguide and the lossy medium is decoupled into two components, one for computing the fields in the waveguide including a coarse representation of the medium (the exterior problem) and one for a detailed resolution of the lossy medium (the interior problem). A previously documented cell-centred Maxwell's equations numerical solver can be used to resolve the exterior problem accurately in the time domain. Thereafter the discrete Fourier transform can be applied to the computed field data around the interface of the medium to estimate the frequency domain boundary condition information that is needed for closure of the interior problem. Since only the electric fields are required to compute the power distribution generated within the lossy medium, the interior problem can be resolved efficiently using

the Helmholtz equation. A consistent cell-centred finite-volume method is then used to discretise this equation on a fine mesh and the underlying large, sparse, complex matrix system is solved for the required electric field using the iterative Krylov subspace based GMRES iterative solver. It will be shown that the hybrid solution methodology works well when a single frequency is considered in the evaluation of the Helmholtz equation in a single mode waveguide. A restriction of the scheme is that the material needs to be sufficiently lossy, so that any penetrating waves in the material are absorbed.

## 5.1 Introduction

Over the last two decades, researchers in the field of computational electromagnetics (CEM) have explored a number of numerical techniques to resolve the electromagnetic fields inside waveguide and cavity structures [1-5]. The popular finite-difference time-domain (FD-TD) method originally proposed by Yee [6] provides very accurate results on structured domains, however it is not straightforward to migrate the scheme to an entirely unstructured mesh. The FD-TD method has been used previously in the literature with great success to simulate microwave heating problems [5, 7]. It is proposed here to use a hybrid approach that combines the frequency and time domain numerical solvers to resolve the power distribution inside a waveguide loaded with a lossy medium.

Typically, the FD-TD method when applied to computing the power distribution in a lossy dielectric load can be a computationally intensive (in terms of CPU time and memory) solution scheme. This research work aims to establish a scheme that can predict the heating distribution inside a lossy medium, both accurately and efficiently. To achieve this goal, a new hybrid approach is developed whereby the problem of determining the electromagnetic fields evolving within the waveguide and the lossy medium is decoupled into an exterior problem for

computing the fields in the waveguide, including a coarse representation of the medium and an interior problem for a detailed resolution of the lossy medium. This scheme is demonstrated on structured grids, so that the accuracy of the developed method can be compared to the exact solution. Since the motivation behind this research is to develop numerical schemes that can be used on unstructured grids, a time-domain scheme that is unstructured in theory needs to be implemented. Here, an existing cell-centred time domain numerical solver for the Maxwell's equations is used in the free-space component of the domain to resolve the electromagnetic field behaviour [8]. The cell-centred numerical solver is discussed in the section labelled Numerical Solution of the Maxwell's Equations.

In the past, a number of researchers in the field of electromagnetics and microwave heating have used frequency domain strategies to predict the power distribution inside lossy media [9, 10]. However, it was highlighted that when the analysis is performed on the whole domain of the waveguide, including the load or material, the decomposition when formulated into a system of linear equations yields a coefficient matrix that is highly ill-conditioned. Adaptive iterative techniques that use left and right preconditioning have to be utilised to obtain electric field solutions inside the material. Although, it is possible to condition (via left and right preconditioning) a matrix that performs well numerically, a small change in the layout of the problem can cause the system to break down numerically. The strict ill conditioning in the coefficient matrix is generally related to the implementation and spatial location of the boundary information.

The hybrid method proposed here aims to utilise the schemes to their full advantage in the time and frequency domains. The time-domain solver is used to predict boundary information via the discrete Fourier transform (DFT). This procedure is normally fast, due to the fact that the time-stepping constraints of the time-domain solver are restricted by only the free-space properties. Given

that the boundary information at a material interface can be obtained accurately and efficiently, the Helmholtz equation can be resolved using a mesh imposed on the domain of the load alone. The boundary information obtained from DFT is used as the material boundary condition in the solution of the Helmholtz equation. The resulting system of equation that governs the physical phenomena in the material is better conditioned than a system that is representative of the domain of the free-space and the load. Such a system of linear equations is solved using a Krylov subspace method [11]. Normally for multi-mode cavities, the solution to the Helmholtz problem is obtained for a number of frequencies within the vicinity of the dominant mode. This is necessary if representative electric field behaviour inside the load is to be attained.

## 5.2 Numerical Solution of the Maxwell's Equations - Exterior Problem

In free-space, the time-domain numerical method is used to obtain the solution of the microwave applicator on a coarse grid that satisfies the stability requirements for the external region of the computational domain, excluding the lossy material. To do this, a cell-centred numerical solver is used to predict the electric and magnetic field components for discrete cells [8]. All of the components of the electric and magnetic fields are located at the same cell-centred spatial location. For a given cell, interpolation is used to estimate the facial unknowns.

To establish the cell-centred scheme, the Maxwell's equations have to be revisited and formulated to cater for electric and magnetic field components at the cell-centres:

$$\nabla \times \mathbf{E} = -\frac{\partial \mathbf{B}}{\partial t}, \quad \nabla \times \mathbf{B} = \frac{\partial \mathbf{D}}{\partial t} + \mathbf{J}, \quad (5.1)$$

$$\mathbf{B} = \mu_0 \mathbf{H}, \mathbf{D} = \epsilon \mathbf{E}, \mathbf{J} = \sigma \mathbf{E}, \epsilon = \epsilon_0 \epsilon', \sigma = \omega \epsilon_0 \epsilon''.$$

The Maxwell's equations (5.1) are transformed into a surface-volume representation. To obtain this form, the divergence theorem with certain vector product properties has to be incorporated into the evaluation of the equation:

$$\iint_S \mathbf{n} \times \mathbf{E} \partial S = - \iiint_V \frac{\partial \mathbf{B}}{\partial t} \partial V, \iint_S \mathbf{n} \times \mathbf{H} \partial S = \iiint_V \frac{\partial \mathbf{D}}{\partial t} \partial V, + \iiint_V \mathbf{J} \partial V. \quad (5.2)$$

From (5.2), the discrete in space form of the Maxwell equations can be deduced directly. For a given cell in the computational domain, the electromagnetic behaviour can be represented at a point  $p$  as:

$$\frac{\partial \mathbf{B}_p}{\partial t} = -\frac{1}{\Delta V} \sum_{F \in \zeta_p} \mathbf{n} \times \mathbf{E}_F \Delta S_F, \quad \frac{\partial \mathbf{D}_p}{\partial t} = \frac{1}{\Delta V} \sum_{F \in \zeta_p} \mathbf{n} \times \mathbf{H}_F \Delta S_F - \mathbf{J}_p. \quad (5.3)$$

To resolve (5.3) in terms of time, a staggered Leapfrog discretisation is adapted to the left-hand sides of (3). The resulting system of equations is expressed as:

$$\mathbf{H}_p^{n+\frac{1}{2}} = \mathbf{H}_p^{n-\frac{1}{2}} - \frac{\Delta t}{\mu_0 \Delta V} \sum_{F \in \zeta_p} \mathbf{n} \times (\mathbf{E}_F)^n \Delta S_F,$$

$$\mathbf{E}_p^{n+1} = \frac{2\epsilon - \sigma \Delta t}{2\epsilon + \sigma \Delta t} \mathbf{E}_p^n + \frac{2\Delta t}{(2\epsilon + \sigma \Delta t) \Delta V} \sum_{F \in \zeta_p} \mathbf{n} \times (\mathbf{H}_F)^{n+\frac{1}{2}} \Delta S_F, \quad (5.4)$$

where, the magnetic and electric fields at a given cell-centre have been staggered half a time step apart. In (5.4),  $\mathbf{n}$  is the unit outward normal to face  $F$ , and  $\zeta_p$  is the set of faces that constitute the  $p^{th}$  cell in a computational domain.  $\Delta S_F$  and  $\Delta V$  are the surface area of a particular face in  $\zeta_p$  and the volume of the  $p^{th}$  cell, respectively. On structured grids, the facial values can be obtained by simply averaging the cell-centre values of the cells common to that face. Such

averaging of the cell values provides a second order in space and second order in time numerical scheme. The method in (5.4) is usually referred to as a staggered Leapfrog discretisation (SLF) to Maxwell's equations.

### 5.3 Numerical Solution of the Helmholtz Equation - Interior Problem

Numerous applications for computing the electromagnetic fields using frequency domain solution strategies for the purpose of heating have been employed in the past [7, 9, 10]. In this section, the frequency domain equations are outlined, and brief descriptions of the different terms are provided. In time-harmonic form, the electromagnetic behaviour can be represented as a set of coupled curl equations:

$$\nabla \times \mathbf{H} = (\sigma + j\omega\epsilon)\mathbf{E}, \quad \nabla \times \mathbf{E} = -j\omega\mu\mathbf{H}. \quad (5.5)$$

In (5.5), by taking the curl of the latter equation, and substituting it into the first expression, the following Helmholtz equation for the electric field that satisfies the divergence criteria is obtained:

$$\nabla^2 \mathbf{E} + k^2 \mathbf{E} = 0, \quad (5.6)$$

$$k^2 = \mu_0\omega(\omega\epsilon - \sigma j).$$

Note that since the interest lies in computing the power distribution, it is necessary only to determine the electric field inside the lossy medium. On structured grids, (5.6) can be discretised using the standard (for example, second-order) finite-difference stencil to obtain a system of linear equations. This yields a finite-volume method for the spatial discretisations. When written in matrix form, the resulting large, sparse complex system of equations can be solved using the GMRES method [11]. Other methods can be used with and without

preconditioning to obtain the solution to the discrete system governed by (5.6). Since  $\omega$  is frequency dependent, for multi-mode waveguides and cavities, the system obtained from the discretisation of (5.6) has to be resolved for a number of distinct frequencies. The number of frequencies used in the evaluation of the power distribution depends on the different modes existent in the microwave heating apparatus. Normally, a number of discrete frequencies have to be taken in the neighbourhood of the dominant frequency to identify the power distribution within the medium. The solutions at these discrete frequencies are then collated, to obtain the electric field behaviour inside the material or load. The power distribution is calculated from the electric field inside the domain of the material using the following equation:

$$P_p = \sigma |\mathbf{E}_p|^2. \quad (5.7)$$

The scope of this research is limited to finding the power distribution inside the lossy medium. If required, the power distribution can be coupled with the forced heat equation to obtain heating inside the material.

## 5.4 Summary of the Hybrid Method

The proposed hybrid model combines a time dependent solver with the Helmholtz equation, and calculates the power distribution from the electric field Helmholtz equation. In this case, the time dependent equations are solved everywhere, even inside the material, to maintain consistency of the solution. It can be shown that for lossy media on a fairly coarse mesh, it is possible to capture the time dependent unknowns at an interface between free-space and the dielectric load. Generally, the computed time dependent solution contains fairly large errors inside the load, but it maintains a good approximation to the solution in the free-space region, and particularly at the material interface.

For a multi-mode waveguide or cavity, by using discrete Fourier transform, it is possible to take a band of discrete frequencies in the neighbourhood of the dominant frequency and transform the time dependent solution to the frequency domain (typically, for a period of the wave). This has to be performed once the time dependent solution has assumed a plane wave form. During the time stepping of the numerical solver at the interface between the free-space and the dielectric load, the time dependent electric fields are mapped to their equivalent fields in the frequency domain. Once the electric field on the material boundaries at a particular frequency has been computed, the Helmholtz equation is solved implicitly at that discrete frequency. Since all of the frequency dependent electric fields are computed using DFT on the faces of the material, the resulting system of linear equations is complex, also in this case it is sparse and banded. To find the solution to such a matrix system, a reliable iterative solver without preconditioning is utilised (GMRES) [11]. The Hybrid scheme makes the assumption of a single dominant mode inside the microwave heating apparatus. For microwave heating, the frequency bandwidth is narrow, hence the assumption of a single dominant frequency inside the microwave applicator makes the time-harmonic solution feasible.

## 5.5 Results

A simple study to demonstrate the potential of the Hybrid method has been considered and investigated. The implementation of a loaded waveguide study is illustrated. The results are compared to the exact solution to assess the accuracy of the method. The SLF scheme outlined in a previous section was used to generate the frequency domain boundary information for the Helmholtz equation. The time-domain information at material interfaces was converted to the frequency domain using a number of frequencies in the neighbourhood of the

dominant  $TE_{10}$   $2.45GHz$  mode. It was observed that for this study, the dominant frequency could accurately capture the exact solution. The incident  $TE_{10}$  wave was smoothed using a Gaussian function:

$$gauss(t) = \begin{cases} e^{-(\frac{t}{T}-3)^2} & t \leq 3T \\ 1 & t > 3T \end{cases}, \quad (5.8)$$

where,  $T$  is the period of the wave. The waveguide is dimensioned  $0.1 \times 0.05 \times 0.4 m^3$ . A load of size  $0.1 \times 0.05 \times 0.1 m^3$  was placed at the short circuit end of the waveguide. At  $z = 0.1$  metres, the incident field was imposed to propagate the electromagnetic fields. The material was discretised using a mesh of size  $40 \times 20 \times 30$  cells (ie. 24000 cells).

For this study, the standard conducting wall boundary conditions were implemented. Any impinging reflected waves in the scattered field region of the guide were absorbed using a perfectly matched layer (PML) absorbing boundary condition [12].

In Figures 5.1 and 5.2, the Hybrid method is compared to the exact solution. The Hybrid method has been implemented using the dominant  $2.45GHz$  frequency. In the figures, the power distribution is calculated for a material with properties  $\epsilon_r = 2 - \frac{1}{2}j$  and  $\epsilon_r = 3 - j$ , respectively. The solution has been normalised (ie. scaled by the largest value), so that the scheme can be compared using the same legend and any similarities in the solution between the Hybrid method and the exact solution can also be demonstrated. For heating purposes, the magnitude of the power distribution is less important than the location of the hot spots, and hence, the focus concerns the analysis of the locations of the hot spots. It can be seen from the figure that at the sole  $2.45GHz$  frequency Hybrid solution, the power distribution is obtained fairly accurately, and the numerical approximation obtained from the Hybrid method tends to be the one observed

by the exact solution. Rigorous amplitude analysis for the Hybrid scheme is left to future research.

Computationally, the classical FD-TD method is very fast. Though, the Hybrid scheme uses a coarser grid outside the domain of the material, and for this reason, when the Hybrid solution is computed for a single frequency, the time to obtain the solution is comparable to the FD-TD method.

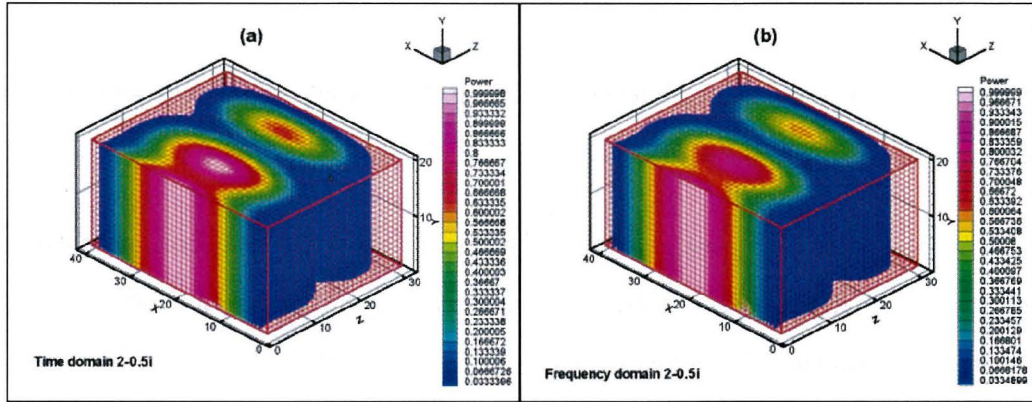


Figure 5.1: The Hybrid method compared to the exact solution (dielectric property  $\varepsilon_r = 2 - \frac{1}{2}j$ ); (a) exact solution, and (b) Hybrid-2.45GHz.

## 5.6 Conclusions

This research work illustrates that a cell-centred Maxwell's equations numerical solver with Leapfrog time integration can be used to obtain the frequency domain boundary condition information via the discrete Fourier transform at the material interfaces. This boundary information is then used to resolve the Helmholtz equation for the electric fields at several frequencies within the lossy medium.

At the dominant frequency, the Hybrid method was used to solve for the electric fields inside a microwave heating apparatus. The electric fields are then

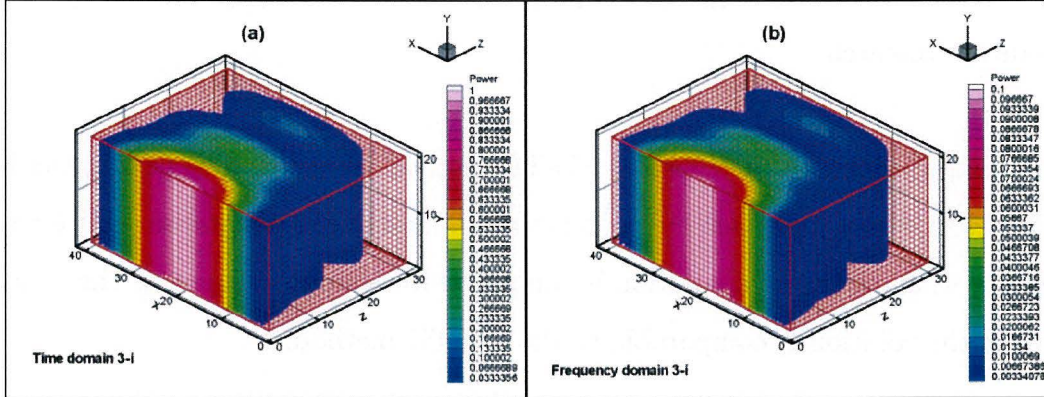


Figure 5.2: The Hybrid method compared to the exact solution (dielectric property  $\varepsilon_r = 3 - j$ ); (a) exact solution, and (b) Hybrid-2.45GHz.

directly related to the power distribution inside the lossy medium. For this simple case study, it is evident from the results that the Hybrid method can capture the electromagnetic field behaviour inside the material for lossy media more than adequately.

This new solution methodology initiates future work on unstructured domains for hybrid solvers for multi-mode cavities, where decoupled domains for both the free space and the lossy medium can be utilised for predicting the power distribution inside a lossy arbitrarily shaped material loaded inhomogeneously within a microwave cavity structure. The impact of using preconditioning in the solution strategy of the Hybrid method is currently under investigation. Future work will also investigate numerical solvers that use higher order approximations for the cell face unknowns. In that work, material interface boundary treatments using dielectric properties will also be considered and treated. Further investigation on preconditioners will also be carried out.

# Bibliography

- [1] Mur, G., *Absorbing Boundary Conditions for the Finite-Difference Approximation of the Time-Domain Electromagnetic-Field Equations*. IEEE Trans. Microwave Theory Tech. EMC-23, 1981, 4: p. 377-382.
- [2] Madsen, N.K., Ziolkowski, R.W., *Numerical solution of Maxwell's equations in the time domain using irregular nonorthogonal grids*. Wave Motion, 1988, 10: p. 583-596.
- [3] Shankar, V., Mohammadian, A.H., *A Time-Domain Finite-Volume Treatment for the Maxwell Equations*, 1990, p. 128-145.
- [4] Dibben, D.C., *Numerical and Experimental Modelling of Microwave Applicators*. Department of Engineering, 1995, University of Cambridge. p. 188.
- [5] Zhao, H., *Computational Models and Numerical Techniques for Solving Maxwell's Equations: A Study of Heating of Lossy Dielectric Materials Inside Arbitrary Shaped Cavities*. Centre in Statistical Science and Industrial Mathematics, 1997, Queensland University of Technology, Brisbane.
- [6] Yee, K.S., *Numerical Solution of Initial Boundary Value Problem Involving Maxwell's Equations in Isotropic Media*. IEEE Trans. Antennas Propagat, 1966, 14: p. 302-307.

- [7] Jia, X., Jolly, P., *Simulation of Microwave Field and Power Distribution in a Cavity by a Three-Dimensional Finite Element Method*. Jounral of Microwave Power, 1992, 27(1): p. 11-22.
- [8] Vegh, V., Turner, I.W., *Comparison of Time Domain Numerical Solvers for the Propagation of a Gaussian Pulse Inside a Rectangular Waveguide*. Presented at CTAC2001 Conference (Brisbane), paper under review for a special issue of the ANZIAM Journal, 2001.
- [9] Madsen, N.K., Ziolkowski, R.W., *A three-dimensional modified finite volume technique for Maxwell's equations*. Electromagnetics, 1990, 10: p. 147-161.
- [10] Dibben, D.C., Metaxas, A.C., *Time Domain Finite Element Analysis of Multimode Microwave Applicators Loaded with Low and High Loss Materials*. Intl. Conf. Microwave and High Energy Heating, 1995, 1-3.4.
- [11] Saad, Y., M.H.S., GMRES: *a generalized minimum residual algorithm for solving nonsymmetric linear systems*. SIAM Journal of Scientific and Statistical Computing, 1986, 7: p. 856-869.
- [12] Vegh, V., Turner, I.W., Zhao, H., *Effective cell-centred time-domain Maxwell's equations numerical solvers for the purpose of microwave heating*. Under review for the Journal of Applied Mathematical Modelling, 2001.

# **Chapter 6**

## **A Hybrid Technique for Computing the Power Distribution Generated in a Lossy Medium During Microwave Heating**

### **Statement of Joint Authorship**

**Vegh, V.** (Candidate) Implemented the Hybrid method for waveguide and cavity case studies, interpreted the results and wrote the manuscript, acted as corresponding author, proof read manuscript.

**Turner, I. W.** Suggested ways of improving the Hybrid method, directed and guided the work, assisted with interpretation of results and the preparation of the paper, proof read the manuscript.

NOMENCLATURE	
<b>A</b>	Coefficient matrix
<b>B</b>	Magnetic flux density ( $T$ )
<b>E</b>	Electric field intensity ( $V$ )
<b>J</b>	Current density ( $A/m^2$ )
<b>r</b>	Spatial location vector
<i>f</i>	Frequency (Hz)
<i>k</i>	The $k^{th}$ frequency
<i>nb</i>	Neighbour node to $p$
<i>P</i>	Power (W)
<i>t</i>	Time (s)
<i>V</i>	Volume ( $m^3$ )
$\alpha_2$	Constant
$\Delta S$	Surface area of face $f$ ( $m^2$ )
$\Delta V$	Volume of the $p^{th}$ cell ( $m^3$ )
$\epsilon_0$	Free-space permittivity ( $8.85 \times 10^{-12} (F/m)$ )
$\epsilon'$	Relative dielectric constant
$\epsilon_f$	Correction term for face $f$
$\mu_0$	Free-space permeability ( $4\pi \times 10^{-7} (H/m)$ )
$\phi$	Frequency dependent electric field
$\xi$	Frequency dependent magnetic field
<b>b</b>	Right hand vector
<b>D</b>	Electric flux density ( $V/m$ )
<b>H</b>	Magnetic field intensity ( $A/m$ )
<b>n</b>	Unit outward normal to face $f$
<i>f</i>	A face of cell $p$
<i>i</i>	Imaginary unit ( $\sqrt{-1}$ )
<i>n</i>	The $n^{th}$ time level
<i>p</i>	The $p^{th}$ cell of the domain
<i>S</i>	Surface area ( $m^2$ )
<i>T</i>	Period inside waveguide (s)
$\alpha_1$	Constant
$\alpha_3$	Constant
$\Delta t$	Time step of numerical scheme (s)
$\epsilon$	Permittivity ( $F/m$ )
$\epsilon_r$	Relative permittivity ( $\epsilon' - \epsilon'' j$ )
$\epsilon''$	Relative loss factor
$\mathcal{H}$	Hessian matrix
$\omega$	Angular frequency ( $2\pi f$ ) (rad/s)
$\sigma$	Electric conductivity ( $\Omega^{-1}/m$ )
$\zeta_p$	Faces that constitute the $p^{th}$ cell

Table 6.1: List of symbols used in Chapter 6.

## Abstract

Over the years researchers in the field of Computational Electromagnetics (CEM) have investigated and explored a number of different techniques to resolve electromagnetic fields inside waveguide and cavity structures. The equations that govern the fundamental behaviour of electromagnetic wave propagation in such structures are the Maxwell's equations. In the literature, a number of different techniques have been employed to solve these equations and out of these methods, the classical Finite-Difference Time-Domain (FD-TD) scheme, which uses a staggered time and space discretisation, is the most well-known and widely used. However, this scheme is complicated to implement on an irregular computational

domain using unstructured meshes.

This research work builds upon previous work undertaken for a waveguide, where a coupled method was introduced for the solution of the governing electromagnetic equations. In that work, the free-space component of the solution was computed in the time-domain, whilst the power distribution in the load was resolved using the frequency dependent electric field Helmholtz equation. This methodology resulted in a time-frequency domain hybrid scheme. In this paper, the hybrid method has been tested further for both waveguide and cavity configurations that are loaded with a lossy dielectric material. Numerical tests highlight both the accuracy and computational efficiency of the proposed hybrid strategy for predicting the power distribution generated during microwave heating processes. The accuracy of the hybrid scheme is gauged by direct comparison with the FD-TD numerical solutions and previously published thermal images.

## 6.1 Introduction

The development of technological advances in the Sciences and Computing [1, 2] has been the requirement to resolve ever-greater applications in electromagnetics. Applications of electromagnetic energy range from satellite communication systems and stealth detection in the defences, to communication of data between geographically displaced locations in Information Technology, and to tree root sterilisation in the sewage industry. Most of the applications, in one form or another, can be decomposed into a subset of local problems in electromagnetic theory [3, 4]. For example, in microwave wood drying, the electromagnetic field behaviour outside of the domain of the wood (referred to as the exterior problem) is of little interest, and the problem should be focused primarily on predicting the heating or power distribution generated inside the material [5] (the interior problem). In such circumstances, it is only natural to develop methods that can

concentrate the computational impetus on the interior problem and obtain solutions to these accurately and efficiently. The Hybrid method [6] is one such method that enables the electromagnetic fields evolving within the interior problem to be solved at a relatively high resolution, and reduces the often exhaustive computational overheads of CPU time and memory requirements associated with the exterior domain.

The new hybrid approach proposed in [6] for resolving the electromagnetic phenomena in a waveguide structure is based on the coupling of a time-marching Maxwell's equations numerical solver and a frequency-domain Helmholtz equation solution. In the past, both the time-domain and frequency-domain techniques have been applied individually, without coupling to study a variety of microwave heating applications [5, 7, 8, 9, 10]. When solely using time-domain numerical solvers like the Finite-Difference Time-Domain (FD-TD) method [11], some restrictions on the problem have to be imposed (for example mesh size and element shape), so that a convergent solution can be obtained. In some problems the irregular shape of both the apparatus and load restrict the numerical solver from obtaining accurate solutions to the electromagnetic field evolutions, and consequently, other methods are sought to better capture the nature of the electric and magnetic field components.

Typically, in the FD-TD method the errors for the discretisations are minimised because of the staggering of the spatial locations of the electric and magnetic field components to cells edges and cell faces respectively, and the positioning of the electric and magnetic fields half a time step apart. Over the last decade there have been a number of modifications made to the FD-TD method to better its performance through revision of reflected and refracted waves at material interfaces [12], and by applying different types of absorbing boundary conditions [13, 14]. Unfortunately, FD-TD cannot be implemented on unstructured grids in

a straightforward manner [12]. Researchers are attempting to take the FD-TD solution strategy and migrate it to an unstructured domain [5], but such work has not been entirely successful. The main complexity arises due to the construction of the dual cell, which for general unstructured meshes sees the normal vectors to the primary cell faces not aligned with the edges of the dual cell [15, 16].

Frequency, or time-harmonic numerical methods possess different restrictions when the frequency dependent electromagnetic theory is applied to industrial microwave heating problems. The classical Helmholtz equation [4], which is derived from the time-harmonic magnetic and electric field point relations can be used to obtain the electric fields inside the material and free-space, without having to compute the magnetic fields. On the other hand, in the time-domain solvers, both electric and magnetic fields must be computed. The advantage of the Helmholtz equation is that the power distribution is obtained easily from the frequency domain solution of the electric field, without the need to compute the magnetic field. It is well-known that time-marching schemes require a fairly large number of electromagnetic wave period computations before adequate power distributions can be obtained [5]. It is also well-known that time-harmonic schemes tend to generate coefficient matrices in the implicit solution strategy that are highly ill-conditioned, and hence, require innovative and computationally intensive numerical techniques to obtain a solution to the problem [9]. Consequently, both time and frequency domain strategies have restrictions that constrain the numerical performance of the underlying electromagnetic algorithm.

Unlike the FD-TD method, which marches the solution in time according to some stability criterion imposed due to both material and grid properties, the Helmholtz equation solution strategy presents a system of linear equations. This system of linear equations is sparse and as mentioned above, often ill-conditioned, with the severity of the ill-conditioning depending on the boundary condition used

and the type and location of the material inside the cavity [9]. There are numerous techniques available to solve systems of linear equations, some of these include factorising the coefficient matrix into lower and upper triangular matrices (LU), bi-conjugate gradient stabilised (biCGstab), quasi-minimal residual (QMR) and generalised minimal residual (GMRES). Depending on the solver used, preconditioning to reduce the condition number of the coefficient matrix may be required [17].

In the solution strategy of the Helmholtz equation, adaptive preconditioners are sometimes needed to cater for the changing frequencies and the different material interfaces. To obtain electric fields and thereafter power distributions, it is not enough to use a single (so-called dominant) frequency to obtain the solution in the frequency-domain, but rather, it may be necessary to compute energy levels that consist of a number of neighbouring frequencies around the dominant mode that approximate the three electric field components in the frequency domain.

The hybrid method [6] aims to eliminate the restrictions of the FD-TD method and the Helmholtz equation solver. To do this, the hybrid method takes advantage of the sparsity of the nodes in free-space and uses problem decomposition to reduce the condition number of the matrix in the domain of the load. A cell-centred Finite-Volume Time-Domain (ccFV-TD) solver that works well in free-space is used to obtain the electric and magnetic fields outside the load (see Figure 6.2) on a relatively coarse mesh. The time-domain electric field distribution solution is converted to the frequency-domain electric fields at the load boundary via the Discrete Fourier Transform (DFT). This information is obtained not only at a single frequency, but rather for a set of frequencies in the neighbourhood of the dominant frequency. Once the interface boundary information is computed, the Helmholtz equation is solved a number of times with the generated boundary conditions at the various discrete frequencies.

The resulting system of linear equations is no longer as ill-conditioned as a system that resolves the whole domain (*i.e.* free-space and load), because only the load has been discretised and a system of linear equations is generated with Dirichlet interface boundary conditions between the free-space and the material with acceptable accuracy. Subsequently, a smaller system of linear equations is formulated that converges to a stable solution more rapidly than a system that is representative of the domain of free space and the load together. As a result, the hybrid method for multi-mode cavity structures yields a technique that provides efficient generation of load boundary information, since the time-domain solver used is applied on a coarse grid, and hence, the solution of the electric field is computed rapidly.

This paper firstly consists of an outline of the hybrid method, followed by an outline of the boundary condition treatment, after which a number of case studies are presented in the results section. Finally, the main conclusions of the research work are summarised. The reasearch work shows that the hybrid method is accurate and highly efficient for predicting the power distribution inside lossy materials during microwave heating processes. The findings are validated for two waveguide case studies and two different industrial case studies using thermal images.

## 6.2 Outline of the Hybrid Method

The aim of the numerical scheme is to resolve the power distribution inside the load, so that the power can be coupled (if so desired) with the forced heat equation to obtain the temperature distribution. The scope of this paper is to demonstrate that the previously published hybrid method can be used successfully for a waveguide and multi-mode cavity to predict the power distribution in a lossy

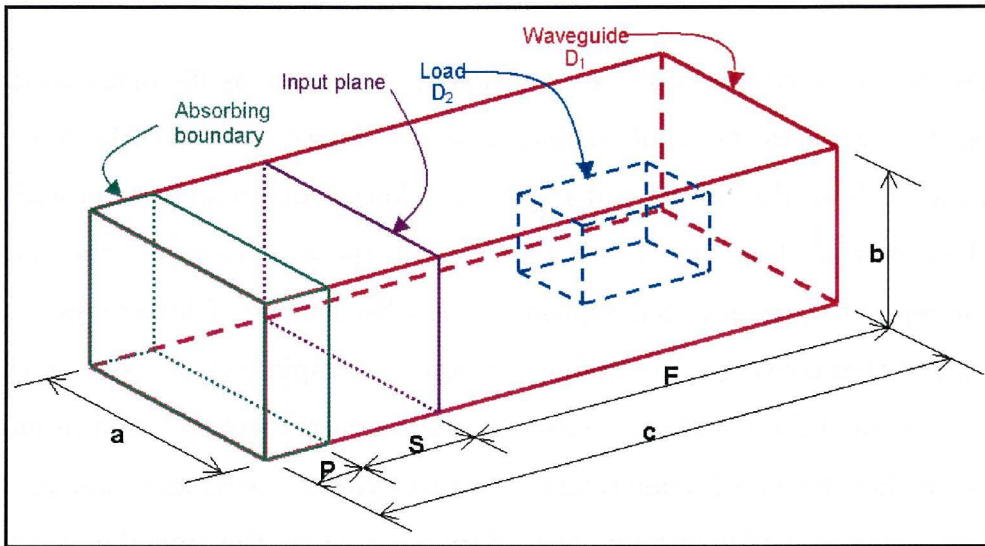


Figure 6.1: The loaded waveguide and dimensions.

load located inside the full field region of the guide and the cavity.

Figure 6.1 illustrates the waveguide and location of the load. In the figure,  $a$ ,  $b$  and  $c$  are the dimensions of the rectangular waveguide. The cavity problem (see Figure 6.2) is an extension of the waveguide problem, where another larger rectangular section has been attached to the end of the waveguide.  $P$  is the size of the Perfectly Matched Layer (PML) boundary region that absorbs any impinging waves in the Scattered ( $S$ ) field region of the guide that may be reflected from the Full ( $F$ ) field region. The waveguide is decomposed into two domains, namely  $D_1$ , which is the free-space component, and  $D_2$  representing the load. In Figure 6.1, the input plane propagates a  $TE_{10}$  electromagnetic wave at  $2.45GHz$  into the full field region of the guide.

The Hybrid method is a numerical technique that comprises the solution of two decoupled problems, which are referred to as the exterior and the interior problems. The exterior problem requires the time-dependent Maxwell's equations to be solved to approximate the fields inside the free-space ( $D_1$ ) and on

the material interface. Whereas, the interior problem requires the solution to the electric Helmholtz equation and thereafter the power distribution inside the load ( $D_2$ ). The following two sections outline the exterior and interior problem methodologies in detail.

### 6.2.1 Exterior Problem - Maxwell's Equations

In the free space component ( $D_1$ ), the electric and magnetic fields are governed by the Maxwell's equations [4]. The time-dependent equations are represented as:

$$\begin{aligned}\nabla \times \mathbf{E} &= -\frac{\partial \mathbf{B}}{\partial t}, & \nabla \times \mathbf{B} &= \frac{\partial \mathbf{D}}{\partial t} + \mathbf{J}, \\ \mathbf{B} &= \mu \mathbf{H}, & \mathbf{D} &= \epsilon \mathbf{E}, & \mathbf{J} &= \sigma \mathbf{E}, & \epsilon &= \epsilon_0 \epsilon', & \sigma &= \omega \epsilon_0 \epsilon''.\end{aligned}\quad (6.1)$$

In this paper, (6.1) is solved using a cell-centred finite-volume time-domain numerical solver. This time-marching scheme uses a Leapfrog time stepping technique and for the finer details of the implementation the reader is referred to [18]. The second order in space cell-centred Leapfrog time-marching algorithm at a point is given as:

$$\mathbf{H}_p^{n+\frac{1}{2}} = \mathbf{H}_p^{n-\frac{1}{2}} - \frac{\Delta t}{\mu_0 \Delta V} \sum_{f \in \zeta_p} (\mathbf{n} \times \mathbf{E})_f^n \Delta S_f, \quad (6.2)$$

$$\mathbf{E}_p^{n+1} = \frac{2\epsilon - \sigma \Delta t}{2\epsilon + \sigma \Delta t} \mathbf{E}_p^n + \frac{2\Delta t}{(2\epsilon + \sigma \Delta t) \Delta V} \sum_{f \in \zeta_p} (\mathbf{n} \times \mathbf{H})_f^{n+\frac{1}{2}} \Delta S_f. \quad (6.3)$$

In (6.2) and (6.3)  $p$  represents the  $p^{th}$  cell inside the computational domain,  $f$  is a cell face unknown of cell  $p$  and  $\zeta_p$  is the set of faces that constitute the  $p^{th}$  cell.  $\Delta t$ ,  $\Delta S_f$  and  $\Delta V$  are the time step of the numerical scheme, surface area of face  $f$  and volume of cell  $p$ , respectively. Equations (6.2) and (6.3) are applied to solve for the electric and magnetic field components inside the free-space part of the waveguide. These equations purely simulate the free-space

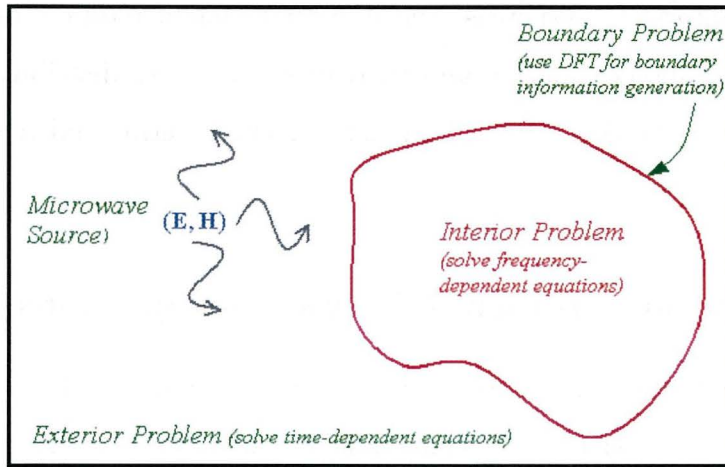


Figure 6.2: Solution methodology for the interior problem.

electromagnetic behaviour, and are used only to generate the boundary condition information, which is then transformed to the frequency domain via the Discrete Fourier Transform [19] at material interfaces:

$$\phi^k = \int_{-\infty}^{+\infty} \mathbf{E}(t) e^{2\pi i f_k t} dt \approx \sum_{n=0}^{N-1} \mathbf{E}^n e^{\frac{2\pi i f_k t_n}{N}} \Delta t = \Delta t \sum_{n=0}^{N-1} \mathbf{E}^n e^{\frac{2\pi i k n}{N}}, \quad (6.4)$$

where,

$$f_k = \frac{k}{N \Delta t}, \quad \phi^k = \phi(f_k), \quad t_n = n \Delta t, \quad k = -\frac{N}{2}, \dots, \frac{N}{2}. \quad (6.5)$$

In (6.4) and (6.5),  $\mathbf{E}^n$  is the discrete set of electric and magnetic field components as computed by (6.2) and (6.3). The DFT algorithm is used to transform time-domain electric field values that lie on the interface between the material and free-space. In the frequency domain,  $\phi(f_k)$  is the electric and magnetic field at the  $f_k$  frequency. The load and boundary data generation are illustrated in Figure 6.2.

### 6.2.2 Interior Problem - Helmholtz Equation

Inside the material depicted in Figure 6.2 the Helmholtz equation is solved at a discrete frequency. The Helmholtz equation is developed and formulated from the time-harmonic electromagnetic equations:

$$\nabla \times \xi = (\sigma + i\omega\varepsilon)\phi, \quad (6.6)$$

$$\nabla \times \phi = -i\omega\mu\xi. \quad (6.7)$$

In (6.6) and (6.7)  $\xi \equiv H_i(f)$  and  $\phi \equiv E_i(f)$ , where  $i = x, y, z$  denote the components of the magnetic and electric fields, respectively. By taking the curl of both equations and rearranging, the following Helmholtz equation is obtained for the electric fields:

$$\nabla^2\phi + \kappa^2\phi = 0, \quad (6.8)$$

$$\kappa^2 = \mu_0\omega(\omega\varepsilon - \sigma i).$$

Equation (6.8) satisfies the divergence criteria [4]:

$$\varepsilon\nabla \cdot \phi = 0. \quad (6.9)$$

The discretisation of the Helmholtz equation (6.6) is straightforward, and usually a second-order scheme is adapted to form the implicit system of linear equations. First, the Helmholtz equation from (6.8) is rewritten as:

$$\nabla \cdot (\nabla\phi) + \kappa^2\phi = 0. \quad (6.10)$$

For a finite-volume discretisation strategy, (6.10) is integrated over the volume of the cell to give:

$$\iiint_v \nabla \cdot (\nabla\phi) \partial v + \Delta V \kappa^2 \bar{\phi} = 0, \quad (6.11)$$

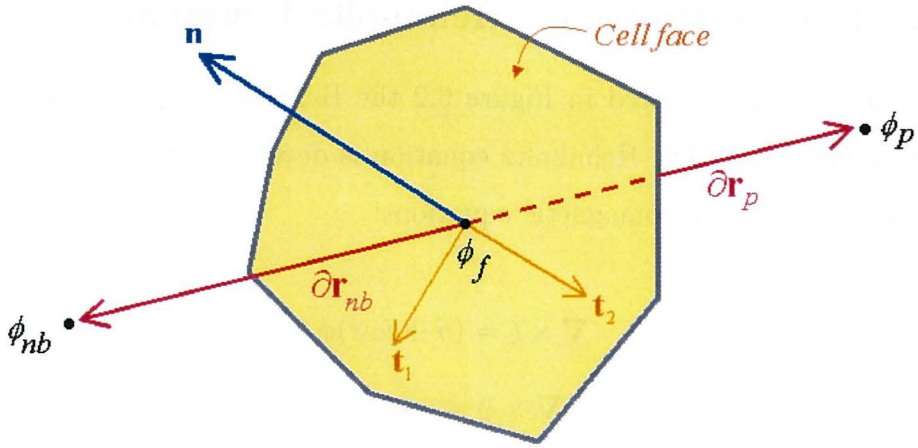


Figure 6.3: A finite-volume cell face of a particular cell  $p$ .

where,  $\Delta V$  is the volume of the particular cell. In (6.11),  $\bar{\phi}$  is the average electric field for cell  $p$ :

$$\bar{\phi} = \frac{1}{\Delta V} \iiint_v \phi \partial V, \quad (6.12)$$

which is approximated as  $\bar{\phi} \simeq \phi_p$ . Hence, the discrete analogue of the volume integral (6.11) can be rewritten for cell  $p$  according to the following expression:

$$\sum_{f \in \zeta_p} (\nabla \phi \cdot \mathbf{n})_f \Delta S_f + \Delta V \kappa^2 \phi_p = 0. \quad (6.13)$$

In (6.13)  $\mathbf{n}$  is the unit outward normal on cell face  $f$ ,  $\zeta_p$  represents the set of faces that constitute cell  $p$  and the term  $\nabla \phi \cdot \mathbf{n}$  is approximated on each of the faces of cell  $p$ . The mid-point integration rule was adopted for the integral approximation in (6.13), which is known to be second order accurate when the value of the unknown  $(\nabla \phi \cdot \mathbf{n})_f$  is computed exactly. As a consequence of this limitation, an estimate of  $\nabla \phi_f$  is sought on the cell face with high accuracy to enable the scheme to retain the second order spatial discretisation. On a Cartesian mesh, (6.12) is equivalent to the standard discretisation using the Taylor approximations for  $\nabla^2 \phi$  in (6.8). Figure 6.4 illustrates a particular face of the

finite-volume cell for a component of the electric field  $\phi$ . In the figure,  $\mathbf{n}$  is the unit outward normal to face  $f$ , and  $\mathbf{t}_1$  and  $\mathbf{t}_2$  are unit vectors lying on that face. The set of vectors  $\{\mathbf{n}, \mathbf{t}_1, \mathbf{t}_2\}$  forms an orthonormal basis for  $\mathbb{R}^3$ . The vectors emanating from face  $f$  to  $\phi_p$  and  $\phi_{nb}$  are denoted  $\partial\mathbf{r}_p$  and  $\partial\mathbf{r}_{nb}$ , respectively. In (6.13),  $\nabla\phi_f \cdot \mathbf{n}$  has to be approximated for a component of the electric field right on the cell face. To achieve this, the Taylor series is used to expand both  $\phi_p$  and  $\phi_{nb}$  about  $f$ , which are written as:

$$\phi_p = \phi_f + \partial\mathbf{r}_p \cdot \nabla\phi_f + \frac{1}{2}\partial\mathbf{r}_p^T \mathcal{H} \partial\mathbf{r}_p + \dots \quad (6.14)$$

$$\phi_{nb} = \phi_f + \partial\mathbf{r}_{nb} \cdot \nabla\phi_f + \frac{1}{2}\partial\mathbf{r}_{nb}^T \mathcal{H} \partial\mathbf{r}_{nb} + \dots \quad (6.15)$$

where,  $\mathcal{H}$  is the Hessian matrix for  $\phi$  evaluated at the cell face. Subtracting (6.15) from (6.14) and letting  $\partial\mathbf{r} = \partial\mathbf{r}_{nb} - \partial\mathbf{r}_p$ , the following equation is obtained:

$$\phi_{nb} - \phi_p = \partial\mathbf{r} \cdot \nabla\phi_f + \frac{1}{2} [\partial\mathbf{r}_{nb}^T \mathcal{H} \partial\mathbf{r}_{nb} - \partial\mathbf{r}_p^T \mathcal{H} \partial\mathbf{r}_p] + \dots \quad (6.16)$$

Now, (6.16) can be rearranging to obtain the following equation:

$$\partial\mathbf{r} \cdot \nabla\phi_f \simeq (\phi_{nb} - \phi_p) - \epsilon_f, \quad (6.17)$$

where,

$$\epsilon_f = \frac{1}{2} [\partial\mathbf{r}_{nb}^T \mathcal{H} \partial\mathbf{r}_{nb} - \partial\mathbf{r}_p^T \mathcal{H} \partial\mathbf{r}_p].$$

To obtain  $\nabla\phi \cdot \mathbf{n}$  at the face in (6.13),  $\partial\mathbf{r}$  has to be resolved in terms of the orthonormal basis vectors in  $\mathbb{R}^3$ . Therefore,  $\partial\mathbf{r}$  is represented as:

$$\partial\mathbf{r} = (\partial\mathbf{r} \cdot \mathbf{n})\mathbf{n} + (\partial\mathbf{r} \cdot \mathbf{t}_1)\mathbf{t}_1 + (\partial\mathbf{r} \cdot \mathbf{t}_2)\mathbf{t}_2. \quad (6.18)$$

In (6.18) by operating on both sides with the dot product of  $\nabla\phi_f$  and letting  $\alpha_1 = \partial\mathbf{r} \cdot \mathbf{n}$ ,  $\alpha_2 = \partial\mathbf{r} \cdot \mathbf{t}_1$  and  $\alpha_3 = \partial\mathbf{r} \cdot \mathbf{t}_2$  the following expression is obtained:

$$\nabla \phi_f \cdot \partial \mathbf{r} = \alpha_1 \nabla \phi_f \cdot \mathbf{n} + \alpha_2 \nabla \phi_f \cdot \mathbf{t}_1 + \alpha_3 \nabla \phi_f \cdot \mathbf{t}_2. \quad (6.19)$$

Rearranging (6.19) for the  $\nabla \phi_f \cdot \mathbf{n}$  term and substituting (6.17) gives the following expression:

$$\nabla \phi_f \cdot \mathbf{n} = \frac{1}{\alpha_1} \left[ \underbrace{(\phi_{nb} - \phi_p)}_1 - \underbrace{\epsilon_f - \alpha_2(\nabla \phi_f \cdot \mathbf{t}_1) - \alpha_3(\nabla \phi_f \cdot \mathbf{t}_2)}_2 \right]. \quad (6.20)$$

In (6.19) term (1) is treated implicitly while term (2) is treated explicitly. It should be noted that the inclusion of term (2) in equation (6.20) for the gradient approximation introduces a non-linearity in (6.13) that requires special treatment to obtain the solution for  $\phi$ . Generally, a Quasi-Newton approach is used to solve the non-linear system. In the case of Cartesian meshes, the inclusion of term (2) is not necessary. The approximation in (6.20) is used in (6.13) for the  $(\nabla \phi \cdot \mathbf{n})_f$  term. To evaluate the right hand side in equation (6.20), a least squares approach is adopted to determine  $\nabla \phi_f$  and the entries of the Hessian matrix for estimating the correction  $\epsilon_f$  [20].

When all the the cells in the computational domain have been visited with (6.13), the discretisation of the Helmholtz equation yields a system of linear equations for a component of the electric field  $\phi$  at frequency  $k$  ( $\phi^k$ ), which is cast into matrix form as:

$$\mathbf{A} \phi^k = \mathbf{b}. \quad (6.21)$$

In (6.21),  $\mathbf{A}$  is the sparse coefficient matrix according to the discretisation of (6.6), and  $\mathbf{b}$  is the right hand vector containing the boundary information generated using (6.4) with the time-domain data obtained from (6.3). Equation (6.21) is solved three times for each frequency, because  $\phi^k$  representes the three components of the electric field (*i.e.*  $\phi^k \leftarrow \phi_x, \phi_y, \phi_z$ ). Once the electric field

components in (6.21) have been obtained, the power is computed according to the following relationship:

$$P_p = \frac{\sigma_p}{2} \phi_p^2(f_k) = \frac{\sigma_p}{2} (\phi_x^2 + \phi_y^2 + \phi_z^2) = \frac{\sigma_p \phi_x^2}{2} + \frac{\sigma_p \phi_y^2}{2} + \frac{\sigma_p \phi_z^2}{2}. \quad (6.22)$$

To obtain the power ( $P_p$ ) at a particular node location  $p$ , (6.22) is computed after the electric field components have been obtained from (6.21). The solution to (6.21) is performed using Quasi-GMRES [21].

### Algorithm 1 (Quasi-GMRES)

```
r0 = b - Ax0,  β = ||r0||2,  v1 = r0/β,
```

```
for j = 1 to m
```

```
    w = Avj
```

```
    for i = max{1, j - l + 1} to j
```

```
        hij = ⟨w, vi⟩
```

```
        w = w - hijvj
```

```
    end for
```

```
    h_{j+1,j} = ||w||2
```

```
    if h_{j+1,j} = 0
```

```
        m = j;  break
```

```
    end if
```

```
    v_{j+1} = w/h_{j+1,j}
```

```
end for
```

```
y_m = min_y ||βe1 - H_my||2
```

```
x_m = x0 + V_m y_m
```

Algorithm 1 uses the modified Gram-Schmidt process for the orthogonalisation of the sub-space vectors within the  $i$  loop. In Quasi-GMRES, not all of the previously generated sub-space vectors were used in the reorthogonalisations, but rather, only a finite number ( $l$ ) of them were used in the Gram-Schmidt process to obtain the next sub-space vector. As a consequence, as more and more sub-space vectors are computed, the amount of time taken to obtain the next best solution to the problem is bounded. For this problem it was found that a minimum of five reorthogonalisations ( $l = 5$ ) of the generated sub-space vectors were required. The Quasi-GMRES method took considerably less time to compute than

the standard GMRES solution strategy (where,  $l = m$ ). The computations here were investigated also using a set of ten sub-space vectors for the reorthogonalisations, but no significant difference was observed, other than having to generate approximately 10% less vectors to reach the desired accuracy. The advantage of Quasi-GMRES over GMRES in this application is that the upper Hessenberg matrix ( $\bar{H}$ ) becomes banded. As a consequence, the least-squares problem is solved also more rapidly. For the finer details of GMRES and Quasi-GMRES, the reader is referred to [17].

### 6.3 Boundary Conditions

In the previous sections the Hybrid method was discussed in detail. In this section the boundary conditions for the free-space conducting wall, input-plane, perfectly matched layer and material interface are formulated.

In the free space region ( $D_1$ ) of the waveguide, a  $2.45GHz$   $TE_{10}$  electromagnetic wave is generated according to:

$$E_y^I = \text{Gauss}(t) E_0 \sin\left(\frac{\pi x}{a}\right) \cos(\omega t - \beta_0 z_0), \quad (6.23)$$

$$H_x^I = -\text{Gauss}(t) \frac{\beta_0}{\omega \mu_0} E_0 \sin\left(\frac{\pi x}{a}\right) \cos(\omega t - \beta_0 z_0), \quad (6.24)$$

$$H_z^I = -\text{Gauss}(t) \frac{\pi}{\omega \mu_0 a} E_0 \cos\left(\frac{\pi x}{a}\right) \sin(\omega t - \beta_0 z_0), \quad (6.25)$$

$$\beta_0 = \sqrt{\omega^2 \mu_0 \epsilon_0 - \left(\frac{\pi}{a}\right)^2}, \quad \text{Gauss}(t) = \begin{cases} e^{-\frac{(t-3T)^2}{T^2}} & , t \leq 3T \\ 1 & , t > 3T \end{cases}.$$

The Gaussian function in (6.23-6.25) is used to smoothen the incident waves so that the noise due to the input plane is minimised [5]. At the input plane the fields are implemented according to [18].

Generally for this situation, the incident fields propagate into the full field region of the guide (and into the cavity), after which they are reflected back from the material and cavity walls into the scattered field region. Any reflected waves that impinge into the scattered region must be absorbed and here, a perfectly matched layer absorbing boundary condition is implemented [14] to achieve this. The implementation details of the Petropoulos PML with the SLF Maxwell's equations discretisation in the framework of a finite-volume methodology for a waveguide is derived in [18]. It should be noted that since this study investigates the Hybrid method for a generalised cavity problem, the Petropoulos PML is somewhat different to [18]. In this case, not only the previously implemented PML is used, but also, another PML region is created to ensure that at the input plane only the true  $TE_{10}$  fields exist (*i.e.*  $H_x$ ,  $H_z$ , and  $E_y$ ). The formula for the PML region is given by the following equation [18]:

$$\mathbf{H}_p^{n+\frac{1}{2}} = \mathbf{H}_p^{n-\frac{1}{2}} - \left( \frac{2\mu_0\Delta t + \sigma^*\Delta t^2}{2\mu_0^2\Delta V} \right) \sum_{f \in \zeta_p} (\mathbf{n} \times \mathbf{E})_f^n \Delta S_f - \frac{\sigma^*\Delta t^2}{\mu_0^2\Delta V} \mathbf{F}_p^{n-1}, \quad (6.26)$$

$$\mathbf{F}_p^n = \mathbf{F}_p^{n-1} + \sum_{f \in \zeta_p} (\mathbf{n} \times \mathbf{E})_f^n \Delta S_f.$$

In (6.26),  $\sigma^* = \frac{\mu_0}{\varepsilon_0}\sigma$  is chosen to ensure that as the waves impinge further into the perfectly matched layer the absorptivity ( $\sigma$ ) of the material increases [14]. Similarly, the normal component of the electric field within the PML region is defined as:

$$\mathbf{E}_p^{n+1} = \mathbf{E}_p^n + \left( \frac{2\varepsilon\Delta t + \sigma\Delta t^2}{2\varepsilon^2\Delta V} \right) \sum_{f \in \zeta_p} (\mathbf{n} \times \mathbf{H})_f^{n+\frac{1}{2}} + \frac{\sigma\Delta t^2}{\varepsilon^2\Delta V} \mathbf{G}_p^{n-\frac{1}{2}}, \quad (6.27)$$

$$\mathbf{G}_p^{n+\frac{1}{2}} = \mathbf{G}_p^{n-\frac{1}{2}} + \sum_{f \in \zeta_p} (\mathbf{n} \times \mathbf{H})_f^{n+\frac{1}{2}} \Delta S_f.$$

In this work, the second PML is introduced in the full field region of the waveguide to absorb the  $y$ -component of the magnetic field ( $H_y$ ), the  $x$ -component of the electric field ( $E_x$ ) and the  $z$ -component of the electric field ( $E_z$ ). These fields must be absorbed before they reflect back into the scattered field region of the waveguide, otherwise the physics of the problem would not be satisfied. The implementation of the second PML in the full field is the same as the first PML, but the components that are absorbed are different. The second PML region has the same dimension as the first PML, however it is located right at the end of the waveguide and near the cavity. This second PML allows the decoupling of the modes, and enables the propagation of only the  $TE_{10}$  mode, whilst all other modes that may exist in the full field region of the guide are absorbed.

Material interface conditions must be satisfied as the waves inside the free-space ( $D_1$ ) propagate towards, and reflect and refract at the material interface ( $D_2$ ). The material boundary conditions are given as:

$$\mathbf{n} \times (\mathbf{E}_{nb} - \mathbf{E}_p) = \mathbf{0}, \quad (6.28)$$

$$\mathbf{n} \cdot (\mathbf{D}_{nb} - \mathbf{D}_p) = 0, \quad (6.29)$$

$$\mathbf{n} \times (\mathbf{H}_{nb} - \mathbf{H}_p) = \rho, \quad (6.30)$$

$$\mathbf{n} \cdot (\mathbf{B}_{nb} - \mathbf{B}_p) = 0. \quad (6.31)$$

In equations (6.28-6.31),  $\mathbf{n}$  is the unit outward normal to the interface between free-space and the load. For most microwave heating problems the media are dielectric materials, which are current free. Hence,  $\mu = \mu_0$  and  $\rho = 0$ , and equations (6.28-6.31) give that the magnetic fields are continuous inside the whole problem domain (*i.e.* through the interface of  $D_1$  and  $D_2$ ), and the electric fields are discontinuous at material or load interfaces. The jump across the material interface is treated as in [18].

For both the Maxwell's equations and the Helmholtz equation, perfectly conducting wall conditions have to be implemented. The only time this type of condition is not implemented in the Helmholtz equation, is when the material does not touch the walls of the waveguide or the cavity. Hence, the treatment of the conducting wall boundary is crucial to both the time-domain and frequency domain solvers. At a perfectly conducting wall, the following criteria have to be satisfied:

$$\mathbf{E} \times \mathbf{n} = 0, \quad (6.32)$$

$$\mathbf{H} \cdot \mathbf{n} = 0. \quad (6.33)$$

According to (6.32) and (6.33), the tangential electric field and normal magnetic field components on a perfectly conducting wall are zero. The perfectly conducting wall conditions are implemented by creating spurious fields outside the free-space domain ( $D_1$ ) for the Maxwell's equation solver, and by catering for these in the discretisation for the Helmholtz equation solver [18].

## 6.4 Results

In this section, a number of different case studies are analysed and the simulation results are compared to either the FD-TD scheme or experimentally determined thermal images. Firstly, a fully loaded waveguide is analysed where the material is placed so that it fills the waveguide. These results will be presented for a single mode waveguide, where the material or load cross-sectionally fills the short-circuit end of the guide. In such a case only the  $y$ -component of the electric field, and the  $x$  and  $z$ -components of the magnetic field propagate.

Similarly to the first study, the second study concerns an inhomogeneously loaded waveguide, where the load half fills the cross-section of the waveguide and

touches the  $x - z$  plane perfectly conducting wall. The modes inside the guide are studied, and the power distribution computed from the Helmholtz equation is compared to the highly accurate solution obtained via the FD-TD scheme. Figure 6.1 exhibits the set-up for the different waveguide tests performed, whilst Figure 6.12 illustrates the cavity and corresponding dimensions for case studies 3 and 4, where the hybrid method is validated against thermal images obtained from industrial applications.

For the waveguide problems,  $a = 0.1\text{ m}$ ,  $b = 0.05\text{ m}$  and  $c = 0.4\text{ m}$ , while the PML region is  $P = 0.09\text{ m}$  deep and the input-plane is located at  $z_0 = 0.1\text{ m}$ . The location of the load will be given for the different case studies, along with the dielectric properties. In case studies 3 and 4, the dimensions for the waveguide, cavity and material are stated. The dielectric properties of the materials chosen in these case studies are indicative of lossy media, and hence, it is reasonable to assume that a large amount of the input energy is absorbed.

The power distribution is computed to compare the hybrid method with the FD-TD scheme. For the time and frequency domain comparisons, the power distribution is obtained in one of two ways. For the FD-TD solver, the power at a point  $p$  is computed as a time-averaged value [5]:

$$P_p = \frac{1}{T} \int_{nT}^{(n+1)T} \sigma_p \mathbf{E}_p^2(t) dt, \quad (6.34)$$

and for the hybrid method the power is computed according to (6.22). The difference between the two power computations lies in the representation of the electric field. All of the computations were performed on a dual processor PIII 1GHz desktop computer with 512MB of memory. Only one of the processors was used for the benchmark computations and the computational times quoted. The programs were written in the C/C++ programming language.

### 6.4.1 Case Study 1 - Fully Loaded Waveguide

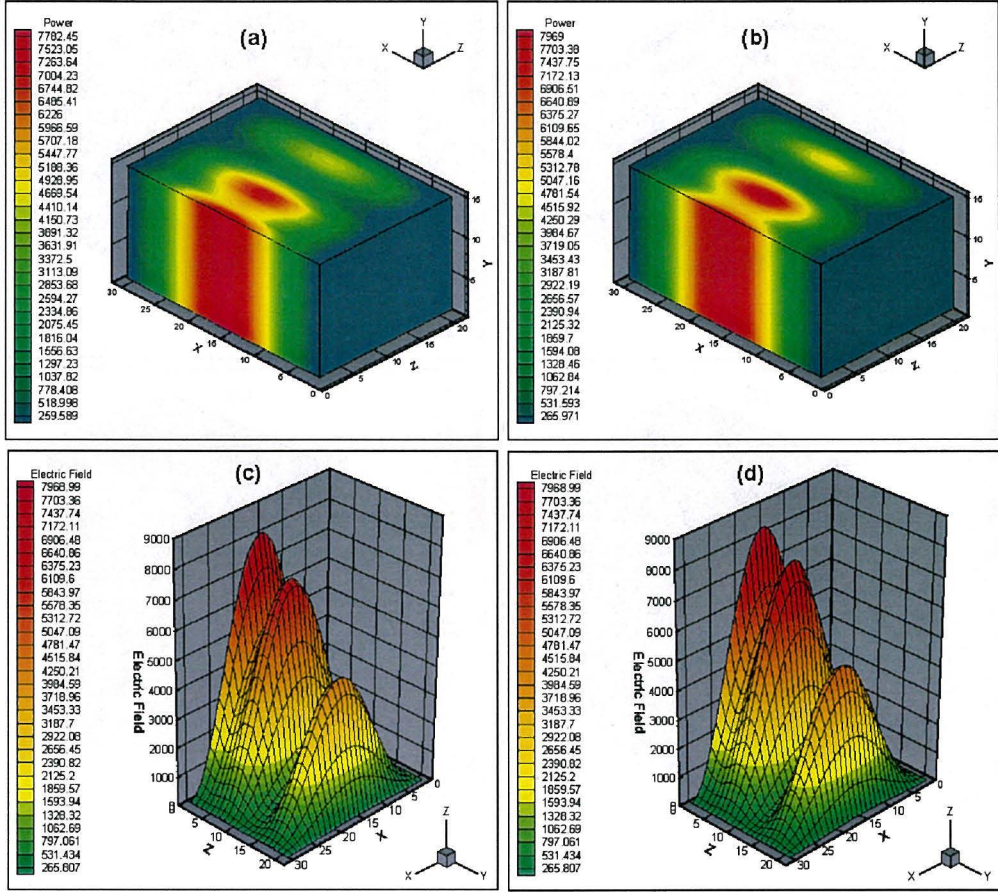


Figure 6.4: Case study 1. Illustration of the loaded waveguide with load comprising of  $30 \times 15 \times 20$  cells, (a) and (c) FD-TD power computation, (b) and (d) hybrid method power computation.

For the first case study, the average input power is set to  $P_{av\_in} = 500 W$  and the permittivity of the load is  $\varepsilon_r = 2 - \frac{1}{2}i$ . The electric field amplitude that is used to excite the incident plane (6.23-6.25) is computed according to [9]:

$$E_0 = \sqrt{\frac{2P_{av_{in}}\mu_0\omega}{\beta_0}}. \quad (6.35)$$

The material with dimension  $0.1 \times 0.05 \times 0.1 m^3$  is placed inside the waveguide, touching the short-circuit end, so that the material cross-section fills the

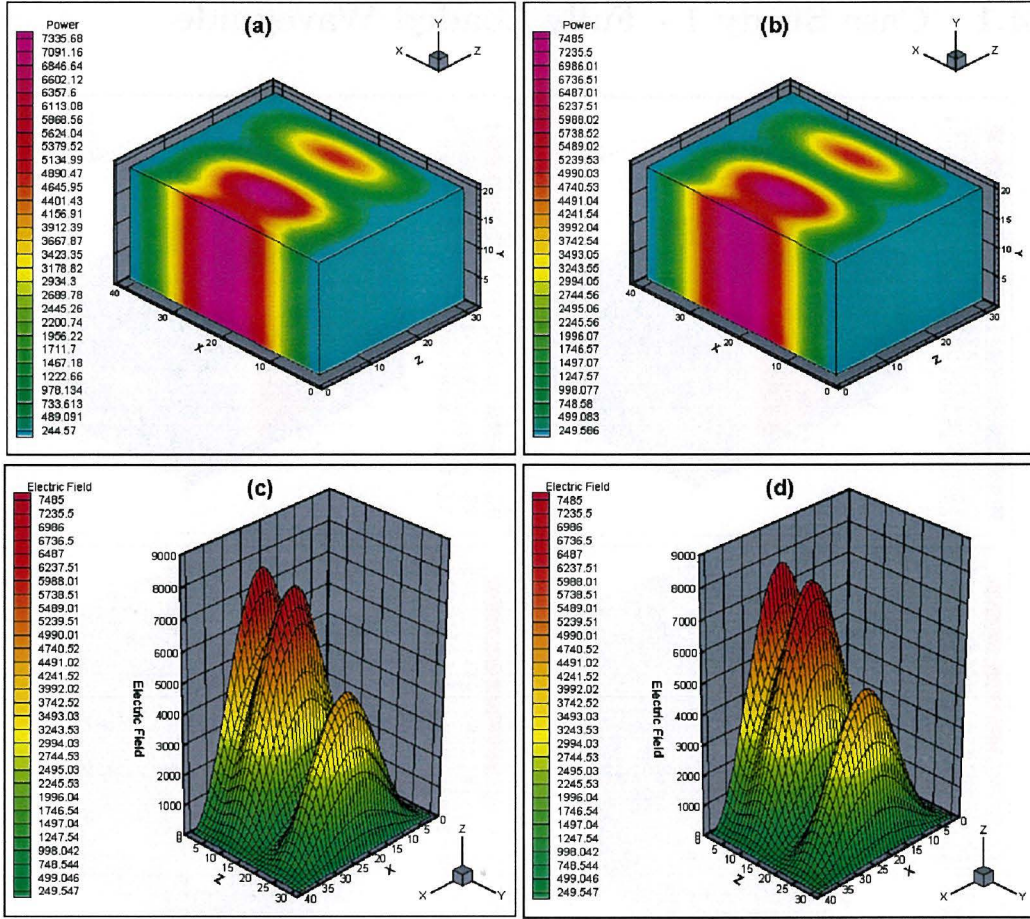


Figure 6.5: Case study 1. Illustration of the loaded waveguide with load comprising of  $40 \times 20 \times 30$  cells, (a) and (c) FD-TD power computation, (b) and (d) hybrid method power computation.

end of the full-field region of the guide. The standard boundary conditions are used as discussed in §6.3. The results have been computed for two different meshes; (a) the waveguide discretised into  $30 \times 15 \times 80 = 36\,000$  cells with the load comprising  $30 \times 15 \times 20 = 9\,000$  cells, and (b) the waveguide mesh consisting of  $40 \times 20 \times 120 = 96\,000$  cells for which the load comprises  $40 \times 20 \times 30 = 24\,000$  cells.

Figures 6.4 to 6.7 exhibit the findings of the first study. Figure 6.4 depicts the comparison of the power distribution when computed by the FD-TD scheme

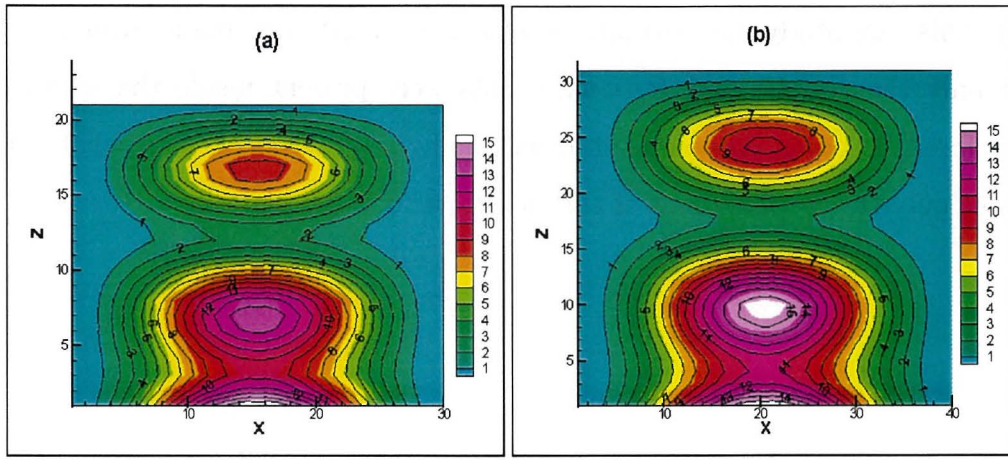


Figure 6.6: Case study 1. Contour (FD-TD) versus flood (hybrid method) plots. Figure (a) is load with  $30 \times 15 \times 20$  cells and (b) is load with  $40 \times 20 \times 30$  cells.

and the hybrid method for the coarser waveguide mesh (*i.e.*  $30 \times 15 \times 20$ ), and Figure 6.5 illustrates the results for the finer mesh ( $40 \times 20 \times 30$ ). For both meshes, Figures 6.6 and 6.7 illustrate the flood-contour plots and centre-line plots respectively, for the two methods.

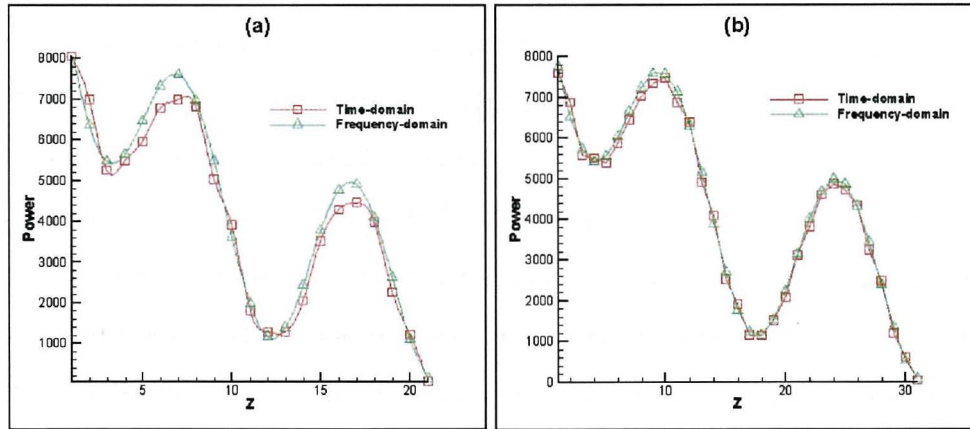


Figure 6.7: Case study 1. Line plots of FD-TD (green) against hybrid method (red). Figure (a) is load with  $30 \times 15 \times 20$  cells and (b) is load with  $40 \times 20 \times 30$  cells.

In this case study, the assumption of a  $TE_{10}$  mode was made, which implies that only the  $E_y$ ,  $H_x$  and  $H_z$  components were present inside the waveguide. Therefore, the power computation using the hybrid method is somewhat simplified, as only the  $y$ -component of the electric field is computed.

For this case study the results were obtained after eight periods have elapsed in the time-marching of the electric and magnetic fields when the hybrid method was used. Once the boundary information for the interior problem was established, the power from the frequency domain electric field solution was obtained at the  $2.45GHz$  frequency. For the coarse mesh, the domain of the load was discretised into 9 000 cells, while for the fine mesh the material was discretised into 24 000 cells. This meant that the matrix obtained from the Helmholtz equation stencil for both the coarse and fine meshes generated sparse matrices of dimension  $9\,000 \times 9\,000$  and  $24\,000 \times 24\,000$ , respectively. The solution to the Helmholtz equation was very rapid, requiring 92 and 116 basis vectors for the coarse and fine meshes respectively were generated for the GMRES solution. In the case of the FD-TD method to obtain a reasonably accurate solution, 14 periods were used to compute the electric and magnetic fields, out of which 2 periods were used to time-average the electric field for the power computations, whereas 8 periods were used for the hybrid method. As a consequence, the hybrid method for the waveguide problem is marginally quicker than the FD-TD scheme. Real gains are observed with the cavity problems, and these are outlined in the following three case studies. From Figures 6.6 and 6.7 it can be seen that the main difference between the coarse and fine meshes is in the amplitude of the waves inside the material, and the phase of the waves are in agreement.

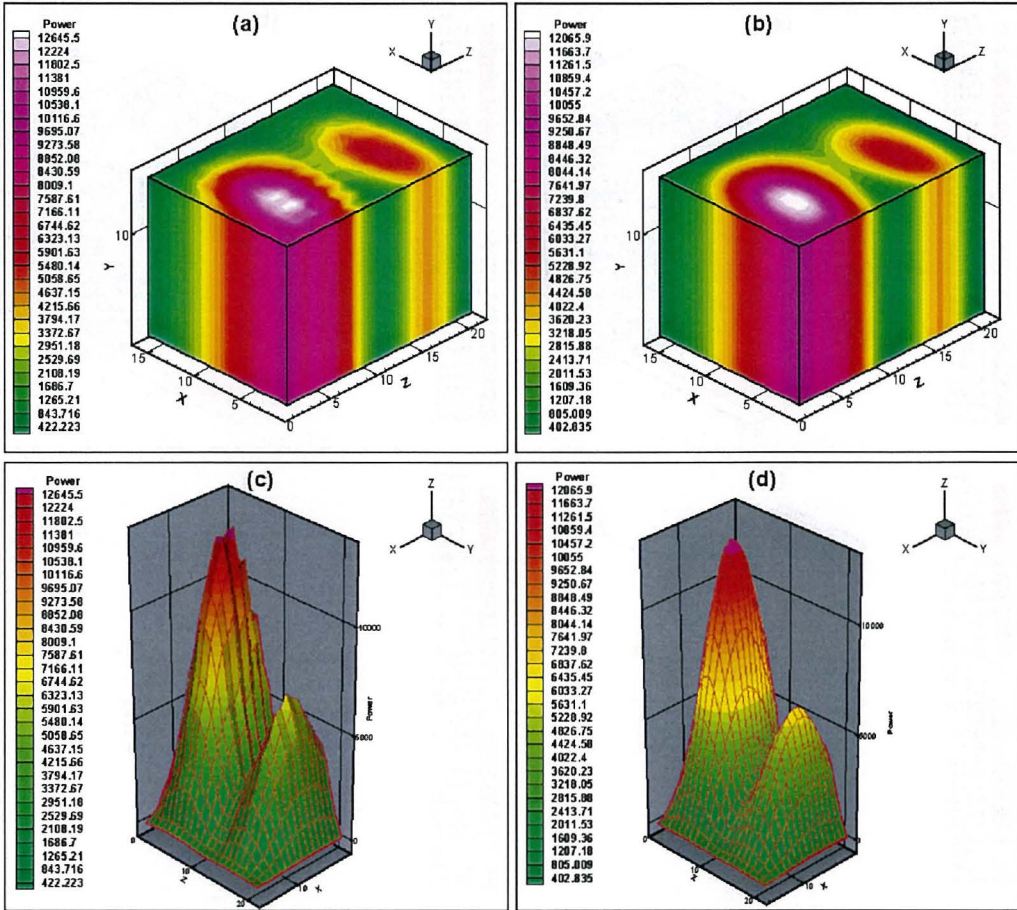


Figure 6.8: Case study 2. Illustration of the loaded waveguide with load comprising of  $15 \times 15 \times 20$  cells, (a) and (c) FD-TD power computation, (b) and (d) hybrid method power computation.

#### 6.4.2 Case Study 2 - Semi Loaded Waveguide

This case study is very similar to the first problem, however in this case the material has been cut in half, having dimension  $0.05 \times 0.05 \times 0.1 m^3$ . The material is placed against the short-circuit end of the waveguide and pushed to one side (see Figure 6.1). The domain of the waveguide has been discretised using the same grid as before, where the coarse mesh consists of  $15 \times 15 \times 20$  cells and the fine mesh consists of  $20 \times 20 \times 30$  cells for the load.

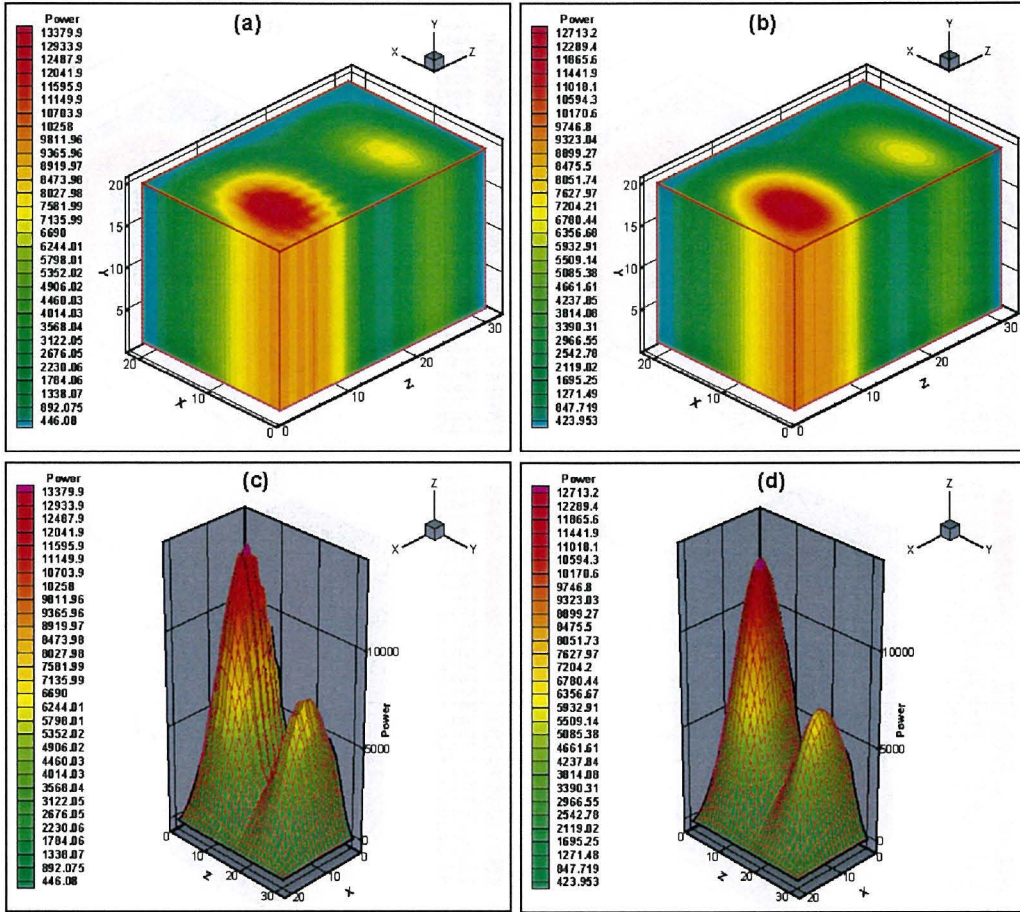


Figure 6.9: Case study 2. Illustration of the loaded waveguide with load comprising of  $20 \times 20 \times 30$  cells, (a) and (c) FD-TD power computation, (b) and (d) hybrid method power computation.

As for the first case study in §6.4.1, Figures 6.8 and 6.9 exhibit the power computations determined from the FD-TD and hybrid methods. The results are compared on both the coarse and fine meshes. In Figure 6.10 the flood versus contour plots are given for the semi-loaded waveguide. The final illustration given in Figure 6.11 is the centre-line plot of the power distribution computed using the hybrid method when compared to FD-TD. With the hybrid method the resultant numerical solutions tend to be smooth, due to the implicit nature of the solution strategy inside the material.

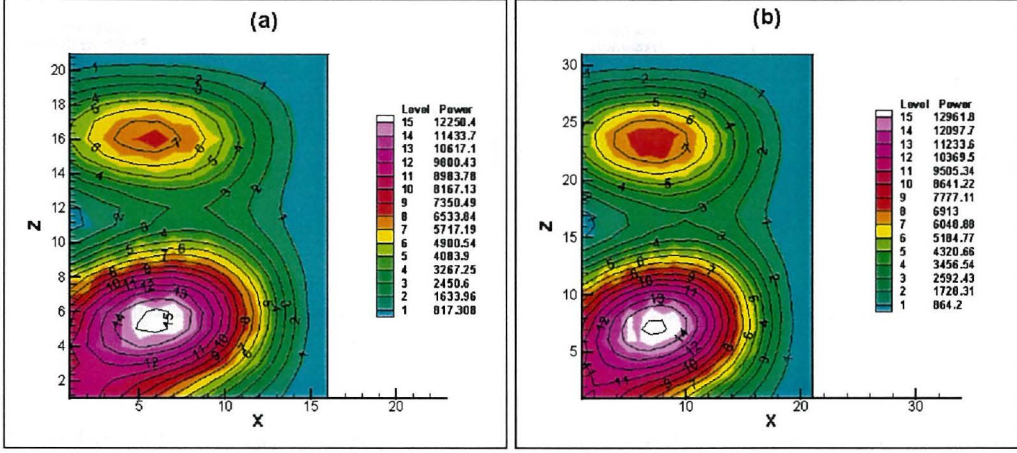


Figure 6.10: Case study 2. Contour (FD-TD) versus flood (hybrid method) plots.  
Figure (a) is load with  $15 \times 15 \times 20$  cells and (b) is load with  $20 \times 20 \times 30$  cells.

Unlike in the previous case study (see §6.4.1), here all field components ( $H_x, H_y, H_z, E_x, E_y, E_z$ ) have been computed and from the  $(E_x, E_y, E_z)$  field components the power distribution was obtained. It can be seen that when the waveguide is loaded at the short-circuit end, the results are in good agreement with the classical FD-TD methodology.

In the waveguide case studies, the computational effort required to compute the power distribution using the hybrid method is similar to that of the FD-TD scheme. Here the grids were chosen to ensure that the FD-TD scheme was stable and provided reasonable solutions. The dimension of the coefficient matrix obtained using the Helmholtz equation discretisation in the hybrid method was  $4500 \times 4500$  for the coarse mesh and  $12000 \times 12000$  for the fine mesh. In this case, 106 and 132 respective sub-space vectors were generated for the coarse and fine meshes to obtain the desired level of accuracy in the Helmholtz equation solution strategy. The same number of periods were run for both the FD-TD and hybrid methods as with case study 1. Moreover, the hybrid method produces results

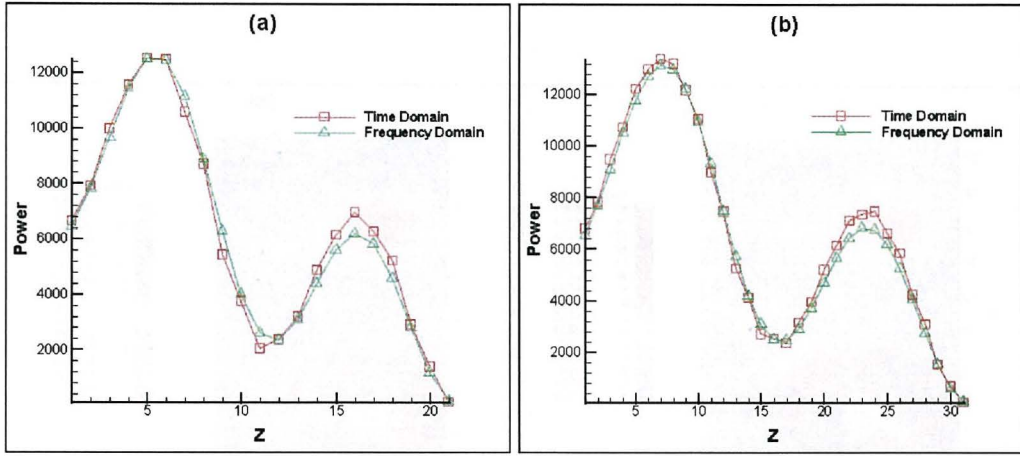


Figure 6.11: Case study 2. Line plots of FD-TD (green) against hybrid method (red). Figure (a) is load with  $15 \times 15 \times 20$  cells and (b) is load with  $20 \times 20 \times 30$  cells.

which are very accurate compared to the FD-TD method, and also, smooth due to the implicit nature of the scheme. The FD-TD simulations required twelve periods before the power distribution was obtained. The waveguide studies provide a benchmark for the hybrid method, and the following two case studies demonstrate the hybrid method using coarser grids on more realistic cavity microwave heating problems.

### 6.4.3 Case Study 3 - Mashed Potato

In this case study a cavity is attached to the short circuit end of the waveguide shown in Figure 6.1. The waveguide has dimensions  $0.086 \times 0.043 \times 0.16125 m^3$  and the cavity has dimensions  $0.391 \times 0.292 \times 0.3 m^3$ . The waveguide is attached to the top of the cavity as illustrated in Figure 6.12. The centre-line of the waveguide lines up with the centre-line of the cavity. The mashed potato is located in the centre at the bottom of the cavity and has dimensions  $0.21 \times 0.09 \times 0.03 m^3$ . According to Figure 6.12, the following parameters were used  $a_l = a_r$ ,  $a_m = 0.21 m$ ,  $b_l = b_r$ ,  $b_m = 0.09 m$ ,  $c_l = 0 m$  and  $c_m = 0.03 m$ . It is assumed that the di-

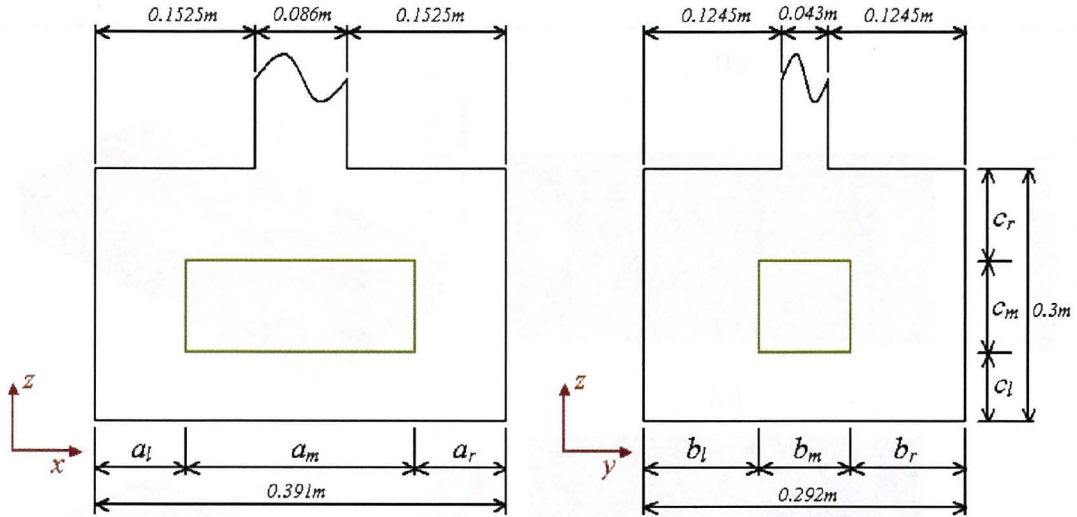


Figure 6.12: The outline of the cavity problem.

electric property of the mashed potato is constant throughout, and is given as  $\epsilon_r = 65 - 20i$ . From the permittivity of this material it can be observed that it is lossy ( $\epsilon'' = 20$ ) and microwaves will have a high phase change at the material interface ( $\epsilon' = 65$ ).

The simulation results for this case study are graphically illustrated in Figure 6.13. The thermal image [22] of the top surface of the mashed potato is given in Figure 6.13(a). Figure 6.13(b) illustrates the time-averaged electric field in the free-space component of the apparatus. Figures 6.13(c) and 6.13(d) represent the results computed by the hybrid method at the surface and the middle of the block.

In this and the following case study, the power distribution inside the material has been illustrated, and compared directly to the thermal images. It should be noted that the power distribution is representative of the energy delivered to the material, and this energy will then manifest as dissipated heat. Heating will therefore occur in high energy areas. Due to the nature of the heating and the thermal material properties, the heat distribution is more dissipative and is

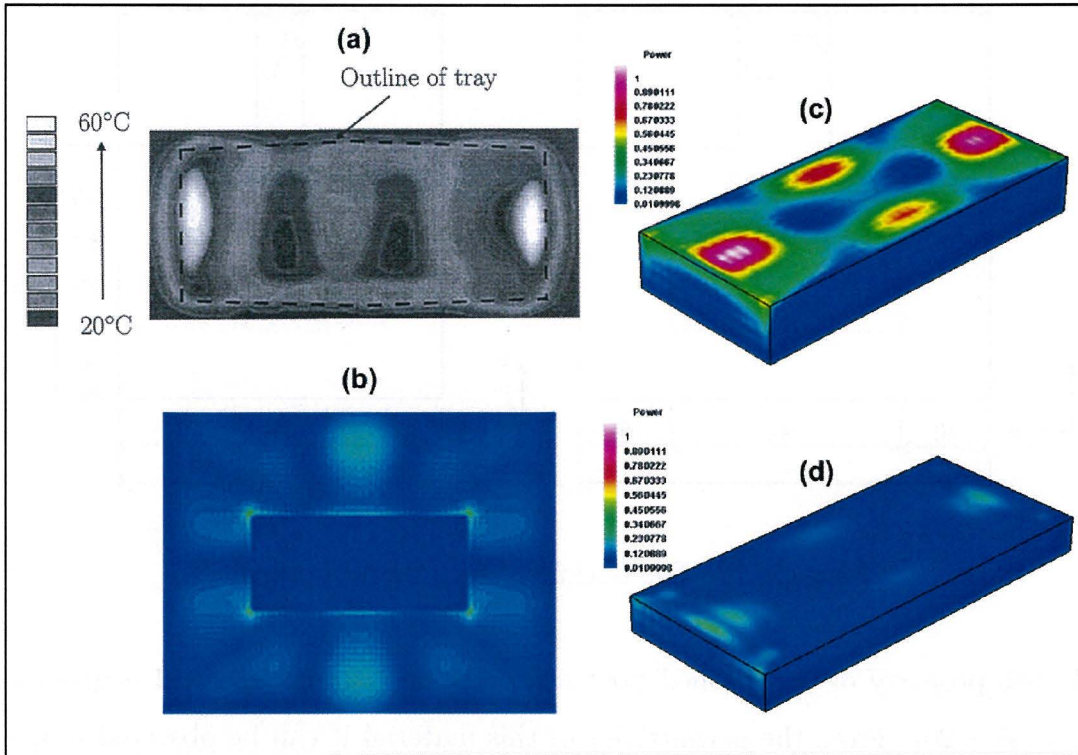


Figure 6.13: Case study 3. Figure shows (a) thermal image of mashed potato, (b) time-averaged electric field distribution inside the cavity, (c) normalised power distribution obtained using the hybrid method at the surface and (d) normalised power distribution through the centre of the block as computed by the hybrid method.

expected to be less concentrated. The power distributions computed here are shown to capture the main aspects of the thermal images, which is thought to be a sufficient validation of the accuracy of the hybrid scheme.

It is evident from Figure 6.13 that the hybrid method can adequately capture the nature of the power distribution when compared to the thermal image. Figure 6.13(b) illustrates the computed time-averaged electric fields at the boundary of free-space and material. It can be seen from the figure that the heating occurs

inside the material according to the time-averaged field computations.

In this case study the free-space component of the apparatus (including the material) was discretised into approximately 1 200 000 cells. The material itself contained around 59 000 cells. In the GMRES solution strategy 157 sub-space vectors were generated for the solution of each electric field component before a residual of less than  $5 \times 10^{-8}$  was obtained. As discussed earlier, Quasi-GMRES was used with 10 reorthogonalisations, which provided a sufficient gain in computational time (about 50%) as opposed to the standard GMRES method. The computations to obtain the approximate solution with the Quasi-GMRES method required approximately 20% more sub-space vector generations than with GMRES.

Approximately 148 minutes were required for the hybrid method to generate the boundary information for the interior problem. Once the boundary information had been obtained, the GMRES solution strategy calculated the power distribution in less than 5 minutes. Altogether, less than 160 minutes of computational time was required to obtain the power distribution. It should be noted that in the case of the hybrid method, only 16 electromagnetic wave periods were calculated in the exterior region using the time-domain solver. In the case of the FD-TD method, 50 electromagnetic wave periods have to be computed before reasonable power distribution estimates are obtained [12]. The FD-TD method also requires a finer mesh (*i.e.* at least 2 000 000 uniform cells), which would require approximately 480 minutes to compute. This time is extrapolated from timings documented in [18].

#### 6.4.4 Case Study 4 - Layers of Pastry

Considering the same cavity as for case study 3 (see §6.4.3) and the same waveguide, the power has been computed using the hybrid method for a pastry block. The pastry block consists of 11 layers of pastry, each  $1\text{ cm}$  thick and layed closely on top of one another. The pastry block has a constant permittivity of  $\epsilon_r = 28 - 8i$ . The dimensions of the pastry block are  $0.11 \times 0.1 \times 0.04\text{ m}^3$ . The block has been pushed to one side and raised  $0.05\text{ m}$  from the bottom of the cavity. The pastry block is touching the  $0.292 \times 0.3\text{ m}^2$  side of the cavity. According to Figure 6.12, the following parameters were used for the simulations,  $a_l = 0\text{ m}$ ,  $a_m = 0.11\text{ m}$ ,  $a_r = 0.281\text{ m}$ ,  $b_l = b_r$ ,  $b_m = 0.1\text{ m}$ ,  $c_l = 0.05\text{ m}$  and  $c_m = 0.04\text{ m}$  are the dimensions associated with this problem.

Figure 6.14 illustrates the pastry block. In the figure, thermal images at two different cross sections are exhibited. The top and centre of the pastry block have been investigated, and the numerical solutions according to the hybrid method are shown next to the thermal images. In Figure 6.14 it is evident that the hybrid method is capable of capturing the power generated in the block produced from the electromagnetic energy. In this work the hybrid method has been computed at a single frequency, which is a reasonable assumption for lossy materials [9].

In this case a mesh consisting of approximately 890 000 cells in the time-domain (including the material) was used to obtain the hybrid method numerical solution. The frequency-domain power distribution was obtained from 12 500 cells inside the load. To obtain reasonable and comparable solutions with the FD-TD method, at least 1 830 000 cells within the domain of the cavity are required [12]. Therefore, there is a large saving in time for the hybrid method.

For this case study involving the pastry block, the Helmholtz equation was

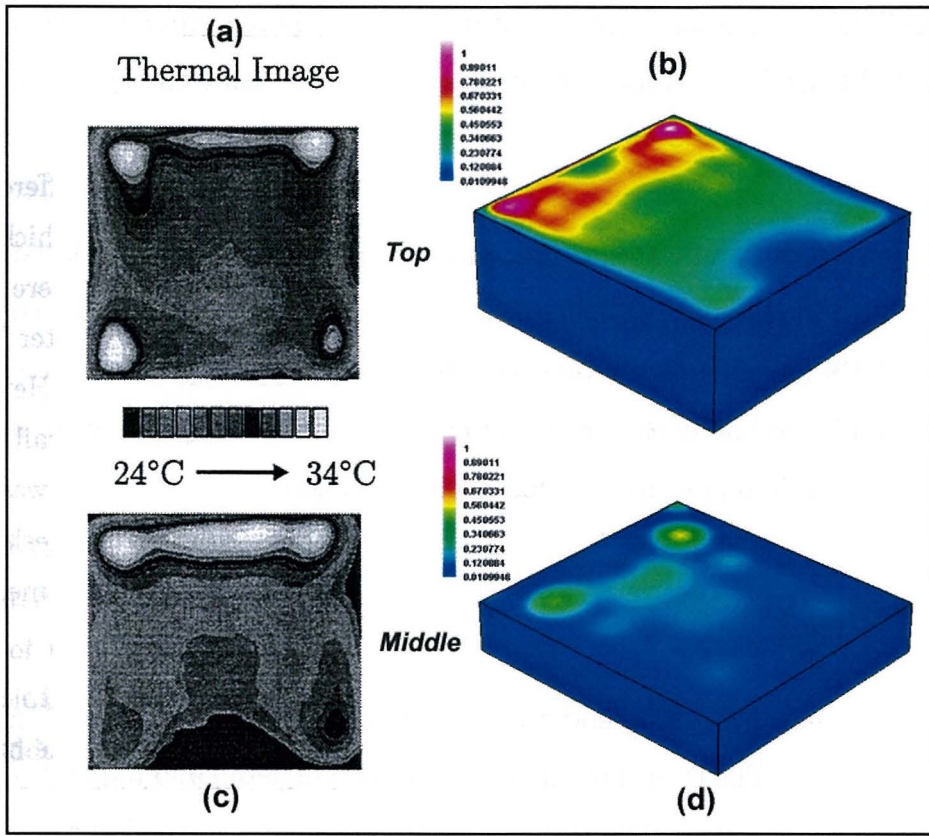


Figure 6.14: Case study 4. Figure shows (a) thermal image of pastry layers at the surface, (b) normalised power distribution obtained using the hybrid method at the surface, (c) thermal image through the centre of the pastry and (d) normalised power distribution through the centre as computed using the hybrid method.

solved implicitly using 12 500 unknown locations, which presented three systems of linear equations of dimension 12 500, for the  $E_x$ ,  $E_y$  and  $E_z$  electric field components. Since the boundary information for the various electric field components for the linear systems was different, the number of subspace re-orthogonalisations varied in the GMRES method before convergence to a desired level of accuracy (*i.e.*  $5 \times 10^{-8}$ ) was achieved. Approximately 110 subspace vectors were needed for each of the components to achieve the desired level of accuracy in the GMRES method. Quasi-GMRES was also investigated and took considerably less time to compute, but required around 130 sub-space vectors. The implementation of

Quasi-GMRES saved a large amount of time, as it required around 220 s to compute the full GMRES, and took about 95 s to compute using the Quasi-GMRES method.

As in case study 3, only 16 electromagnetic wave periods were calculated in the exterior region of the problem before the power distribution was predicted using Quasi-GMRES (10 sub-space reorthogonalisations). Typically, it is necessary to run the FD-TD method in this cavity for around 50 electromagnetic wave periods before a reasonable power distribution is obtained [12].

## 6.5 Conclusions

In this paper a new hybrid method was presented for the microwave heating problem using a cavity. The hybrid method was outlined in detail and implemented on four different case studies. The first two case studies allowed the hybrid method to be benchmarked against the classical FD-TD scheme, whilst the final three case studies showed that the hybrid method produces very good results for real industrial type problems.

The power distribution obtained from the hybrid method was compared to two different thermal images, and was shown to be competitive with existing methods, and can produce results more quickly than the FD-TD scheme. The hybrid method has been formulated using an unstructured mesh terminology, but has been implemented here only on regular structured grids.

Future research will study the use of the hybrid method when an unstructured grid is adapted for the time-domain solver, and the domain of the material is discretised differently to the domain of the free-space. This will require innovative interpolation techniques to capture the boundary information on the material

interfaces. This future research will investigate also the use of structured grids on the free-space region and unstructured grids within the material. Higher order spatial approximations with the cell-centred SLF scheme will also be analysed with the hope of further reducing the number of grid points required to obtain the power distribution, so that even larger problems can be solved more readily.

### Acknowledgements

The authors would like to acknowledge the use of the thermal images from Dr. David Dibben's thesis on finite element methods for the solution of microwave heating problems [22]. The thermal images for case studies 3 and 4 in §6.4.3 and §6.4.4 were adapted in this work to compare the hybrid method to some specific problems. The authors would like to also thank Professor Yousef Saad for his input into fine tuning the GMRES method for this paper. With Professor Saad's help, large computational gains were realised in the solution of the Helmholtz equation.



# Bibliography

- [1] Kenkre, V.M., Skala, L., Weiser, M.W. and Katz, J.D., *Theory of microwave effects on atomic diffusion in sintering: basic considerations of the phenomenon of thermal runaway.* Microwave processing of materials II (ed. W.B. Snyder, W.H. Sutton, M.F. Iskander & D.L. Johnson), Material Research Society Symposium Proceedings, 1991, **189**: p. 179-183, Material Research Society.
- [2] Kriegsmann, G.A., *Cavity effects in microwave heating of ceramics.* SIAM J. Appl. Math, 1997, **57**: p. 382-400.
- [3] Metaxas, A.C. and Meredith, R.J., *Industrial Microwave Heating.* Peter Peregrinus Ltd. London, UK, 1983.
- [4] Kraus, J. D. and Fleisch, D.A., *Electromagnetics with Applications*, McGraw-Hill, 1999.
- [5] Zhao, H. and Turner, I.W., *An analysis of the finite-difference time-domain method for modelling the microwave heating of dielectric materials within a three-dimensional cavity system.* Journal of Microwave Power and Electromagnetic Energy, 1996, **31(4)**: p. 199-214.
- [6] Vegh, V. and Turner, I.W., *A Hybrid Approach for Resolving the Microwave Heating inside Lossy Media.* Advances in Microwave and Radio Frequency Processing, Ampere 8, Germany, 2002.

- [7] Shankar, V. and Mohammadian, A.H., *A Time-Domain, Finite-Volume Treatment for the Maxwell Equations*. Journal of Microwave Power and Electromagnetic Energy, 1990, p. 128-145.
- [8] Madsen, N.K. and Ziolkowski, R.W., *A three-dimensional modified finite volume technique for Maxwell's equations*. Electromagnetics, 1990, **10**: p. 147-161.
- [9] Dibben, D. C. and Metaxas, A.C., *Time Domain Finite Element Analysis of Multimode Microwave Applicators Loaded with Low and High Loss Materials*. Intl. Conf. Microwave and High Energy Heating, 1-3.4, 1995.
- [10] Shang, J.S., *High-Order Compact-Difference Schemes for Time-Dependent Maxwell Equations*. Journal of Computational Physics, 1999, **153**: p. 312-333.
- [11] Yee, K.S., *Numerical Solution of Initial Boundary Value Problem Involving Maxwell's Equations in Isotropic Media*. IEEE Trans. Antennas Propagat., 1966, **14**: p. 302-307.
- [12] Zhao, H., *Computational Models and Numerical Techniques for Solving Maxwell's Equations: A Study of Heating of Lossy Dielectric Materials Inside Arbitrary Shaped Cavities*. Centre in Statistical Science and Industrial Mathematics. Brisbane, Queensland University of Technology, 1997.
- [13] Berenger, J.P., *Three-Dimensional Perfectly Matched Layer for the Absorption of Electromagnetic Waves*. Journal of Computational Physics, 1996, **127**: p. 363-379.
- [14] Petropoulos, P.G., Zhao, L. and Cangellaris, A.C., *A Reflectionless Sponge Layer Absorbing Boundary Condition for the Solution of Maxwell's Equations with High-Order Staggered Finite Difference Schemes*. Journal of Computational Physics, 1998, **139**: p. 184-208.

- [15] Zhao, H. and Turner, I.W., *The use of a Coupled Computational Model for Studying the Microwave Heating of Wood*. Applied Mathematical Modelling, 2000, 24(3), p. 183-197.
- [16] Gedney, S.D. and Lansing, F., *Full Wave Analysis of Printed Microstrip Devices Using a Generalized Yee-Algorithm*. IEEE transactions, 1993, 5, p. 1179-1182.
- [17] Saad, Y., *Iterative Methods for Sparse Linear Systems*. Second Edition with Corrections, <http://www-users.cs.umn.edu/~saad/>, 2000.
- [18] Vegh, V., Turner, I.W., Zhao, H., *Effective Cell-Centred Time-Domain Maxwell's Equations Numerical Solvers for the Purpose of Microwave Heating*. Submitted in the International Journal of Applied Mathematical Modelling, 2002.
- [19] Press, W. H., Teukolsky, S.A., et al., *Numerical Recipes in C: The Art of Scientific Computing*. Cambridge Press, 1997.
- [20] Jayantha, P. A. and Turner, I. W., *A Second Order Finite Volume Technique for Simulating Transport in Anisotropic Media*. The International Journal of Numerical Methods for Heat & Fluid Flow, 2003, 13(1), p. 31-55.
- [21] Saad, Y., M.H.S., *GMRES: a generalized minimum residual algorithm for solving nonsymmetric linear systems*. SIAM Journal of Scientific and Statistical Computing, 1986, 7: p. 856-869.
- [22] Dibben, D.C., *Numerical and Experimental Modelling of Microwave Applicators*. Department of Engineering, University of Cambridge, 1995, 188.



# **Chapter 7**

## **General Discussion**

### **7.1 Conclusions and Remarks**

In this thesis five papers have been presented that comprise the bulk of Chapters 2 to 6. These papers together form the backbone of the theory associated with the newly developed hybrid method. Existing CEM models, although accurate, have been shown to have excessive computational times associated with the simulations of real-world industrial microwave heating problems. The hybrid method was developed as a new more efficient computational method that can overcome these computational bottlenecks. The hybrid method outlined in this thesis has the ability to capture the power distribution within the lossy material accurately and has been formulated specifically for use in an unstructured mesh framework. The method has been analysed and implemented in a number of microwave heating case studies that highlight its numerical prowess.

The paper presented in Chapter 2 considered a waveguide problem with a number of different approaches for resolving the electromagnetic fields inside the waveguide loaded with a ceramic type material. This research work analysed the effect of changes in incident power versus maximum temperature inside the

ceramic block in the context of thermal runaway. It was observed that indeed, for small changes in incident power, it is possible to obtain large changes in the temperature distribution inside the material. The work on the ceramic block provided further insight into the physical phenomenon of thermal runaway and the way in which electromagnetic waves interact with dielectric materials in waveguide and cavity structures.

The simulations resulted in the production of an S-shaped curve for the three different computational techniques: the finite-element frequency-domain method, the finite-difference time-domain method and the semi-analytical method. All techniques investigated produced good results that highlight the significance of temperature jumps from cool to hot branches in the S-curve for certain types of ceramics. This work showed also that it is reasonable to assume a single dominant mode within the waveguide for the frequency-domain solution methodology.

The work conducted in Chapters 3 and 4 was related to finite-volume time-domain numerical solvers for simulating the propagation of electromagnetic waves in free-space and loaded waveguides, respectively. A number of different approaches for resolving the time-domain electromagnetic waves was considered, and each approach was implemented and analysed to identify a numerical solution strategy that is sufficient for capturing the electric and magnetic field components accurately, so that these cell-centred numerical solvers can be used for studying industrial microwave heating processes.

The Maxwell's equations were cast into a surface-volume discrete form so that finite-volume approaches could be used in the numerical simulations. Typically, leapfrog staggered and unstaggered time integration techniques along with third and fourth order Runge-Kutta methods were used in the time marching. Methods emanating from *CFD* (Intensity vector splitting and Riemann solvers) were

investigated in the spatial discretisations with the Runge-Kutta time marching methods, for which the results appeared to be smooth and the noise evident due to locating the electric and magnetic field unknowns at cell centres was removed. It was observed that the staggered, and the third and fourth order Runge-Kutta methods produced results that were comparable to the classical finite-difference time-domain simulations. This work clearly demonstrated that cell-centred finite-volume time-domain solvers can be used to simulate electromagnetic waves for the purpose of microwave heating within a waveguide.

In Chapter 4, a new perfectly matched layer boundary condition was derived for the cell-centred finite-volume methods that used the staggered and Runge-Kutta time marching schemes. It was postulated that this type of absorbing boundary condition can be used with cell-centred schemes, and it was shown that impinging waves into this absorbing layer were absorbed almost entirely. At material and free-space interfaces plane wave assumptions were made to the electromagnetic fields to allow for the calculation of the derivatives of the electric field components. This assumption enabled the development of a numerical technique that performs better at material and free-space interfaces than methods that do not use corrections for the derivatives. At the conducting wall boundaries, spurious cells were formulated in the numerical schemes to allow for fast and efficient calculations of electric and magnetic field component unknowns at the conducting walls of the waveguide. The research work presented in this chapter outlined different cell-centred finite-volume time-domain solvers and also identified and developed new strategies for simulating electromagnetic waves.

The main contribution of this thesis was presented in Chapters 5 and 6, whereby the hybrid method was described in detail. In Chapter 5, the hybrid method was first introduced and the original problem under study was decomposed into localised exterior and interior problems. The exterior problem requires

the solution of the time-domain Maxwell's equations using the cell-centred numerical strategy outlined in Chapters 3 and 4. The interior problem considered the domain of the material alone, and the electric fields inside the medium are calculated using the Helmholtz equation discretisation at some prescribed frequency, or superposition of frequencies. The Helmholtz equation presents electric fields that are in the frequency domain, and as a consequence, the sole purpose of the time-domain solver (*i.e.* the exterior problem) is to generate Dirichlet boundary conditions for the interior problem using the discrete Fourier transform.

In Chapter 5 the Helmholtz equation was solved at the dominant frequency of the waveguide, and the results showed that the simulation results from the hybrid method were very close to that of the finite-difference time-domain scheme. In Chapter 6 a number of different industrial microwave heating case studies were considered within a multi-mode cavity structure. The simulation results generated from the hybrid method were compared to previously published thermal images and it was shown that for various dielectric media, the hybrid method can capture the solution accurately and efficiently.

The work in Chapter 6 showed that the hybrid method can be used with meshes that do not have as many unknowns as, for example, the finite-difference time-domain method. Normally, classical time-marching algorithms require that a large number of electromagnetic wave periods are calculated before the power distribution is determined. In the case of the hybrid method, it was shown that less periods are required for the exterior problem, before the power inside the material can be approximated using the frequency-domain solution strategy for the Helmholtz equation. Advanced numerical linear algebra techniques were investigated to solve the frequency-domain linear system of equations obtained using the discretisation of the Helmholtz equation. Incomplete reorthogonalisation with the generalised minimal residual iterative solver *GMRES* was used to obtain the

best solutions in the hybrid method. Preconditioners were investigated also, but it was observed that for the preconditioners investigated, preconditioning the coefficient matrix in the system of linear equations did not substantially change the time to compute a solution.

The hybrid method is an efficient and accurate computational algorithm for simulating industrial microwave heating processes. The hybrid method has been validated using both exact solutions and also various industrial problems in the microwave frequency range. It was highlighted (especially in Chapter 6) that the hybrid method can generate solutions to problems more rapidly than existing CEM methods, while providing highly accurate solutions to many different industrial microwave heating applications.

## 7.2 Recommendations for Future Work

Computational electromagnetics is a very diverse field and the concepts that are discussed in this thesis have been demonstrated in the context of industrial microwave heating. Nevertheless, most of the ideas from the time-domain numerical solvers work can be applied to other fields, for example radar and satellite communication systems. Although, the hybrid method was strictly developed for microwave oven problems, it will be in the future used also in the radio frequency range for the purpose of studying industrial heating and drying processes.

In particular, it is envisaged that from the work initiated in Chapter 2 of this thesis, further work will concentrate on efficient numerical solutions for other waveguide configurations, such as short-circuited guides and cavities with an iris. The validity of the single mode assumption for waveguide modes, such as the  $TM_{11}$  mode as well as in cavities will also be investigated.

The future work on cell-centred finite-volume time-domain solvers from Chapters 3 and 4 will be twofold, (a) the implementation of higher order spatial approximations for cell face unknown predictions, and (b) the migration of these finite-volume time-domain methods to other meshes, mainly formed from tetrahedra. This work will allow for arbitrary shaped cavities and objects to be simulated, while possibly providing a more efficient numerical strategy.

Other benefits of the hybrid method will see the study of a coupled structured free-space solver (exterior problem) and unstructured material solver (interior problem). This idea should allow for the efficient simulation of arbitrary shaped materials loaded within standard regularly shaped multi-mode cavities. Another area that is of interest within the microwave heating community is the ability to model the microwave heating of non-homogeneous materials. Future work will investigate the dissipated heat obtained from the hybrid method when applied to materials that do not necessarily have uniform dielectric properties.

Future work also will investigate the accuracy of the Helmholtz equation solution strategy for the interior problem under the divergence assumption. A frequency-domain algorithm that ensures that the divergence condition has been met will be rigorously scrutinised in the future.